

Martin Hohberg

**Experimental investigation and
process simulation of the
compression molding process
of Sheet Molding Compound
(SMC) with local reinforcements**

Martin Hohberg

**Experimental investigation and process simulation
of the compression molding process of Sheet Molding
Compound (SMC) with local reinforcements**

**Karlsruher Schriftenreihe Fahrzeugsystemtechnik
Band 80**

Herausgeber

FAST Institut für Fahrzeugsystemtechnik

Prof. Dr. rer. nat. Frank Gauterin

Prof. Dr.-Ing. Marcus Geimer

Prof. Dr.-Ing. Peter Gratzfeld

Prof. Dr.-Ing. Frank Henning

Das Institut für Fahrzeugsystemtechnik besteht aus den Teilinstituten Bahnsystemtechnik, Fahrzeugtechnik, Leichtbautechnologie und Mobile Arbeitsmaschinen.

Eine Übersicht aller bisher in dieser Schriftenreihe erschienenen Bände finden Sie am Ende des Buchs.

Experimental investigation and process simulation of the compression molding process of Sheet Molding Compound (SMC) with local reinforcements

by
Martin Hohberg

Karlsruher Institut für Technologie
Institut für Fahrzeugsystemtechnik

Experimental investigation and process simulation of the
compression molding process of Sheet Molding Compound (SMC)
with local reinforcements

Zur Erlangung des akademischen Grades eines Doktors der
Ingenieurwissenschaften von der KIT-Fakultät für Maschinenbau des
Karlsruher Instituts für Technologie (KIT) genehmigte Dissertation
von Dipl.-Ing. Martin Hohberg

Tag der mündlichen Prüfung: 4. Dezember 2018
Erster Gutachter: Prof. Dr.-Ing. Frank Henning
Zweiter Gutachter: Prof. Dr. Andrew Hrymak

Impressum



Scientific
Publishing

Karlsruher Institut für Technologie (KIT)
KIT Scientific Publishing
Straße am Forum 2
D-76131 Karlsruhe

KIT Scientific Publishing is a registered trademark
of Karlsruhe Institute of Technology.
Reprint using the book cover is not allowed.

www.ksp.kit.edu



*This document – excluding parts marked otherwise, the cover, pictures and graphs –
is licensed under a Creative Commons Attribution-Share Alike 4.0 International License
(CC BY-SA 4.0): <https://creativecommons.org/licenses/by-sa/4.0/deed.en>*



*The cover page is licensed under a Creative Commons
Attribution-No Derivatives 4.0 International License (CC BY-ND 4.0):
<https://creativecommons.org/licenses/by-nd/4.0/deed.en>*

Print on Demand 2022 – Gedruckt auf FSC-zertifiziertem Papier

ISSN 1869-6058
ISBN 978-3-7315-1007-9
DOI 10.5445/KSP/1000104914

Kurzfassung

Die ganzheitliche virtuelle Auslegung von Faserverbundbauteilen aus Sheet Molding Compund (SMC) ermöglicht es durch die Berücksichtigung von Fertigungseffekten in der Struktursimulation, bedarfsgerechtere und somit leichtere und günstigere Bauteile zu fertigen. Hierfür muss jedoch die Prozesssimulation in der Lage sein, die SMC-spezifischen Blockströmung auf Grund der niedrig-viskosen Randschicht richtig zu beschreiben. Nur so kann das richtige Füllverhalten und somit auch die richtige Faserorientierungsverteilung vorhergesagt werden. Dies wird gerade im Kontext des zunehmenden Einsatzes von semi-strukturellen SMC-Formulierungen besonders wichtig. Darüber hinaus gibt es neue Konzepte der Hybridisierung von SMC mit lokalen unidirektionalen Verstärkungen, welche ebenfalls in der Prozesssimulation berücksichtigt werden müssen, um die Positionierung der Verstärkungen abzusichern.

Aus diesem Grund wurde in dieser Arbeit ein neuer dreidimensionaler Ansatz für die Prozesssimulation von SMC entwickelt, der sowohl die durch Dehnviskosität dominierte Kernschicht, als auch die niedrig-viskose Randschicht berücksichtigt. Durch die Verwendung des gekoppelten Euler-Lagrange-Ansatzes, kann auch die Interaktion zwischen SMC und lokalen Verstärkungen abgebildet und vorhergesagt werden. Um die Informationen aus der Prozesssimulation in die Struktursimulation zu übertragen, wurde eine CAE-Kette weiterentwickelt, die das Übertragen der Information vom Prozess- zum Strukturnetz ermöglicht. Hierbei wird sowohl eine Cluster-Bildung, als auch eine Homogenisierung auf Basis der Faserorientierungsverteilung durchgeführt.

Zur experimentellen Analyse des Fließverhaltens, sowie zur Bereitstellung der benötigten validen Materialparameter für die Prozesssimulation, wurde ein neues rheologisches Fließpresswerkzeug entwickelt. Mit diesem Werkzeug wurden erstmal das kompressible Verhalten von semi-strukturellen SMC For-

mulierungen nachgewiesen und über einen phänomenologischen Ansatz beschrieben. Auf Basis dieser Kompressibilitätsformulierung konnte ein neues rheologisches Model entwickelt, das eine genauere Charakterisierung ermöglicht. Durch die Charakterisierung von fünf unterschiedlichen SMC-Materialformulierungen, konnten einige Gesetzmäßigkeiten der Materialparameter abgeleitet werden.

Abstract

A holistic virtual design of Sheet Molding Compound (SMC) components takes manufacturing effects in the structure simulation into account. This enables lighter and cheaper components that meet the needs of the customer due to a reduced margin of safety, compared to today's designs. For that purpose, however, the process simulation must be able to describe the SMC-specific plug flow correctly, which occurs due to the low-viscosity boundary layer. Otherwise, the filling behavior and thus the fiber orientation distribution cannot be predicted correctly. Especially in the context of the increasing use of semi-structural SMC formulations, this is particularly important. In addition, there are new concepts for the hybridization of SMC with local unidirectional reinforcements. These reinforcements must also be considered in the process simulation to ensure the positioning of the reinforcements in the final part.

For this reason, a new three-dimensional approach for the process simulation of SMC is developed in this thesis. This approach takes into account both, the core layer that is dominated by the extensional viscosity and the thin lubrication layer, which is dominated by a high shear rate. By using the Coupled-Eulerian-Lagrangian (CEL) approach, the interaction between SMC and local reinforcements can be modeled and thus, predicted. In order to transfer the information from the process simulation to the structure simulation, a CAE chain is further developed. This CAE chain enables the transfer of the information from the process to the structure mesh. As part of this CAE-chain, a clustering and a homogenization are carried out based on the fiber orientation distribution.

To analyze the flow behavior experimentally and to provide the required valid material parameters for process simulation, a new rheological tool is developed. With this rheological tool, the compressible behavior of semi-structural SMC formulations is proven for the first time and described by using a phenomenological approach. Based on this compressibility formulation, a new

rheological model is developed which allows a more precise characterization. By characterizing five different SMC material formulations, several pattern of material parameters are derived.

Acknowledgments

This dissertation was written during my work as an academic researcher at the Institute of Vehicle Systems Technology, Lightweight Technology at the Karlsruhe Institute of Technology (KIT) between 2013 and 2018.

I wish to express my deepest appreciations to Professor Dr.-Ing. Frank Henning, my thesis advisor. He gave me the opportunity to work in an interdisciplinary environment with a strong cooperation with the Fraunhofer ICT in Pfinztal. This interdisciplinary environment based on the idea of the holistic consideration of fiber reinforced composites and the realization with the Methods–Material–Processes approach was one of the keys of this work. I also appreciate to Professor Dr. Andrew Hrymak, my co-advisor, for all the discussions during my two research stays in London, Ontario at the University of Western Ontario in 2015 and 2017. A special thanks go to Dr. Luise Kärger, who has spent many hours for discussions about current problems which has made a significant contribution to the success of this work. I also want to thank Professor Dr. Tim Osswald for the research stay in 2017 and the discussions with him and his team during this time.

Furthermore, I want to thank all my colleagues from the Institute of Vehicle Systems Technology, Lightweight Technology for the friendly and good working atmosphere. In particular, I would like to thank my colleague Benedikt Fengler, Dominik Dörr, Nils Meyer und Gustavo Blazek. Without their dedicated and professional support and their valuable and constructive discussions, I would not have been able to write this work. I would also like to thank my colleagues at Fraunhofer ICT in Pfinztal for the good cooperation in many joint projects. In particular, I would like to thank Dr.-Ing. Christoph Keckl and Dr.-Ing. David Bücheler for their help with the experimental part of this thesis.

My biggest thanks goes to my parents, especially to my father who showed me what it means to be an engineer until he left us much too early. I also want to thank my wife Jana for all the time, sympathy and motivation during my studies and doctoral work.

I also would like to thank the European Union, the state government of Baden-Wuerttemberg in Germany and the German Research Foundation for its financial support of this work.

Karlsruhe, January 2019

Martin Hohberg

Table of Content

Kurzfassung	i
Abstract.....	iii
Acknowledgments.....	v
1. Preamble	1
1.1. Motivation	1
1.2. Objectives	3
1.3. Structure of the thesis	4
2. State of research.....	7
2.1. Production and molding of SMC.....	7
2.2. Modelling of the SMC flow process.....	11
2.3. Rheological characterization of SMC.....	16
2.4. Modelling of the fiber orientation distribution	22
2.5. Coupled-Eulerian-Lagrangian approach	27
3. Rheological measurements and rheological modelling	33
3.1. Rheological tool and experimental setup	33
3.2. Rheological measurements of different SMC materials	35
3.2.1. Standard Class-A SMC.....	36
3.2.2. Low-Density (LD) Class-A SMC.....	39
3.2.3. Vinylester (VE) SMC.....	41
3.2.4. Unsaturated Polyester Polyurethane Hybrid resin (UPPH) glass fiber SMC	45
3.2.5. UPPH carbon fiber SMC.....	48
3.3. Compressibility of SMC during flow.....	49
3.3.1. Vinylester SMC formulation [Hoh17a]	50
3.3.2. Class-A SMC formulations	53
3.3.3. UPPH SMC formulations.....	54
3.4. Compressible Rheological 2D Shell-Model [Hoh17a]	55

- 3.5. Material Characterization with the Compressible Rheological Model 60
 - 3.5.1. Class-A SMC formulations 60
 - 3.5.2. Vinylester SMC formulation 62
 - 3.5.3. UPPH SMC formulations [Hoh17b]..... 63
- 3.6. Effects of the material type on the rheological behavior and model parameters 69
- 3.7. Alternative flow kinetic of the UPPH glass fiber SMC [Hoh17c] 70
 - 3.7.1. Experimental investigation 70
 - 3.7.2. Model Discussion..... 74
- 3.8. Summary on rheological measurements 77
- 4. Process simulation of hybrid SMC..... 79**
 - 4.1. Application and Evaluation of state of art commercial compression molding software..... 79
 - 4.2. Compression molding simulation by using the CEL approach within Abaqus..... 86
 - 4.2.1. Development of a deformation-rate based material modelling for SMC 87
 - 4.2.2. Implementation of the SMC-Material model 93
 - 4.2.3. Effects of simulation settings on numerical stability and accuracy 101
 - 4.2.4. Consideration of local reinforcements 103
 - 4.3. Validation of hybrid SMC process simulation 104
 - 4.3.1. 2D flow within the rheological tool 104
 - 4.3.2. IRTG reference structure without ribs..... 117
 - 4.4. Summary process simulation..... 126
- 5. Process simulation within a CAE chain for long-fiber reinforced composites 127**
 - 5.1. Export of results..... 129
 - 5.2. Mapping of process simulation results..... 131
 - 5.3. Linear elastic homogenization with anisotropic material cards ... 135

5.4. Effects of the consideration of fiber orientation in the structural simulation	140
5.5. Summary CAE Chain for long-fiber reinforced composites	144
6. Conclusion	145
Nomenclature	153
Greek Symbols	153
Latin Symbols	154
Abbreviation	158
Table of Figures	161
List of Tables	169
References	171

1. Preamble

1.1. Motivation

In the automotive and in the commercial vehicle industry, long fiber reinforced composites are challenging in terms of two main tasks: weight and cost reduction of complex shaped structures. In this context Sheet Molding Compound (SMC) has an outstanding price to stiffness ratio and a good stiffness to weight ratio [Sch07], [Nic11], [AVK13] for medium to high volume productions [Åke00], [Sch07]. Due to its possible Class-A surface and its high freedom of design, SMC is widely used for exterior parts. By combining SMC with local unidirectional reinforcements, the resulting hybrid structure can carry high loads in the known load direction, while it can integrate functions and increase the bending stiffness by adding ribs.

To design such a complex hybrid structure, a combination of different simulation steps is necessary. In such a CAE-Chain, the design, the process and the structural simulation are combined to consider previous results in further simulation steps [Kär15], [Hoh16b]. Since many structural results are strongly dependent on the fiber orientation distribution, the process simulation with its fiber orientation prediction is an important step in such a CAE-Chain.

Comparing the results from commercial process simulation tools with experimental results of compression molding processes, differences in accuracy can be noticed, which depend on the polymer type. For thermoplastic materials, material models for the injection molding process have been developed over a long time. In addition, compression molding simulation of reinforced thermoplastics also shows good agreement with experiments and the flow fronts can be predicted even for complex rib structures as shown by Hohberg and Baumgärtner [Hoh16a]. As the thermoset market is much

smaller than thermoplastic injection molding, the prediction of the flow induced pressure shows significant differences with experimental data due to the lack of validated material models [Hoh15]. Therefore, material models, which can describe the characteristic SMC plug-flow, are crucial. This plug-flow occurs due to the resin-rich lubrication layer with a low viscosity at the mold surface. Due to this lubrication layer, no velocity gradient and therefore, no stress gradient occurs within the plug flow region. Such plug-flow models were developed for 2.5D approaches by Osswald [Oss87], but not for the nowadays regular 3-D simulation models. Therefore, no rib structures or T-shaped parts can be simulated satisfactorily. Furthermore, the consideration of local reinforcements in the molding process needs to be implemented in such a new approach, as there is a strong interaction in in-plane as well as in the out-of-plane directions. Since these reinforcements can move within the tool, the basic assumption for a 2-D or 2.5D approach is not valid any more, as velocity gradients through the thickness can occur.

Material flow properties are important for the correct prediction of material flow and the fiber orientation. Since the fiber length of 1 inch (25 mm) is in the same range as the typical sample size of shear- or rotational rheometers, new experimental rheological measurement approaches are necessary for SMC. To consider the material specific flow behavior during the rheological characterization, a novel in-line rheometer was presented by Dumont et al. [Dum03]. Due to the setup, two separate molding trials had to be performed, which caused inaccuracies due to material variations and slightly changed boundary conditions like thermal conditions and closing speed and material placement. Furthermore, such a setup cannot deal with the compressibility of the SMC during the molding trials. To avoid these inaccuracies, an enhanced rheological measurement tool is needed.

1.2. Objectives

The target of this thesis is to investigate and to model the compression molding process of Sheet Molding Compound (SMC) with local reinforcements. To reach this target, an improvement of the compression molding process and especially the rheological material behavior is necessary. Since new SMC material formulations were developed during the last years [Hen17], different formulations need to be investigated. Therefore, a new method to characterize the rheological properties has to be developed. This method needs to be close to the industrial process to ensure the validity for the further use of the rheological parameter. Therefore, industrial standards like the process settings need to be considered.

Based on the experimental investigation and characterization, a new SMC specific simulation approach will be developed. This approach has to consider the two dominating effects of the resin-rich lubrication layer with its high shear gradient and the core region with its plug-flow behavior. Since SMC is a non-Newtonian fluid, modeling of the shear and extensional viscosity are two of the most important steps towards better process simulation.

To show the capability of this new process simulation approach, a validation with a reference structure is performed. Local unidirectional reinforcements are also considered in a first approximate model. The results are compared with the actual produced part. Furthermore, the fiber orientation results are needed in the structural simulation. Therefore, a CAE-chain is developed, which can process the result information. This simulation processing output contains the export, the mapping and the homogenization, so that structural simulation can be performed.

Briefly summarized, the following sub-objectives can be defined:

- Experimental investigation of the rheological behavior of different SMC formulations
- Development of a method to measure the rheological properties of SMC

- Development, implementation and application of advanced compression molding simulation models for SMC with simple local reinforcements
- Determination of material parameters of different materials for the implemented models
- Validation of the implemented models on a reference structure
- Development of a long fiber CAE-chain to transfer result information from the process to the structural simulation

1.3. Structure of the thesis

This thesis is divided into four chapters, starting with the presentation of the state of research in the area of process characterization and simulation of SMC. Therefore, the SMC production and molding process is described in Section 2.1, followed by the modelling approaches in Section 1.2. In Section 2.3, the different types of rheological characterization methods for the SMC are presented. For the holistic simulation description, fiber orientation development during the molding process and the corresponding closure approximations are introduced in section 2.4. In the last section of the first chapter, the Coupled-Eulerian-Lagrangian approach is introduced, which enables a fluid-structure-interaction in a closed simulation. This is essential for the SMC-tool interaction as well as for the SMC-reinforcement interaction.

The second chapter focuses on the development of a new rheological tool, of a new rheological model and on the characterization and evaluation of different SMC material formulations. In Section 2.1, the new rheological tool and the experimental setup are presented. In section 3.2, five different SMC materials are presented and their experimental characterization tests are performed. The chosen materials range from the typical Class-A SMC, through state of research low-density formulations to three novel semi-structural SMC formulations. Based on the experiments, the material compressibility is proven for the semi-structural SMCs in section 3.3 and considered for the first time in a compressible rheological model in section 3.4. By using this new

compressible model, the rheological properties are evaluated in section 3.5. By evaluating these properties, physical laws and corresponding modelling recommendations could be deduced, which is given in section 3.6. Due to the different behavior of the carbon fiber semi-structural formulation, an alternative flow kinetic is presented for such a material in section 3.7.

In the third chapter, the process simulation of hybrid SMC is presented. As basis for development, the state of art software is tested in section 4.1. In the section 3.2, the new SMC specific 3D simulation approach is developed and implemented in the Coupled-Eulerian-Lagrangian method. This is done by dividing the flow into the extensional viscosity dominated core region and the shear rate dominated lubrication layer at the tool surface. In section 4.3, this model is validated by means of characterization experiments and by a hybrid demonstrator, consisting of SMC and local unidirectional reinforcements.

In the context of the holistic virtual part design, the fourth chapter addresses the CAE chain. The export of the process simulation results (e.g. fiber orientation distribution) is presented in section 5.1. In section 5.2, the mapping and in section 5.3, the linear elastic homogenization within the CAE chain is described. At the end of this chapter, an example is given in Section 5.4, showing the effects of the consideration of process results in structural simulation.

2. State of research

At the beginning of this chapter, the production of the semi-finished Sheet Molding Compound (SMC) and the compression molding process is introduced. This introduction is followed by the state of research for the process simulation (Section 2.2) and the rheological characterization methods (Section 2.3) of SMC. For the simulation methods, the state of the art fiber orientation models (Section 2.4) and approaches for the simulation of material flow by using Finite-Element-Methods for large deformations, respectively material flow (Section 2.5), are described.

2.1. Production and molding of SMC

Sheet Molding Compound (SMC) denotes both, a compression molding process of a stack of planar semi-finished discontinuous fibers and the thermoset-based material itself. The main application for SMC is the exterior of automobile and commercial vehicles. Therefore, the semi-finished material is mainly based on an unsaturated polyester (UP) resin, which is mixed with mineral fillers and other process simplifying and material improving ingredients (see Figure 2-1) depending on the designated application [Che16]. Besides the UP resin, alternative resins like Vinylester resin with higher mechanical properties, phenol formaldehyde resins and epoxy resins are used [Org12], [Hen17]. For a Class-A SMC, the fillers have the highest content in the paste. The main task of the fillers is to increase the viscosity and therefore to avoid fiber-matrix separation and to reduce the price of the material. Depending on the filler type, it can also functionalize the SMC. For example, Aluminum hydroxide ($\text{Al}(\text{OH})_3$) has flame retardant properties, which can lead to aviation certified SMCs [AVK13]. To achieve the high Class-A surface quality, dispersed thermoplastic additives are added. Due to these additives, the macroscopic process-induced shrinkage is distributed to many homogeneously

distributed micro-areas within the material. Within these micro-areas, the thermoplastic additives volume is increasing due to the higher temperature, while the curing resin is shrinking. This leads to components which are almost completely free of distortion or residual stresses [Kec16]. An important ingredient is also the thickening agent. It is used to increase the viscosity of the paste to handle the semi-finished products and to prevent fiber matrix separation during the molding process [Kec16].

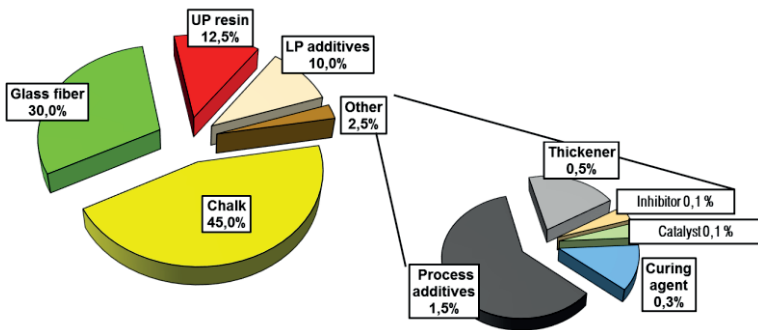


Figure 2-1: Composition of a typical Class-A SMC in wt.-% [Hoh15]

All liquid ingredients together with the fillers are mixed and filled in the so-called doctor box or knife-coating box (see Figure 2-2) of an SMC conveyor belt system. Two boxes are present on an SMC production line to cover and coat the upper and lower carrier foils, which are continually moved, with a thin resin film. In the next step the continuous fibers, which are fed into the chopping units, are cut to the designated fiber length of commonly 1 inch (approx. 25 mm). These chopped fibers fall onto the lower foil, covered with the resin filler paste, with a random in-plane orientation. By changing the speed of the foils, the fiber content can be adjusted. After covering the fibers with the upper impregnated foil, the whole material is impregnated in a calendaring zone. In this area, the air is moved out to prevent air entrapments

in the final part. In the end of the manufacturing process, the already thickened material is coiled up or cut into flat sheets [Org12], [AVK13], [Che16].

For further detailed information regarding the SMC ingredients and a detailed description of the manufacturing process of the semi-finished SMC, please see the chapter “Sheet Molding Compound” from Nicolais and Barzachiello [Nic12].

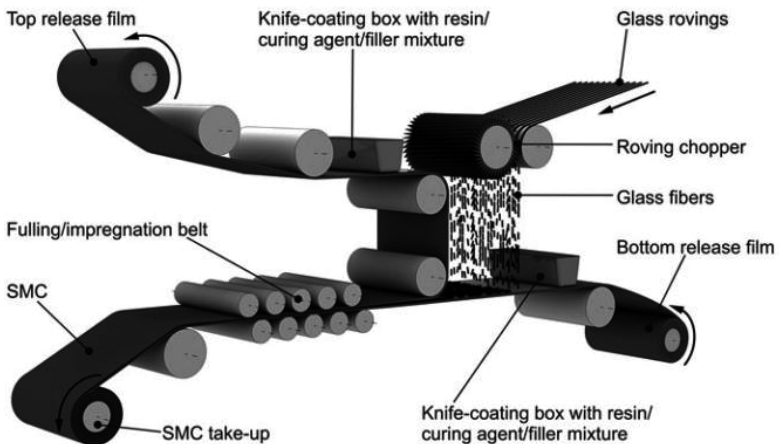


Figure 2-2: Principle of SMC production [Che16]

After a maturing time between two and four weeks, in which the viscosity of the semi-finished product is increasing, the material is ready to be processed in the compression molding process. Due to the ongoing increase of viscosity, the material is usable between a few weeks up to several month depending on the storage conditions, the resin type and the amount of thickening agent [Che16], [Org12].

For the molding process, the coiled SMC semi-finished material is cut and the single sheets are stacked into an initial charge (IC). The number of sheet layers

as well as the shape and size of the initial charge depend on the mold size and shape (see Figure 2-3). Typically, the initial charge covers between 40 and 70% of the projected mold surface, which is also the ratio of the initial filled to the total surface area. This reduces the press pressure on the one side, but on the other side, also to generate some material flow to release entrapped air and process induced styrene bubbles. The molding tool is tempered between 140 and 160°C depending on the resin system, while the initial charge is placed at ambient temperature conditions into the mold. After placing the initial charge into the mold, the mold is closing with a closing speed between 1 and 10 mm s⁻¹. During the compression molding process, the pressure is increasing up to 200 bar for glass fiber SMC and up to 300 bar for carbon fiber SMC. These limits are ensured by limiting the maximum press pressure. If this limit is reached, the closing speed is reduced and therefore the pressure within the mold. After the mold is filled, the material stays in the mold under a high pressure until most of the curing process is finished. The curing time within the mold is between 30 seconds and 3 minutes depending on the resin system, the mold temperature and the part thickness. After the curing phase, the final part can be ejected [AVK13], [Che16], [Org12].

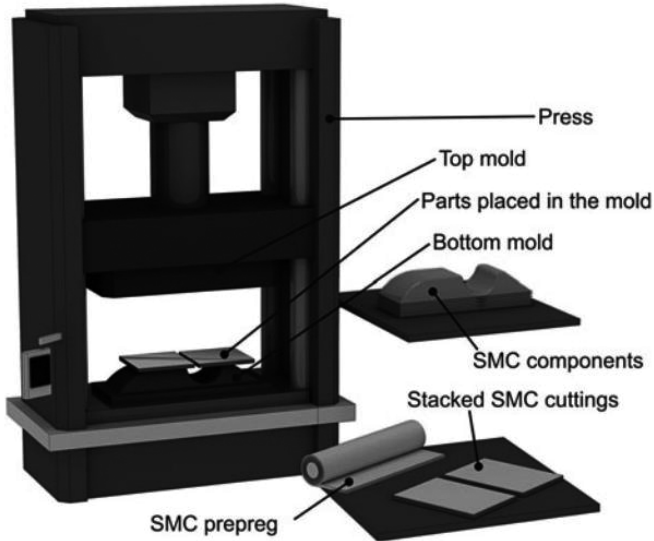


Figure 2-3: Process steps for the manufacture of SMC components with cutting, stacking, placing of the initial charge in the mold and the final part [Che16]

For further detailed information please see the chapter “Sheet Molding Compound” from Nicolais and Barzachiello [Nic12].

2.2. Modelling of the SMC flow process

For all modelling approaches of the SMC flow process, it can be assumed that no curing reaction occurs during the compression molding as long as the SMC material is flowing. This assumption is supported by many experimental results from Marker and Ford [Mar77], as well as Barone and Caulk [Bar79]. Also newer fast curing SMC formulations fulfill this assumptions like Bücheler [Büc17] showed in his PhD thesis. Therefore, it is sufficient to describe the flow phase by using (thermo-) mechanical models. These models can generally be divided into two types with regard to their level of detail. On the one

side, there are specialized models, which simulate the fibers and the paste separately, so that fiber matrix separation effects (changing of local fiber volume content) can be described. These fiber matrix separation effects were observed in T-shaped molds [Kim92], [Kim97], [Kuh18] and especially at ribs [Xu93], [Chr97]. To model these effects, the fibers are resolved individually to simulate the fiber-fiber and the fiber-fluid interactions [Pér15], [Kuh18]. Due to the complexity of these models, only small spatial problems can be simulated with such an approach. Another, less computationally intensive, approach is a two-phase model based on the mixture theory on a macroscopic scale. This approach describes the two phases, fiber and paste (resin and filler), by a volume fraction partitioning. To model the flow of both phases, additional balance and constitutive equations are required. Therefore, a modified Darcy's law was used by Orgéas et al. [Org06], [Org07] and Dumont et al. [Dum12]. Up to now, these models are just empirical modifications of Darcy's Law, where numerous non-physical model parameters need to be fitted to experimental results with high computational effort.

On the other side, macroscopic one-phase models are used more widely. The SMC material is described as a continuum fluid so that the matrix and the fibers have the same velocity and therefore no fiber-matrix separation will occur. The fiber orientation is then computed from fiber orientation models based on physical and empirical models and the flow field (cf. section 2.4). The first one-phase models were taking advantage of the shell-like structure of the most SMC parts. Hence, the thickness is relatively small compared to the other in-plane dimensions. Therefore, generalized Hele-Shaw shell models were developed [Sil80], [Hie80], [Lee84], [Jac86], [Oss90], [Adv90b], [Twu93]. The generalized Hele-Shaw shell model describes a 2D flow in a domain with a small thickness compared with the in-plane dimensions. These models employ a Newtonian description of the SMC material and the no-slip condition between the SMC and the mold surfaces. This leads to a high shearing of the fluid across the thickness of the mold cavity.

Barone and Caulk [Bar85] showed with their experiments the need for better and suitable material models. By using different colored SMC sheets and performing experiments over a wide range of closing speeds, they showed a plug-flow behavior of the SMC core region and the presence of a resin rich lubrication layer (see Figure 2-4). Furthermore Lee and Tucker [Lee87] showed the dependency of the lubrication layer thickness on the compression molding process settings.

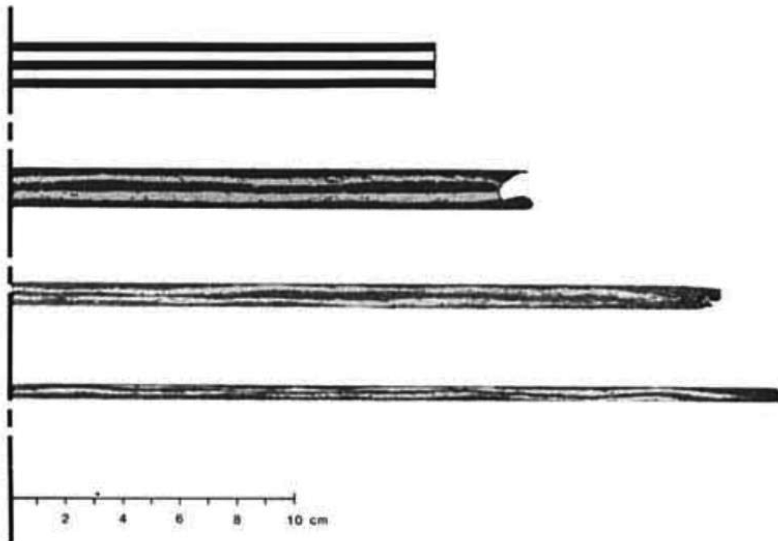


Figure 2-4: Experimental investigation of the flow behavior of SMC by using differently colored SMC sheets [Bar85]

Based on these experiments considering the lubrication layer, analogue material models were developed. In a first step, different friction formulations were investigated to consider the lubrication layer in a generalized Hele-Shaw shell model by Barone and Caulk [Bar86]. By comparing the friction mechanisms of constant friction, hydrodynamic friction and Coulomb friction in the

simulations with the experiments, the hydrodynamic friction approach based on the relative velocity at the mold surface gave the best consistency. Based on this result and on the consideration of uniform in-plane shear and extensional deformation [Kot98], [Dum03] as well as only out-of-plane shear in the lubrication layer [Ode04], various new material flow models were developed and improved [Bar87], [Bar88], [Cas89], [Oss94], [Abr03], [Dum03], [Dum07], [Gui10], [Gui12]. These models use the superposition of the fluid pressure p , the viscous stress of the core region σ_{rheo} and the friction stress from the lubrication layer σ_{fric} , by assuming an incompressibility of the material:

$$\boldsymbol{\sigma} = -p\mathbf{I} + \boldsymbol{\sigma}_{\text{rheo}} + \boldsymbol{\sigma}_{\text{fric}}, \quad (1)$$

where the incompressibility for a control volume is defined as:

$$\frac{\partial v_x}{\partial x} + \frac{\partial v_y}{\partial y} + \frac{\partial v_z}{\partial z} = 0 \quad \text{and} \quad (2)$$

$$\frac{d}{dt} \rho(t, \mathbf{x}(t)) = 0, \quad (3)$$

where \mathbf{v}_i is the velocity in x , y or z , and ρ the density of the material.

As a result of these one-phase models, which take into account the core layer and the lubrication layer behavior, it can be stated that certain modelling approaches have proven their effective value. As the lubrication layer is relatively thin compared to the part thickness, the hydrodynamic friction approach by using a power-law model becomes the state of the art in research studies [Abr03], [Dum07], [Org12], [Gui12]:

$$\boldsymbol{\sigma}_{\text{fric}} = -\lambda \left(\frac{\|\vec{v}\|}{v_0} \right)^{m-1} \frac{\vec{v}}{\|\vec{v}\|} \otimes \vec{n}. \quad (4)$$

In this equation, \vec{v} represents the velocity in the surface plane, λ is the hydrodynamic friction coefficient, m is the power-law coefficient and \vec{n} the normal surface vector. Furthermore, \otimes represents the dyadic product of both vec-

tors. In this equation, the velocity \vec{v} and the surface normal vector \vec{n} are perpendicular to each other. Therefore, the symmetry of the friction stress tensor σ_{fric} is sacrificed.

For the viscous stress of the core region, a deformation rate dependent power-law approach becomes the state of art in research [Le 02], [Dum03], [Dum07], [Org12], [Gui12]:

$$\sigma_{rheo} = \eta \left(\frac{\|D\|}{D_0} \right)^{n-1} D. \quad (5)$$

In this equation, η represents the extensional viscosity for a pure strain load case, D the deformation rate tensor, which is deviatoric, and n the viscous stress power-law coefficient.

Motivated and based on the experiments by Barone and Caulk [Bar85] a multilayer plug flow model, considering the single SMC sheets, was developed by Letierrier and G'Sell [Let96]. This model is also based on a generalized Hele-Shaw approach, but calculates the deformation of every single sheet and their interactions. As the result is similar to the previous Hele-Shaw shell models but more comprehensive, this approach was not continued.

None of the presented one-phase approaches considers the anisotropic flow properties of the SMC material due to its fiber orientation. Depending on the process condition (e.g. initial charge, closing speed), anisotropic material properties can be observed in the final part structure and also a change in the flow was assumed by Kim et al. [Kim92]. Therefore, a Hill's anisotropic yield criterion in conjunction with a rigid visco-plastic formulation was chosen and a resulting finite element formulation was developed [Kim92], [Lin97], [Lin99]. These models were able to describe the slight changes due to the anisotropy, at the expense of six additional parameters, which must be determined as a function of the strain rate. Due to the complex modelling and characterization, this approach was not continued.

Since all these approaches are based on a 2.5D model, a limitation in the prediction of complex shaped parts can be identified. For example in ribbed parts, the Hele-Shaw boundary condition of a relative low height compared with the in-plane 2D dimension is not satisfied anymore. Therefore, a new 3D approach is developed in this thesis to overcome the Hele-Shaw limitations. By developing such a 3D approach, new functionalities like the interaction with local reinforcements or inserts are possible. Therefore, the state of the art research approaches from the 2.5D simulations are used and extended to the 3D simulation.

2.3. Rheological characterization of SMC

The aim of the rheological characterization of SMC is to determine the necessary material parameters for the flow models during the compression molding process. This can be done by two different methods. On the one side, shear or rotational rheometers can be used. This is an established method to characterize the rheological properties of polymers, but has the disadvantage that the induced flow in a rheometer is different to the flow in a mold. In a rheometer, high shear rates are applied, while SMC shows a bulk flow behavior due to the lubrication layer in the compression molding process (cf. Section 2.2). Furthermore, typical process parameters such as the applied pressure cannot be realized in a reasonable way. Besides this, the typical sample diameter size for a shear or rotational rheometer is as long as the fiber lengths of the SMC (1 inch, 25 mm) [Lee81].

In contrast to traditional laboratory scale rheology, in-line rheological compression molding tools and corresponding characterization models were developed. These in-line rheological tools use different flow kinetics and therefore, different input types. On the one side, in-situ methods are used which utilize in-mold pressure sensors, press force or transparent mold sides to follow and record the flow fronts. These in-situ flow kinetics include squeeze

flow, simple compression, channel flow and simple shear. In addition, a characterization based on the flow length depending on the process parameters was performed using spiral flow.

The squeeze flow method [Sil81], [Lee81], [Kot98] is very simple (see Figure 2-5) and one can observe the material over a large range of strain rates by varying the closing speed for radial flow of the sample. By recording the press force and the sample thickness by the distance between the mold sides, a generalized Hele-Shaw model (cf. section 2.2) can be used to determine the material parameters. For these tests, it is crucial that no slip between the SMC material and the mold surface occurs, as this would lead to an extra shear stress, which would affect the measurements. Due to the setup, the flow kinematic is neither homogeneous over the sample thickness nor along the flow radius. Therefore, the inversion of the flow models from section 2.2 needs to be done iteratively to consider the correct flow kinematics while fitting the material parameters. This can easily lead to errors in the material parameters. Therefore, these types of rheological testing is mainly done for simple rheological models which assume incompressibility of the material [Org12].

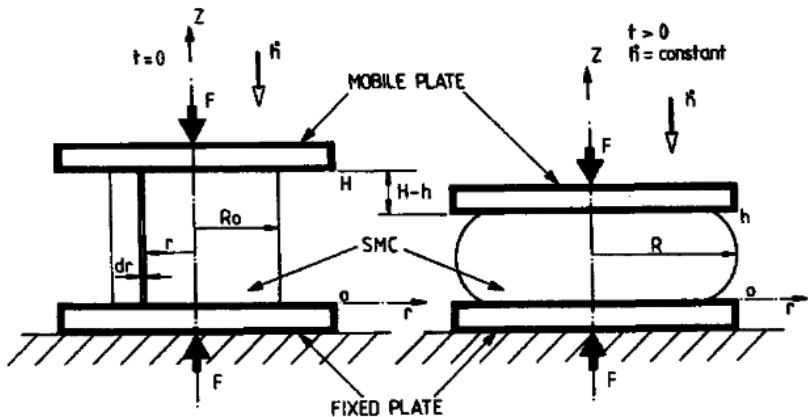


Figure 2-5: Schematic illustration of the squeeze flow rheometer [Sil81]

The simple compression in-line rheometer [Mic90], [Le 02], [Dum03], [Dum07], [Mar09], [Gui12] is based on the same idea as the squeeze flow rheometer, but overcomes its disadvantage by lubricating the mold surfaces and using a higher initial radius to height ratio (see Figure 2-6). Due to the slip condition, as a result of the lubricated mold surface, the material flow is more homogeneous. As the experiments were performed with constant strain rates, the extensional viscosity can be calculated directly by using eq. (5). As the lubrication layer is suppressed in these experiments, the friction parameter cannot be determined. Furthermore, the material flow in the rheometer is different to the flow in the real tool, as the friction stress is missing.

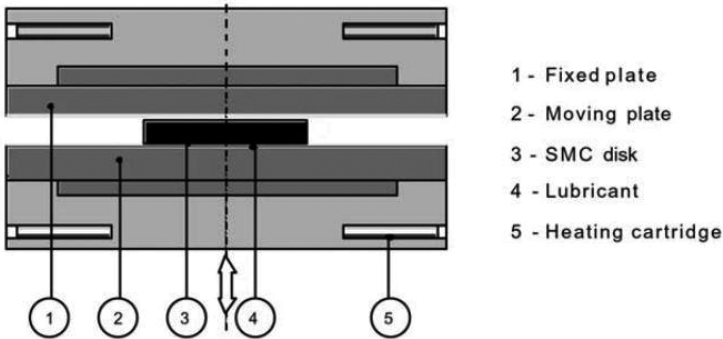


Figure 2-6: Schematic illustration of the simple compression rheometer. To gain simple compression, the mold surfaces are lubricated [Dum03]

The plane strain/channel flow rheometer [Cas90], [Lin97], [Lin99], [Dum03] simplifies the flow compared to the simple compression rheometer. Instead of molding the sample in a 2D flow, the material flow is reduced to a quasi 1D (see Figure 2-7). These tests were performed with and without lubricating the mold surfaces. Due to the simplification of the flow and the high ratio of the initial charge length to the initial charge height, no flow kinetic gradient occurs within the material. Therefore, a generalized Hele-Shaw shell model with

a deformation rate based core region and the lubrication layer can be developed by using the eq. (1) – (5). By inverting this model, the material parameters for both regions can be determined.

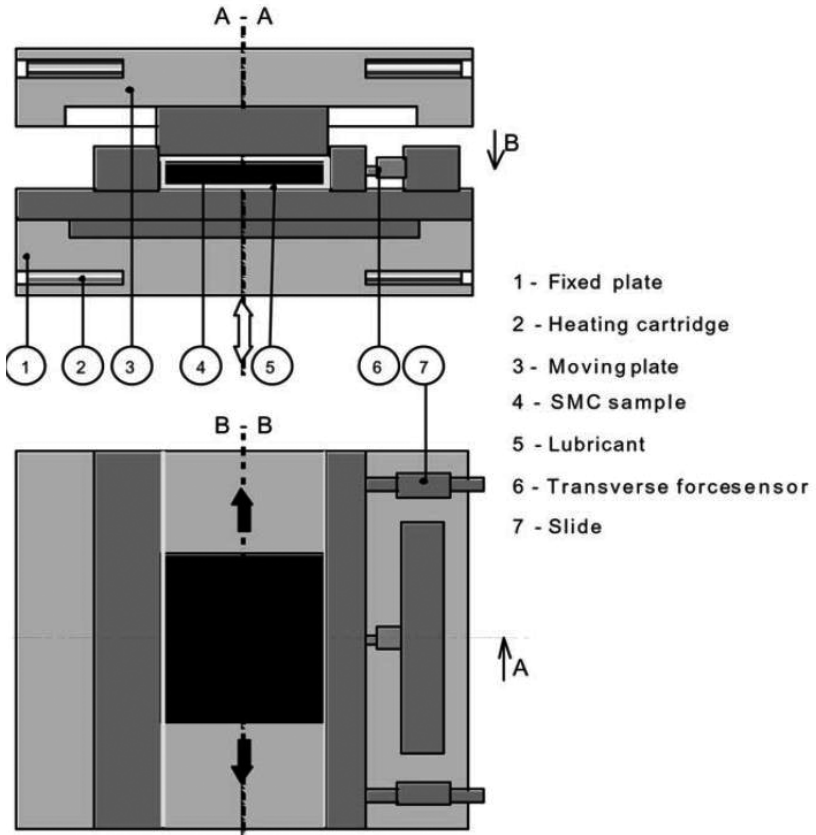


Figure 2-7: Schematic illustration of the plane strain/channel flow rheometer. To gain plane strain, a 1D flow is enforced [Dum03]

The in-line rheometer based on the simple shear kinetics [Le 02] is an up-scaled rotational rheometer. Due to the larger scale, a sufficient ratio between fiber and sample diameter as well as sample diameter to height is ensured. To get closer to the industrial molding conditions, normal forces are applied. This also helps to prevent the slip between the material and the mold surface. In some cases, this is not sufficient to prevent slip and an additional adhesive film can be introduced between the mold surface and the sample. Due to the no-slip condition of the material at the mold surface, these experiments could only be performed at room temperature to prevent the development of the lubrication layer, as higher temperatures would lead to a slip. Due to the plug flow behavior of the core region of the SMC, the shear behavior is mainly important for the hot resin-rich lubrication layer. Due to these problems, simple shear rheometers have not been further investigated.

The spiral flow [Rab08] is mainly used to compare materials under the same process conditions. Therefore, the materials are placed in the center of the tools (see Figure 2-8) and the flow length along the spiral is compared. By changing the process conditions, the best material for specific molding processes can be identified quantitatively. Besides this method, the flow along the spiral can be approximated as a 1D flow. Therefore, the tool can be used as a plane strain rheometer. By using the pressure sensors and the press pressure, the hydrodynamic friction coefficient can be calculated. By comparing the results between this spiral flow rheometer and the plane strain rheometer, a good match could only be achieved for low fiber volume contents and medium filler contents. These differences might come from the approximation of the plane strain, which is not completely satisfied in this case. Therefore, this type of rheometer has not been investigated for the characterization of SMC materials regarding the process simulation.

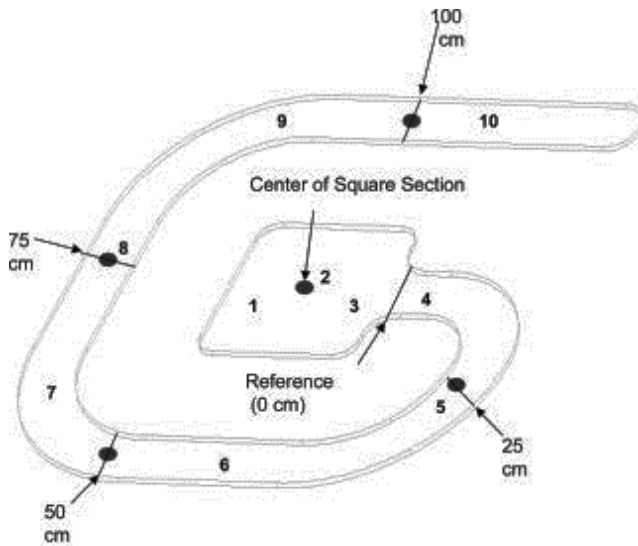


Figure 2-8: Schematic illustration of a spiral flow tool [Rab08]

The plane strain rheometer becomes state of the art in research for the rheological characterization of SMC. They are close to the industrial process and therefore, the characterization results can be used for industrial applications. The available plane strain rheometers have the huge disadvantage that at least two measurements with different initial charge positions are needed. By comparing the different pressure distributions of these different initial charge positions, the characterization is performed. Due to the reproducibility of flows and the local variation of the SMC material properties, this leads easily to small inaccuracies due to experimental errors. To overcome this disadvantage, a new plane strain rheometer is developed in this thesis, with which a characterization within a molding trial could be performed. Due to the new design, the flow front can be traced during the molding process at several points. This enables additional characterizations of the material flow and therefore, a more precise understanding of the SMC compression molding process.

2.4. Modelling of the fiber orientation distribution

As explained in section 2.2, the main macroscopic models describe the SMC as a one-phase fluid. Therefore, the fibers and their orientation are modeled as a function of the flow. Such a homogenization of particles were firstly introduced by Einstein [Ein1906]. Based on this idea, Jeffery [Jef22] developed the first fiber orientation model for the rotation of a single ellipsoid fiber. By assuming a Newtonian fluid, a linear velocity field far away from the fiber and no buoyancy or inertia effects, an exact and closed solution has been developed. The model describes the two main fiber orientation phenomena: the fiber alignment in the shear direction and the alignment in the stretching direction. The initial orientation of a single fiber at the beginning of a calculation step is described by the unity vector \mathbf{p} and based on the following expression of reorientation:

$$\frac{d\mathbf{p}}{dt} = \mathbf{W} \cdot \mathbf{p} + \xi (\mathbf{D} \cdot \mathbf{p} - [\mathbf{p} \cdot \mathbf{D} \cdot \mathbf{p}] \mathbf{p}), \quad (6)$$

where \mathbf{W} represents the vorticity tensor (see eq. 50), \mathbf{D} the rate of deformation tensor and ξ the particle shape defined as:

$$\xi = \frac{ar^2 - 1}{ar^2 + 1}, \quad (7)$$

where the aspect ratio of the fiber is $ar = l/d$ ($\xi = -1$: disc, $\xi = 0$: sphere, $\xi = 1$: ellipsoid with $l \gg d$).

In the next step, a model to predict the fiber reorientation in concentrated suspensions was developed by Folgar and Tucker [Fol84]. Based on their experiments, they added an empirical rotary diffusion term to the Jeffery's equation (eq. (6)) to model the fiber-fiber interactions. As not all fibers are aligned in the same direction, an efficient way to store this information is necessary. By introducing the fiber orientation function $\Psi(\mathbf{p})$, which is fitting the angular distribution over the in-plan orientation, a new storage method was developed:

$$\int_S \Psi(\mathbf{p}) \, d\mathbf{p} = 1, \quad (8)$$

where $\int_S d\mathbf{p}$ denotes the integral over the area of all possible directions of the fiber orientation vectors \mathbf{p} . To represent a 3D fiber orientation, the fiber orientation tensor \mathbf{A} was introduced [Ken84], [Adv87]. The fiber orientation tensor is a symmetric second order tensor:

$$\mathbf{A} = \int_S \mathbf{p} \otimes \mathbf{p} \Psi(\mathbf{p}) \, d\mathbf{p}, \quad (9)$$

or fourth order tensor:

$$\mathbb{A} = \int_S \mathbf{p} \otimes \mathbf{p} \otimes \mathbf{p} \otimes \mathbf{p} \Psi(\mathbf{p}) \, d\mathbf{p}, \quad (10)$$

with the trace of one, due to the statistical distribution function. An example of the fiber orientation distribution and the corresponding in-plane second order fiber orientation tensor is given in Figure 2-9. The model developed by Folgar and Tucker gave good agreement with short fiber suspensions, but it raised the problem with the need of the fourth order tensor (\mathbb{A}) to calculate the second order fiber orientation tensor change ($\frac{d\mathbf{p}}{dt} = \dot{\mathbf{A}}$). Therefore, a closing approximation between the second and the fourth order tensor is needed and discussed later in this Section.

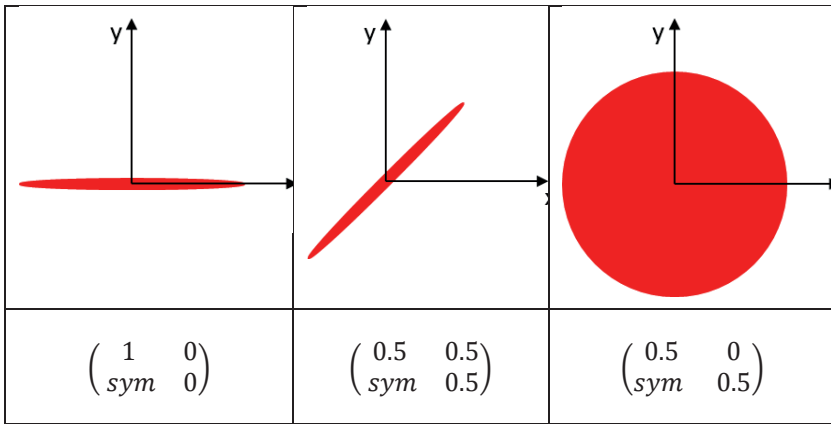


Figure 2-9: Fiber orientation distribution and the corresponding reduced 2D second order fiber orientation tensor

More precise measurements, considering the orientation distribution over the thickness and over the time, showed a development of different fiber orientations in the core and the shell layer which could not be predicted correctly by the Folgar-Tucker model. Based on the idea of the Strain Reduction Factor (SDF) which describes the local reduction of the strain due to resin rich “slip layers” with higher strains, the Reduced Strain Closure (RSC) was developed by Wang et al. [Wan08]. Therefore, the scalar reduction factor κ was introduced, which has a value between zero and one and needs to be fitted to experiments.

At the same time, new developments were done for the behavior of long fibers. In the basic Folgar-Tucker model, the interaction coefficient is a scalar value that models isotropic rotary diffusion. This is suitable for short fibers, but as long fibers cannot be assumed to be rigid, the interaction depends on the current fiber orientation. Therefore, the scalar value is replaced by a tensor, which can vary between the interaction of aligned and quasi-isotropic fiber orientations. Furthermore, this Anisotropic Rotary Diffusion (ARD) tensor

is flow type dependent (shear and extensional) [Phe09a]. This tensor contains five new parameters ($b_1 - b_5$), which need to be fitted to experiments.

As the RSC and the ARD extension is dealing with two separate effects of the fiber orientation evolution, the combination of both should be used for long fiber reinforced polymers such as SMC. The combined ARD-RSC Folgar-Tucker model has the form:

$$\dot{\mathbf{A}} = (\mathbf{W} \cdot \mathbf{A} - \mathbf{A} \cdot \mathbf{W}) + \xi (\mathbf{D} \cdot \mathbf{A} + \mathbf{A} \cdot \mathbf{D} - 2[\mathbf{A} + (1 - \kappa)(\mathbb{L} - \mathbb{M} : \mathbf{A})] : \mathbf{D}) + \dot{\gamma} [2[\mathbf{C} - (1 - \kappa)\mathbb{M} : \mathbf{C}] - 2\kappa \text{tr}(\mathbf{C})\mathbf{A} - 5(\mathbf{C} \cdot \mathbf{A} + \mathbf{A} \cdot \mathbf{C}) + 10[\mathbf{A} + (1 - \kappa)(\mathbb{L} - \mathbb{M} : \mathbf{A})] : \mathbf{C}], \quad (11)$$

with the ARD fiber interaction tensor:

$$\mathbf{C} = b_1 \mathbf{I} + b_2 \mathbf{A} + b_3 \mathbf{A}^2 + b_4 \frac{\mathbf{D}}{\dot{\gamma}} + b_5 \frac{\mathbf{D}^2}{\dot{\gamma}^2} \quad (12)$$

and the fourth order tensors \mathbb{L} and \mathbb{M} , which are analytical functions of the eigenvalues and eigenvectors of the second order fiber orientation tensor \mathbf{A} . They are defined as

$$\mathbb{L} = \sum_{i=1}^3 \lambda_i (\mathbf{e}_i \otimes \mathbf{e}_i \otimes \mathbf{e}_i \otimes \mathbf{e}_i) \quad (13)$$

and

$$\mathbb{M} = \sum_{i=1}^3 (\mathbf{e}_i \otimes \mathbf{e}_i \otimes \mathbf{e}_i \otimes \mathbf{e}_i). \quad (14)$$

Furthermore, the “:” represents the double dot product of the second and forth order tensors.

For the closure from the second fiber orientation tensor \mathbf{A} to the fourth order tensor \mathbb{A} , different approaches have been developed and tested. The linear closure approximation [Han62] gives exactly the fourth order tensor for an isotropic fiber orientation, but the accuracy is getting worse when it comes to aligned fiber orientations. The quadratic closure approximation developed by Doi [Doi81] and Lipscomb et al. [Lip88] uses the dyadic product of the second

order tensor with itself. This gives a good agreement for aligned fibers, but shows some nonphysical oscillation effect depending on the flow regime. Therefore, the linear and the quadratic closure approximation were combined in the hybrid closure approximation by Advani and Tucker [Adv90a]. Depending on the fiber orientation, a scalar value is used to interpolate between both approaches.

By showing the existence of an exact closure, if fiber-fiber-interactions are neglected [Lip88], the natural closure approximation was developed by Verleye et al. [Ver94]. This method uses a general expression for the fourth order tensor, which can be calculated by an analytical solution. Therefore, the natural closure values need to be fitted. This method showed a good agreement, but has some problems with singularities.

The orthotropic fitted closure approximation was developed by Cintra and Tucker [Cin95] and uses the assumption that the second and the fourth order tensor have the same principal direction and that the principal values of the fourth order tensor are a function of the second order tensor's eigenvalues. The parameters for this correlation were also fitted from experimental data and obtained from distribution function calculations. Due to nonphysical oscillations an improved version (ORW3) was proposed by Chung and Kwon [Chu01]. Due to the high number of parameters and the eigenvalue calculations, this method is very computational intensive.

To find a closure approximation which combines the accuracy of the eigenvalues methods with the relative low computational time of the natural closure approach, the Invariant Based Optimal Fitting closure approximation (IBOF) was developed by Chung and Kwon [Chu02]. This method uses a polynomial function of the invariants of the second order fiber orientation tensor. Therefore, the components of the fourth order tensor can be calculated using:

$$A_{ijkl} = \beta_1 S(\delta_{ij} \delta_{kl}) + \beta_2 S(\delta_{ij} A_{kl}) + \beta_3 S(A_{ij} A_{kl}) + \beta_4 S(\delta_{ij} A_{km} A_{ml}) + \beta_5 S(A_{ij} A_{km} A_{ml}) + \beta_6 S(A_{im} A_{mj} A_{kn} A_{nl}), \quad (15)$$

where S is a distribution function of the components in the fourth order Tensor \mathbb{A} , β_3 , β_4 and β_6 are coefficient depending on the second and third invariant of the second order fiber orientation tensor and β_1 , β_2 and β_5 are coefficients depending on the invariants and β_3 , β_4 and β_6 . For further details on these coefficients, it is referred to Chung et al. [Chu02]. As the coefficients β_3 , β_4 and β_6 are polynomial functions, each coefficient has 21 parameters. A total number of 63 parameters need to be fitted based on six known exact solutions of the fourth order tensor. This fitting was done for different thermoplastic short and long fiber materials by Phelps [Phe09b]. The parameter set for the long fiber reinforced thermoplastics (LFT) is used for SMC as well, since the fiber length and fiber volume fractions are in the same range.

Summarizing, the ARD-RSC becomes state of the art for long fiber reinforced polymers, since it has the best agreement with experiments. Furthermore, it has an acceptable parameter identification effort by fitting the five coefficients of the ARD fiber interaction tensor \mathbf{C} and the scalar reduction factor κ . For the closure approximation of the fourth order fiber orientation tensor \mathbb{A} , the IBOF closure is a good compromise between accuracy and computational time. The parameter determination for the IBOF closure is quiet complex, but due to the available parameter set, the combination of the ARD-RSC model with the IBOF closure is used in this work. Since the fiber orientation modeling is not the focus of this thesis, no further developments are done in this context.

2.5. Coupled-Eulerian-Lagrangian approach

To model a flow of material, a Lagrangian mesh based method can be used with some difficulty. As a high deformation is necessary, Lagrangian meshes might be distorted during the deformation and the Jacobian determinants might become negative. This could be overcome by remeshing the Lagrangian mesh, but this approach leads to a higher computational time, can introduce errors from the projection and can cause convergence problems. Therefore,

mainly Eulerian mesh formulations are used for fluid transport problems. Due to the convection of mass through the elements, the constitutive equation and its update can become complicated. Furthermore, the consideration of moving boundaries and interfaces is difficult. To overcome these drawbacks, a hybrid method was developed which combines the best of the Eulerian and the Lagrangian methods while minimizing their disadvantages. The Arbitrary Lagrangian Eulerian (ALE) method was first introduced by Noh [Noh63] and improved by Hirt et al. [Hir74]. Belytschko and Kennedy [Bel78a] showed the advantages of these ALE methods for three different use cases in 2D and 3D. They also showed the capability of the ALE formulation in terms of the fluid-structure-interaction [Bel78b] and Hughes et al. [Hug81]. This ALE method is distinguished by the mesh motion, which is separated from the material motion. Due to this separation of the material and the mesh motion, a material flow through the ALE mesh as well as a mesh deformation can occur. Depending on this mesh motion, the ALE approach is similar to the Eulerian method, if the mesh motion is set to zero, while it describes a Lagrangian formulation, if the mesh motion is equal the material motion [Bel14]. Furthermore, different dynamic, stress dependent mesh motions were investigated by Liu et al. [Liu91].

In this general ALE method, the material domain, the reference domain (mesh) and the spatial domain have to be described separately by defining the motion of the materials as:

$$\boldsymbol{x} = \boldsymbol{\phi}(\boldsymbol{X}, t), \quad (16)$$

with the material coordinate \boldsymbol{X} . Therefore, the function $\boldsymbol{\phi}(\boldsymbol{X}, t)$ maps the body from the initial configuration Ω_0 to the spatial domain Ω . Since both domains are not directly linked to the mesh deformation, the reference domain $\widehat{\Omega}$ is introduced in the ALE Continuum Mechanics (see Figure 2-10). Within this domain, the initial values of the particle motions $\boldsymbol{\chi}$ are denoted as:

$$\boldsymbol{\chi} = \boldsymbol{\phi}(\boldsymbol{X}, 0). \quad (17)$$

By introducing this reference domain $\widehat{\Omega}$, the motion of the material can be described mesh-independently. In most implementations, this domain is used to construct the initial mesh. Since the reference domain $\widehat{\Omega}$ typically remains coincident with the mesh, it is also the computational domain. To map the material motion from this reference domain to the spatial domain Ω , the function

$$\boldsymbol{x} = \widehat{\boldsymbol{\phi}}(\boldsymbol{\chi}, t) \quad (18)$$

is used. Therefore, the kinetics for the general ALE formulation and their simplifications towards the Lagrangian, and the Eulerian formation is given in Figure 2-11. For further information regarding the general ALE formulation, see the chapter “Arbitration Lagrangian Eulerian Formulations” in [Bel14].

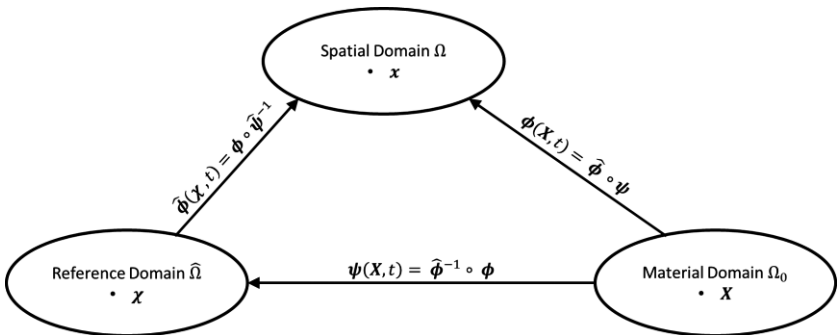


Figure 2-10: Maps between Lagrangian, Eulerian and ALE domain

Description		General ALE	Lagrangian	Eulerian
Motion	Material	$\mathbf{x} = \phi(\mathbf{X}, t)$	$\mathbf{x} = \phi(\mathbf{X}, t)$	$\mathbf{x} = \phi(\mathbf{X}, t)$
	Mesh	$\mathbf{x} = \hat{\phi}(\boldsymbol{\chi}, t)$	$\mathbf{x} = \phi(\mathbf{X}, t)$ $(\boldsymbol{\chi} = \mathbf{X}, \hat{\phi} = \phi)$	$\mathbf{x} = \mathbf{I}(\mathbf{x})$ $(\boldsymbol{\chi} = \mathbf{x}, \hat{\phi} = \mathbf{I})$
Displacement	Material	$\mathbf{u} = \mathbf{x} - \mathbf{X}$	$\mathbf{u} = \mathbf{x} - \mathbf{X}$	$\mathbf{u} = \mathbf{x} - \mathbf{X}$
	Mesh	$\hat{\mathbf{u}} = \mathbf{x} - \boldsymbol{\chi}$	$\hat{\mathbf{u}} = \mathbf{x} - \mathbf{X} = \mathbf{u}$	$\hat{\mathbf{u}} = \mathbf{x} - \mathbf{x} = \mathbf{0}$
Velocity	Material	$\mathbf{v} = \mathbf{u}_{,t[X]}$	$\mathbf{v} = \mathbf{u}_{,t[X]}$	$\mathbf{v} = \mathbf{u}_{,t[X]}$
	Mesh	$\hat{\mathbf{v}} = \hat{\mathbf{u}}_{,t[\boldsymbol{\chi}]}$	$\hat{\mathbf{v}} = \hat{\mathbf{u}}_{,t[\mathbf{x}]} = \mathbf{v}$	$\hat{\mathbf{v}} = \hat{\mathbf{u}}_{,t[\mathbf{x}]} = \mathbf{0}$
Acceleration	Material	$\mathbf{a} = \mathbf{v}_{,t[X]}$	$\mathbf{a} = \mathbf{v}_{,t[X]}$	$\mathbf{a} = \mathbf{v}_{,t[X]}$
	Mesh	$\hat{\mathbf{a}} = \hat{\mathbf{v}}_{,t[\boldsymbol{\chi}]}$	$\hat{\mathbf{a}} = \hat{\mathbf{v}}_{,t[\mathbf{x}]} = \mathbf{a}$	$\hat{\mathbf{a}} = \hat{\mathbf{v}}_{,t[\mathbf{x}]} = \mathbf{0}$

Figure 2-11: Comparison of the kinetic for an ALE formulation with Lagrangian and Eulerian description [Bel14]

The Coupled-Eulerian-Lagrangian (CEL) Method is a special ALE formulation, in which the Lagrangian formulation is combined with an ALE formulation (see Figure 2-12). This is done to improve the interaction of the flowable material with the Lagrangian solid material. Therefore, the contact and moving boundary conditions are treated in the Lagrangian step. By coupling an ALE step with an Eulerian element formulation to this step, high deformations can be realized. By using a negative mesh motion in this ALE step, which is reverse to the material motion, the mesh stays the same. As a consequence, the final configuration is comparable to the Eulerian formulation. Different methods of remeshing were investigated by Huerta and Liu [Hue88]. For this remapping, they use an approximation of the fluid boundary surface in the deformed configuration. Based on this idea, various further works were focusing on the reduction of the computational effort due to new terms in the formulation for special geometries [Ben89], [Ben92]. Besides the numerical remeshing, the material point information needs to be transported due to the material convection. Therefore, Liu et al. [Liu86] developed the convection equation to fulfill the mass conservation by using the Lax-Wendroff method [Lax60].

For further information regarding the operation of the Eulerian, the Eulerian operator splitting and the Lagrangian step see Benson et al. [Ben04] and Donea et al. [Don04].



Figure 2-12: Lagrangian and Eulerian Steps in the CEL approach [Ben04]

The interaction in the Lagrangian step is done by using a penalty function. Therefore, the penetration length g between the element edges or the interpolated surface of the material in the Eulerian elements and the interaction surface is calculated (see Figure 2-13). The resulting penalty force depends on the exact formulation of the penalty function, but it is defined normal to the interaction surface towards the material. For an unambiguous description of this penalty force direction, it is recommended to use solid interaction elements as they have a distinctive surface direction. Furthermore, at least three Eulerian elements behind the Lagrangian contact surface are needed to prevent a loss of mass over insufficient boundary conditions.

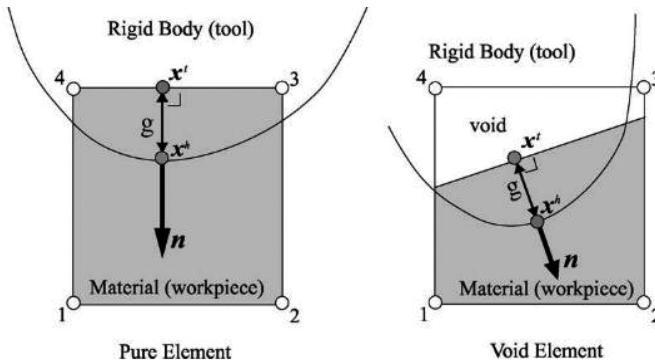


Figure 2-13: Definition of the penetration for pure and void elements [Ben04]

The current focus of research regarding the ALE and CEL methods has two main targets: the simulation of cracks in a structural simulation and the development of special material models in the fluid simulation. Since the ALE and CEL formulation are not limited to fluids, research for high deformation structural simulation was also done. Currently, combination with XFEM methods leads to new application areas. For example the prediction of crack propagations due to contact is simulated by Vitali and Benson [Vit08]. On the other side, the ALE and CEL formulations are improved for special applications and material combinations. Therefore, a multi-physics and multi-material code is developed to simulation the interaction of plasma to solid materials by Koniges et al. [Kon15].

In this thesis, the commercial available CEL framework within Abaqus is used. Therefore, no further developments or implementations of the CEL formulation need to be done. Since the CEL implementation within Abaqus offers most of the user subroutines, the focus is on the material model development and the corresponding CEL specific simulation parameter identification.

3. Rheological measurements and rheological modelling

In this chapter the rheological measurements, the rheological modelling and the evaluation of different SMC materials is presented. Therefore, the measurement method is described in Section 3.1. In the next Section, the experimental investigated are presented and measurement results are shown. In Section 3.3 and 3.4, the compressibility and rheological models are developed. In Section 0, the correlation between the material parameters for the different materials and their composition is elaborated.

Most of the content of this chapter 2 has been published predominantly in the publications [Hoh17a], [Hoh17b], [Hoh17c].

3.1. Rheological tool and experimental setup

As discussed in Section 2.3, typical shear or rotational rheometers cannot be used for the rheological characterization of SMC, since the fiber length of SMC is in the same range as the typical sample size. Furthermore, SMC has a different flow behavior compared to other thermoplastic and thermoset composite materials in the injection molding or compression molding process (cf. Section 2.2). Therefore, not all necessary material parameters can be determined by using a classical rheometer method.

The first characterization of SMC by using an SMC tool was performed by Castro and Griffith [Cas89] and improved by Dumont et al. [Dum03], [Dum07], [Gui12] (cf. Section 2.3). Based on their experiments a new rheological tool was developed at the Fraunhofer Institute for Chemical Technology (ICT), Pfintzal, Germany. The design of the new rheology tool was driven by the two targets of having a long 1D flow of the SMC and the ability to measure the

pressure distribution over the flow length. Both targets were deduced from the goal to observe the changes in the material properties over the flow length and over time. To enable a long flow length, the rheology tool has a rectangular cavity of 800 mm x 250 mm (see Figure 3-1) and can produce plates between 1 mm and 5 mm thickness. By changing the initial charge, mold coverage between 20 % and 80 %, different flow-lengths and their characteristics can be observed. [Hoh17a]

For a precise rheological measurement, the knowledge of the time- and location-resolved pressure distributions are important. To gain this pressure information, seven pressure sensors are placed in the lower mold part along the flow path (e_1) (cf. Figure 3-1). They are centered vertically to the flow direction in the symmetry line of the tool ($e_2 = 0$). Figure 3-1 shows the exact position of these sensors, which were mounted flush. These sensors are not distributed equally as the tool contains a replaceable inlay in the center area and therefore, no sensors could be placed at the transition between the tool and the inlay. Furthermore, Sensor 1 and 7 are not equally spaced to the tool sides, since the short tool side is replaceable and so the distance needs to be increased to protect Sensor 1.

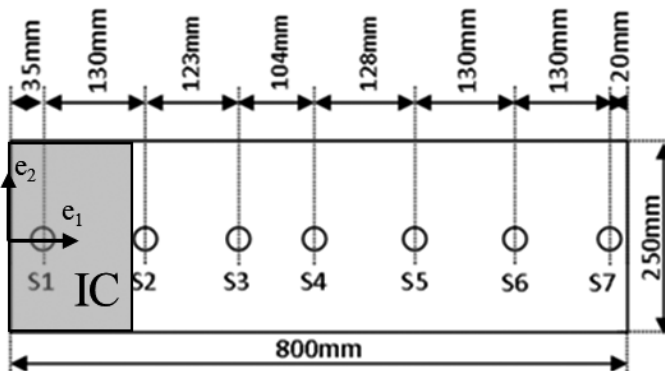


Figure 3-1: Position of the SMC initial charge and the pressure sensors along the lower mold part of the rheological tool [Hoh17a]

Besides the pressure information, the press data like the current press working force and the position of the parallelization-equalizing cylinders are necessary for the rheological characterization. Therefore, the internal press system is linked to the same data logging system as the pressure sensors. With this experimental setup, it is possible to record all necessary data simultaneously (see Figure 3-2).

This experimental setup was used at two Dieffenbacher presses at the Fraunhofer ICT. The bigger Dieffenbacher COMPRESS PLUS DCP-G 3600/3200 AS has a maximum working pressure of 36 000 kN and a maximum closing speed of 80 mm s⁻¹. The smaller Dieffenbacher DYL 630/500 has a maximum working pressure of 6 300 kN and a maximum closing speed of 18 mm s⁻¹.

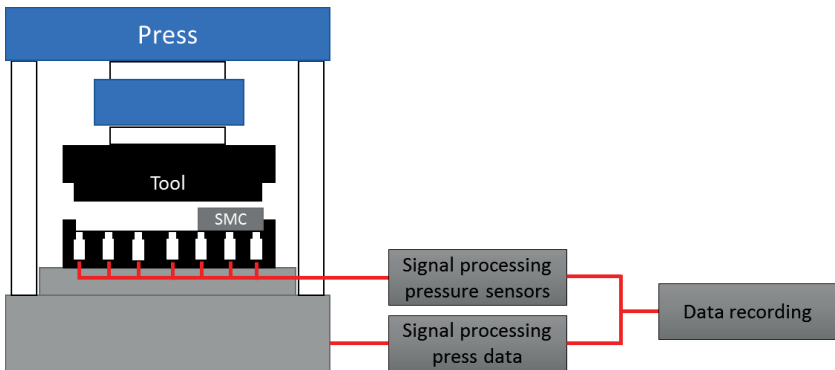


Figure 3-2: Experimental setup for the rheological measurements

3.2. Rheological measurements of different SMC materials

During the experiments, materials with different resin types, fillers and fibers were investigated. All these SMCs were compounded at Fraunhofer ICT in Pfinztal, Germany, on a modified HM-LB-800 Schmidt & Heinzmann SMC line

(cf. Section 2.1). The detailed description of the five investigated SMC formulations (Class-A SMC, the Low-Density Class-A SMC, Vinylester SMC and the UPPH carbon and glass fiber SMC) follows within this Section. For each SMC formulation a short description of the material composition is given. This is followed by a description of the process parameters and a presentation of a reference pressure distribution plot for the same closing speed of $\dot{h} = 1 \text{ mm s}^{-1}$.

3.2.1. Standard Class-A SMC

This first SMC, which is investigated, is a typical Class-A SMC for exterior parts with a paintable surface. It has a high amount of fillers to reduce shrinkage and material costs while increasing the density only slightly. The resin-filler mixture (see Table 3-1) has a density of $\rho_{\text{Class-A, paste}} = 1.69 \text{ g cm}^{-3}$. The semi-finished product was produced with a fiber content of 20 vol.-% chopped glass fibers (27 wt. %) with a fiber length of 1 inch (25 mm). The fibers used for the SMC are a 12 k MultiStar® 272 from Johns Manville (filament diameter $d = 13.5 \text{ }\mu\text{m}$, 4800 tex). As filler, calcium carbonate (CaCO_3 , chalk) is used. Due to its low price, this is a typical filler for Class-A SMC formulations (see Section 2.1). The final semi-finished material has a density of $\rho_{\text{Class-A}} = 1.85 \text{ g cm}^{-3}$. The exact composition of this Class-A SMC is given in Table 3-1.

Table 3-1: Composition of the paste of the Class-A SMC

Component	Trade name	Quantity
UP resin	Palapreg Premium G21	100 parts
Adherent and flow aids	BYK 996 + BYK A 560	2.2 parts
Peroxide	Pergan Peroxid BEC	1.5 part
L&V 50%MgO	LuvatoI® MK35	2.5 parts
Filler: calcium carbonate (CaCO ₃)	Omya Millicarb® OG	190 parts

The experiments with this Class-A SMC were performed using an initial mold coverage of 37.5 % (300 mm x 250 mm). The room-tempered initial charge was assembled out of four single sheets and had an average thickness of $h_0 = 8.4$ mm. The mold was tempered to 150 °C for the upper side and to 160 °C for the lower side. Due to the different thermal expansions at the upper and lower tool sides, this helped to prevent both tool sides to touch each other at the flush faces. Furthermore, these settings helped to balance temperature differences due to convection. [Hoh17b]

All compression molding experiments for this material were performed with a constant closing speed of $\dot{h} = 1$ mm s⁻¹, which was predefined directly in the press control. To prevent too high pressure in the cavity and therefore, to protect the pressure sensors, the maximum working force was limited to 2 000 kN. This leads to a reduction of the closing speed at the end of the compression molding process at a relative gap height of 0.25 mm (see Figure 3-3).

The pressure distribution and the press working force over the relative gap height ($h - h_f$) is plotted in Figure 3-3), where h is the current height and h_f is the final height of the plate. This type of plotting enables an easier comparison of the slightly different flows and initial charges. [Hoh17b]

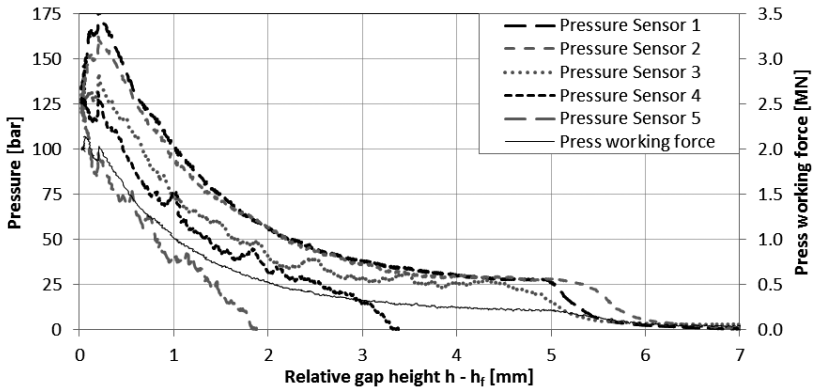


Figure 3-3: Exemplary pressure distribution of the standard Class-A SMC for a closing speed of $h = 1 \text{ mm s}^{-1}$

The pressure distributions of all 10 measurements are following the same pressure pattern. The Sensors 1 to 3 were covered by the initial charge. Therefore, these sensors show an immediate pressure increase, as soon as the upper mold side is touching the initial charge material. The Sensor 4 right behind the initial charge (in flow direction) can be used to monitor the start of the material flow. By comparing the gap heights of the first pressure increase of this reference sensor and the one of Sensor 1, an offset between these gap heights can be observed. This offset distance can be attributed to a short compression or squish [Old04] phase at the beginning of the mold filling process. After this transversal compression (e3), the flow of the SMC starts and the pressure at Sensor 1 reaches a threshold at a relative gap height of approx. 5 mm. During the following stable plug-flow, the pressure at Sensor 1, 2 and 3 is increasing throughout [Hoh17b]. After the press working force reaches its maximum, at a relative gap height of approximately 0.25 mm, the pressure values of the sensors are decreasing due to the reduced closing speed.

3.2.2. Low-Density (LD) Class-A SMC

The second SMC formulation is a Low-Density (LD) Class-A SMC. This LD Class-A SMC has a lower density compared to the previous standard SMC due to micro hollow glass spheres, which have a diameter of 40 μm and a density of 0.38 g cm^{-3} . The formulation was developed by the Fraunhofer ICT during the Technologie-Cluster Composites “InnoSMC” [Kec16]. Using the composition from Table 3-2, the density of the paste was reduced to $\rho_{\text{LD-Class-A, paste}} = 1.09 \text{ g cm}^{-3}$. The resin types for the Class-A and the LD Class-A SMC are not the same, as the resin producer was not offering the same resin type anymore. By evaluating the successor resin, no differences could be found and therefore, the resins can be considered to have similar behavior. The semi-finished SMC was produced at the Fraunhofer ICT with a fiber content of 20 vol.-% (38 wt.-%) and a density of $\rho_{\text{LD-Class-A}} = 1.38 \text{ g cm}^{-3}$. As for the Class-A SMC, chopped 12 k MultiStar® 272 from Johns Manville with a fiber length of 1 inch (25 mm) is used for this SMC.

This LD Class-A SMC has nearly the same mechanical properties as the standard Class-A SMC, while the costs increasing only slightly [Kec16]. Since the material still has a Class-A quality at reduced density, it becomes interesting to the automotive industry.

Table 3-2: Composition of the paste of the Low-Density Class-A SMC [Kec16]

Component	Trade name	Quantity
UP resin	Palapreg Premium G22-01 LE	100 parts
Adherent and flow aids	BYK W9010	3 parts
Styrol	-	7 parts
Peroxide	Palapreg Premium G21- 01LE Cure	1 part
L&V 50%MgO	LuvatoI® MK35	2.77 parts
Filler: calcium carbonate (CaCO ₃)	Omya Millicarb® OG	105 parts
Filler: micro hollow glass spheres	3M VS5500	28 parts

The LD Class-A SMC measurements were conducted with nearly the same process settings as the Class-A SMC. Due to the slightly increased thickness of the semi-finished product, the initial charge coverage was reduced to 36.25 % (290 mm x 250 mm) to gain the same final plate thickness of $h_f = 3$ mm by iterative changing the initial charge dimensions. The initial charges were assembled from four single sheets which had a total thickness of $h_0 = 9$ mm. A representative pressure distribution for this material composition is plotted in Table 3-5.

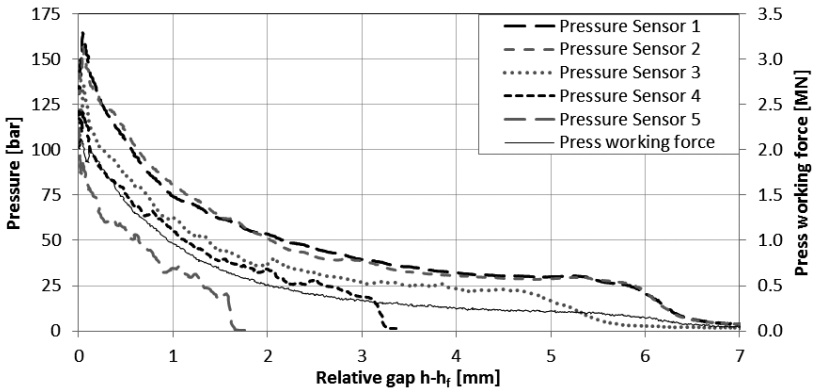


Figure 3-4: Exemplary pressure distribution of the LD Class-A SMC for a closing speed of $\dot{h} = 1 \text{ mm s}^{-1}$ [Hoh17b]

As the pressure distribution is following the same pressure pattern as that of the Class-A SMC, referred to in the previous Section, for the discussion of the pressure pattern. The slight differences of the first pressure increases of Sensor 1 to 3 (cf. Figure 3-4 and Figure 3-5) can be explained to be the slightly changing initial charge length and the wavy surface of the initial charge. These non-homogenous thickness distributions lead to a different relative gap height of the first pressure increase.

3.2.3. Vinylester (VE) SMC

The Vinylester (VE)-SMC was developed within the International Research Training Group (IRTG) GRK 2078 "Integrated engineering of continuous-discontinuous long fiber reinforced polymer structures" by the Fraunhofer ICT. The objective was to develop a material formulation for semi-structural applications. Therefore, the fiber volume content is increased, while the fillers are omitted. Furthermore, the material should be able to crosslink with the local unidirectional reinforcements during the molding process. Therefore, a VE resin is used.

In this context, the term semi-structural material is used to indicate material properties between the Class-A SMC and unidirectional reinforcement composites, which are used for structural applications. The semi-structural material needs local reinforcements or geometrical stiffeners to be used in structural applications. [Hoh17b]

The composition of the VE-SMC paste is given in Table 3-3. The density of the paste is dominated by the resin with a density of $\rho_{VE-SMC, paste} = 1.10 \text{ g cm}^{-3}$ as no fillers were used. The fiber content is set to 22.7 vol.-% (41 wt.-%) of 1 inch (25 mm) chopped glass fibers. Once again, the MultiStar® 272 from Johns Manville is used. The final semi-finished product has a density of $\rho_{VE-SMC} = 1.42 \text{ g cm}^{-3}$.

Table 3-3: Composition of the paste of the semi-structural VE SMC

Component	Trade name	Quantity
VE resin	Atlac XP810X	100 parts
Adherent and flow aids	BYK 9085	2 parts
Peroxide	Trigonox 117	1 part
L&V 50%MgO	Luvatol EK 100KM	4.2 parts

During the first molding trials, the VE-SMC showed a higher flowability than the Class-A SMC formulations with fillers. Therefore, the initial charge coverage was reduced to 20 % (160 mm x 250 mm) to investigate the viscosity over a longer flow length. Due to the decrease of the initial charge coverage, eight single SMC sheets were needed to be assembled, with a total height of $h_0 = 10.1 \text{ mm}$. This leads to a final plate thickness of $h_f = 2 \text{ mm}$.

The experiments were performed with the same mold temperatures, 150 °C for the upper and 160 °C for the lower side. The closing speed was set to

$\dot{h} = 1 \text{ mm s}^{-1}$, but also molding trials with different constant deformation rates of $D = 0.5 \text{ s}^{-1}$, 1.0 s^{-1} and 2.0 s^{-1} were performed. The deformation rate D is defined as the ratio between the closing speed \dot{h} and the current gap height h :

$$D = \frac{|\dot{h}|}{h}. \quad (19)$$

To define the nominal deformation rate during the molding process, the closing speed was prespecified over the height. During these trials, the closing speed varied between $\dot{h}_{\max} = 20 \text{ mm s}^{-1}$ and $\dot{h}_{\min} = 1 \text{ mm s}^{-1}$. Due to the industrial scale press and the mold size, the nominal deformation rate could not be held constant until the end of the filling process, because the press switches from velocity based control to pressure based control at the end of the compression molding process. Thus, the pressure values from sensors 5 to 7 (fast mold closing), or 6 to 7 (slower mold closing) could not be used for the deformation-rate-dependent experiments, since the deformation gradient decreases significantly after the switching point. [Hoh17a]

Since the experiments were performed with higher closing speeds (see Table 3-4), the maximum press working force had to be reduced to 1 600 kN to protect the pressure sensors. The process settings and the relevant information for all experiments performed with the VE-SMC are listed in Table 3-4. A representative pressure distribution for this SMC with a constant closing speed of $\dot{h} = 1 \text{ mm s}^{-1}$ is plotted in Figure 3-5.

Table 3-4: Press settings of the VE-SMC molding trials [Hoh17a]

Molding Trial	Press setting	Closing speed [mm s ⁻¹]	Nominal deformation rate [s ⁻¹]	Sensors within setting range
D = 0.5 s ⁻¹	Constant deformation rate	2.5 - 5.3	0.5	1 - 5
D = 1.0 s ⁻¹	Constant deformation rate	5.0 - 10.5	1.0	1 - 4
D = 2.0 s ⁻¹	Constant deformation rate	10.2 - 20.2	2.0	1 - 4
v = 1.0 mm s ⁻¹	Constant closing speed	1.0	0.35 - 0.11	1 - 7

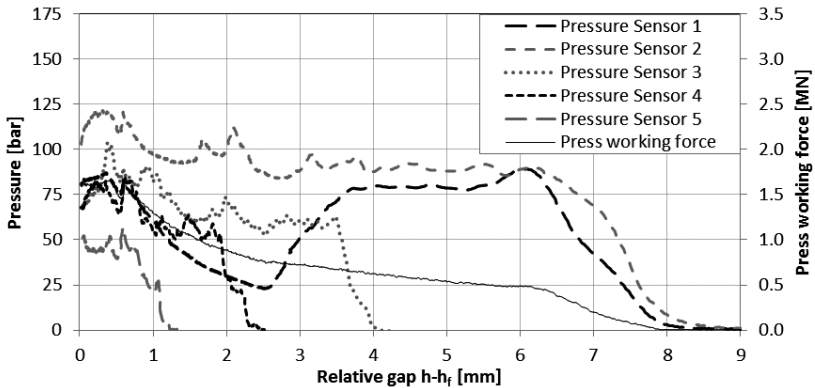


Figure 3-5: Exemplary pressure distribution of the VE-SMC for a closing speed of $\dot{h} = 1 \text{ mm s}^{-1}$

The pressure distribution of the VE-SMC generally behaves in the same way as the previous SMC formulation. Nonetheless, differences in the threshold

pressure values and in the pressure increase in the flow phase can be observed. One clear difference is the pressure progression of Sensor 1. This has no SMC material specific reason, but a technical cause. It can be traced back to a problem with the tool. After the experiments with the Class-A SMCs, the short pegboard next to sensor 1 was damaged and the clearance between the mold sides was slightly increased. Due to this higher clearance, the tightness between both mold sides is not given and a slight flow occurs through this clearance. While closing the tool, the clearance is decreased and the fully cavity function is recovered. The loss of material can be neglected for the following steps, since it is very low. [Hoh17a], [Hoh17b]

Since the pressure pattern shows the same characteristics as the Class-A SMCs, see Section 3.2.1 for the detailed discussion.

3.2.4. Unsaturated Polyester Polyurethane Hybrid resin (UPPH) glass fiber SMC

The UPPH glass fiber SMC was also developed within the International Research Training Group with the same aims as the semi-structural VE-SMC. As the VE-SMC showed a tendency to foam during the molding process, the mechanical properties were not in the designated range. Therefore, the resin system was replaced and an unsaturated polyester polyurethane hybrid resin (UPPH) is used. Within the International Research Training Group, the overall scope is the combination of SMC with local continuous unidirectional (UD) reinforcements. Therefore, also UD-SMC materials were developed. For these reinforcements, the same UPPH resin is used since it has a B-stage, which enables a preforming and a rapid precuring to fixate the shape. Due to this, also the UPPH SMC semi-finished product can be aged in a shorter time than conventional SMCs [Büc16], [Büc17].

The UPPH resin based paste has a density of $\rho_{\text{UPPH-SMC, paste}} = 1.08 \text{ g cm}^{-3}$. Its composition is given in Table 3-5. The fiber content of the UPPH glass fiber SMC is 23 vol.-% (41 wt.-%) of the same 1 inch (25 mm) chopped fibers from

Johns Manville (MultiStar® 272) as the previous SMC formulations. This leads to a density of the semi-finished product of $\rho_{\text{UPPH-G-SMC}} = 1.42 \text{ g cm}^{-3}$.

Table 3-5: Composition of the paste of the semi-structural UPPH SMC

Component	Trade name	Quantity
UPPH resin	Daron ZW 14142	100 parts
Adherent and flow aids	BYK 9085	2 parts
Impregnation aid	BYK 9076	3 parts
Deaeration aid	BYK A-530	0.5 parts
Inhibitor	pBQ	0.03 parts
Peroxide	Trigonox 117	1 part
Isocyanate	Lupranat M20R	24.2 parts

The compression experiments were performed in the same way as the trials for the semi-structural VE-SMC. The initial coverage was also set to 20 % (160 mm x 250 mm). Since the final plates should be used for mechanical testing, the final plate thickness was $h_f = 3 \text{ mm}$. Therefore, the initial charge had a thickness of $h_0 = 18 \text{ mm}$ and was assembled from 16 single sheets.

Due to the change of the resin, the mold surface temperature had to be adjusted. Therefore, the upper tool was tempered to 140 °C and the lower tool to 145 °C. The experiments were performed with a constant closing speed of $\dot{h} = 1 \text{ mm s}^{-1}$ and different constant nominal deformation rates of $D = 0.1 \text{ s}^{-1}$, 0.25 s^{-1} , 0.5 s^{-1} and 1.0 s^{-1} . Due to the increase of the initial charge volume, the maximum press force has been increased to 3 000 kN. During the experiments with the high deformation rates, a higher closing speed compared to

the previous experiments occurred due to the higher initial thickness. Therefore, the press pressure limit was reached too early for some experiments of this series. An exemplary pressure distribution of this semi-structural UPPH glass fiber SMC and a constant closing speed of $\dot{h} = 1 \text{ mm s}^{-1}$ is plotted in Figure 3-6.

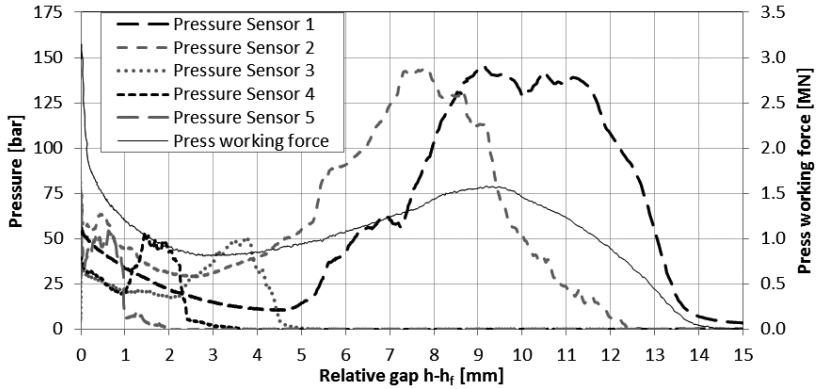


Figure 3-6: Exemplary pressure distribution of the UPPH glass fiber SMC for a closing speed of $\dot{h} = 1 \text{ mm s}^{-1}$

The pressure distribution for the UPPH glass fiber SMC shows a significantly different behavior compared to the other SMC formulations. At the beginning of the flow phase, a high pressure at Sensor 1 and Sensor 2 is recorded until the pressure reaches a threshold at a relative gap height of 9 mm. This threshold is at a three times higher level than the pressure at the end of the molding process. Compared to the UPPH carbon fiber SMC (see Section 3.2.5), this threshold is approx. four times higher. Since the press working pressure is increasing at the same time, this is not just a local effect at the locations of the pressure sensors, but also a global effect throughout the whole material at that time. After this threshold, the pressure is decreasing until it proceeds in the same way as the carbon SMC. From a relative gap height of approx. 3 mm onwards, the pressure values of Sensor 1 and 2 are increasing again and

following the typical pressure pattern. The lower pressure values of Sensor 1 compared to Sensor 2 can be explained once again by the damaged pegboard. Since the total pressure in the cavity is higher for this experiment, the material is still flowing and therefore, not curing occurs in the gap. Therefore, the pressure at Sensor 1 is lower over a larger range. Still, the amount of material flow through the gap is so small, that it can be neglected. [Hoh17c]

The effect of this local pressure peak is not only appearing at the beginning of the flow phase, but also at the flow front along the hole molding process. Sensor 3 to Sensor 5 also show this behavior when the flow front is reaching them, but with a lower amplitude. [Hoh17c]

3.2.5. UPPH carbon fiber SMC

The UPPH carbon fiber SMC was developed together with the UPPH glass fiber SMC. Both semi-structural SMC are based on the same paste (see Table 3-5). In contrast to the UPPH glass fiber SMC (see 3.2.4), the fiber content was increased to 42 vol.-% (55 wt.-%) of chopped carbon fibers. The 50k carbon fiber PX 35 from Zoltek was chopped to 1 inch (25 mm) long fibers. This leads to a density of the semi-finished product of $\rho_{\text{UPPH-C-SMC}} = 1.39 \text{ g cm}^{-3}$.

The compression experiments were performed in the exact same way as the experiments for the UPPH glass fiber SMC. As the single carbon fiber SMC sheets are slightly thinner than the glass fiber sheets, the initial stack were assembled out of 18 single sheets. Due to the higher material costs, molding trials were only done for one constant closing speed of $\dot{h} = 1 \text{ mm s}^{-1}$ and one constant nominal deformation rate of $D = 0.25 \text{ s}^{-1}$. An exemplary plot of the pressure distribution of this SMC for a constant closing speed of $\dot{h} = 1 \text{ mm s}^{-1}$ is plotted in Figure 3-7.

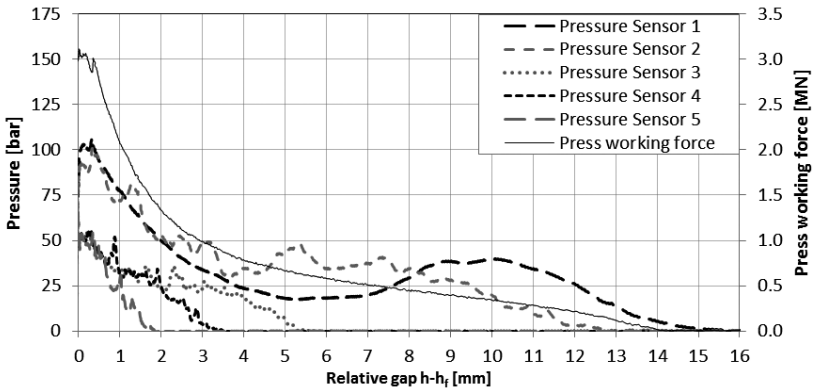


Figure 3-7 Emplary pressure distribution of the UPPH carbon fiber SMC for a closing speed of $\dot{h} = 1 \text{ mm s}^{-1}$ [Hoh17b]

The pressure distribution of this UPPH carbon fiber SMC follows the typical SMC pressure pattern – refer to Section 3.2.1 for the detailed discussion. The pressure drop of Sensor 1 after the relative gap height of 8.5 mm can be traced back to the problem with the damaged pegboard once again (cf. Section 3.2.3).

3.3. Compressibility of SMC during flow

In this Section, the compressibility of the different material formulations during the molding process is investigated. Since the SMC was assumed to be incompressible in most previous works (see. Section 2.3), the first material characterized in this Section is the VE-SMC, as the compressibility is first observed. Based on this, the other SMC material formulations are then systematically examined.

3.3.1. Vinylester SMC formulation [Hoh17a]

Figure 3-8 (a) and Figure 3-8 (b) show the pressure distributions of the VE-SMC for Sensors 1 and 4, respectively, for the three different deformation rates $D = 0.5 \text{ s}^{-1}$, 1.0 s^{-1} and 2.0 s^{-1} . Within these plots it can be observed, that the relative gap heights, where the pressure is increasing, are changing with the different nominal deformation rates. Considering the effects described in the previous Section, the current averaged flow front position can be determined and used in a correlation with the current gap height. By using the sensor positions l_{S_x} of sensor S_x , representing the position of the current melt front, and the current gap height $h(t)$, the current volume of the SMC melt can be calculated as

$$V(t) = l_{S_x} \cdot h(t) \cdot b, \quad (20)$$

where b is the width of the mold and x the number of the sensor. Dividing the current volume change by the initial charge volume, the relative volume change β can be calculated by

$$\beta(t) = \frac{1}{V} \left(\frac{\partial V}{\partial t} \right) = \frac{V(t) - V_0}{V_0 \Delta t} = \frac{l_{S_x} h(t) - l_0 h_0}{l_0 h_0 (t - t_0)}, \quad (21)$$

where t_0 represents the time when the press is touching the SMC initial charge for the first time.

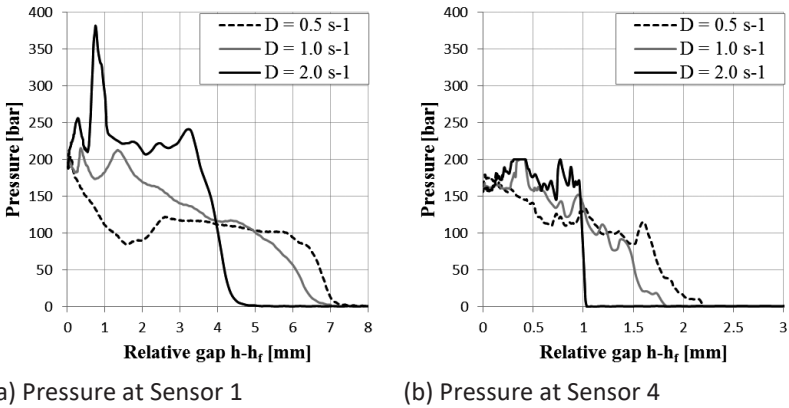


Figure 3-8: Compression molding experiments of the VE-SMC: pressure over relative gap height for (a) Sensor 1 and (b) Sensor 4 for different nominal deformation rates ($D = 0.5 \text{ s}^{-1}$, 1.0 s^{-1} and 2.0 s^{-1})

The relative volume change over the real flow length is plotted in Figure 3-9 for all constant nominal deformation rates. The first sensor reached by the SMC flow is Sensor 2 (S_2), with a position of $l_{S_2} = 165 \text{ mm}$, which is in the transition between the squish and the flow phases (cf. Section 3.2.1 and 3.2.3). The last sensor value plotted in Figure 3-9 is the last one with a constant nominal deformation rate, before the press is switching from speed to pressure control. Since higher closing speeds lead to higher press forces, the switching point is reached earlier for higher nominal deformation rates. This can be recognized in the diagrams by the time, the maximum pressure threshold is reached at the end of the compression phase.

The graphs plotted in Figure 3-9 show that the nominal deformation rate has a high effect on the volume change, where the first measuring point (Sensor 2, $l = 165 \text{ mm}$) does not represent the initial charge volume change, but the change after a short flow. After the mold is touching the material, different compressibility behaviors can be observed. For small nominal deformation rates ($D = 0.5 \text{ s}^{-1}$), a volume increase was measured, while it decreases for

higher nominal deformation rates. This variation can be attributed to the different closing speeds and therefore different temperature and pressure distributions during the squish phase. Higher closing speeds lead to higher extensional viscosity (see eq. 5) and therefore to a higher pressure in the material. Especially during the squish (compaction) phase, this leads to a compaction of the material whereby the compression of air entrapments might have the biggest effect. Furthermore, for small nominal deformation rates, the initial charge has a longer contact with the lower molding tool (1 s, +10% contact time), so the temperature is slightly higher. This increases the release of styrene and therefore a volumetric increase can occur. Additionally the void and gas entrapments content might change, like shown by Comte et al. [Com06] and Lee et al. [Le08].

At the beginning of the flow phase, the tendency from the squish (compaction) phase is the same, but approximately after a flow length of 240 mm (at Sensor 4, $l = 392$ mm), the volume change reaches a threshold at $\beta = 0 \text{ s}^{-1}$.

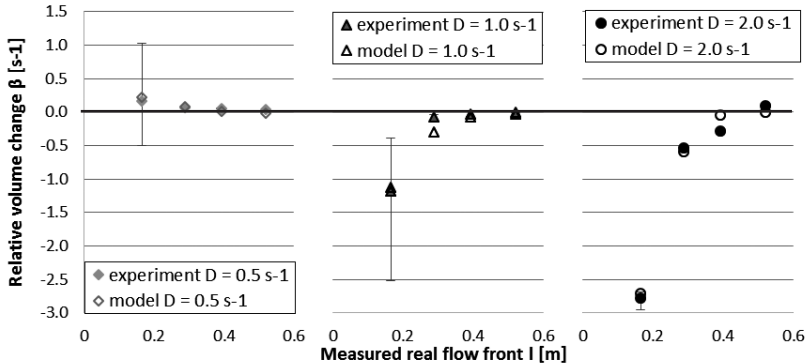


Figure 3-9: Comparison of the relative volume change β of the VE-SMC between measurement and modelling for three nominal deformation rates $D = 0.5 \text{ s}^{-1}$, 1.0 s^{-1} and 2.0 s^{-1} during the molding process [Hoh17a]

This behavior clearly shows that this semi-structural SMC material cannot be assumed as incompressible. The most common approach to describe the resulting volume change induced by a pressure is to use the bulk modulus. Since the bulk viscosity can only describe a volumetric decrease due to a pressure increase, this method is not suitable for this case. Another approach to describe the volume change is to use an empirical model to predict the changes during the flow. By evaluating the experimental data (compare Figure 3-8), it could be observed that the relative volume change β depends on the deformation rate and the flow length. Combining this with a power-law estimation and an empirical evaluation, the following empirical equation is evolved by fitting different equation terms:

$$\beta(t, D(t)) = \alpha_1 \left(\frac{l_{max} - l_{incomp}(t)}{l_{def}} \right)^k (D_c - D(t)) - \frac{\alpha_2 (D_c - D(t))(t - t_0)}{\left(\frac{l_{incomp}(t) - l_0}{l_{def}} \right)^l}, \quad (22)$$

with $l_{def} = 1\text{m}$, the incompressible flow front position l_{incomp} defined by the mass balance equation as

$$l_{incomp}(t) = \frac{l_0 h_0}{h(t)}, \quad (23)$$

with the power-law parameters k and l , the fitted volume change factor α_1 and α_2 and the deformation rate D_c , where the compressibility is changing from a volume decrease to a volume increase. The comparison between the measurements and the empirical model are plotted in Figure 3-9.

3.3.2. Class-A SMC formulations

After showing the compressibility of the VE-SMC, also the other SMC formulations are evaluated. In Figure 3-10, the averaged experimental relative volume changes β are plotted for both Class-A materials and a constant closing speed of $\dot{h} = 1 \text{ mm s}^{-1}$. As the relative volume change is nearly zero over the whole flow length, the Class-A SMC formulations can be assumed to be incompressible.

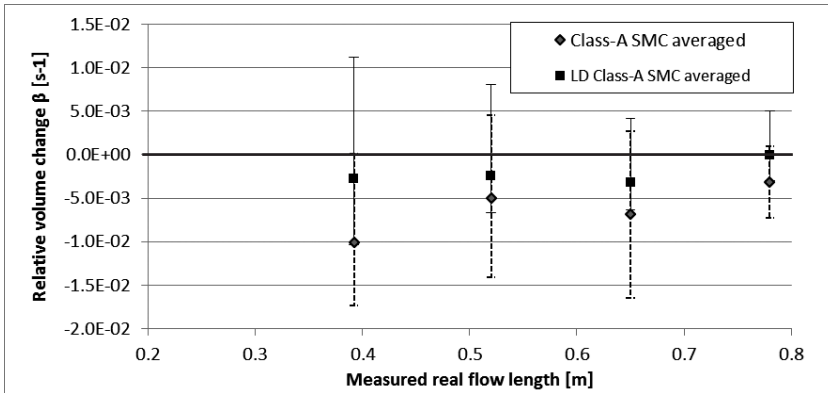


Figure 3-10: Averaged relative volume change β from the Class-A SMCs experiments for a constant closing speed of $\dot{h} = 1 \text{ mm s}^{-1}$

3.3.3. UPPH SMC formulations

For the UPPH glass fiber SMC, the evaluation of the relative volume change was only possible for the constant deformation rate of $D = 0.25 \text{ s}^{-1}$. For the other test series, the fingering effect was too high. The fingering effect describes the statistically forming of faster flowing “fingers”, due to local variation of the viscosity [Yad11]. This effect can be recognized in Figure 3-6 for the sensors 3, 4 and 5: While the flow front is reaching the sensor, a first small pressure increase occurs. When the finger slows down, the pressure stays constant, until the average flow front reaches the sensor position. Then the pressure is increasing again. This effect can also be observed for the VE-SMC (cf. Figure 3-5) at Sensor 4, when a pressure is recorded for the first time at 2.5 s. The threshold of approx. 3.0 bar is the pressure of the small finger, while the normal pressure increase due to the rheological pressure starts at approx. 2.2 s. For the UPPH glass fiber SMC, this effect is much higher and overlaid by other effects (cf. Section 3.7). Therefore, the determination of the exact time at which the flow front reaches the sensor has a high inaccuracy. Since only the experimental series for the deformation rate of $D = 0.25 \text{ s}^{-1}$ has enough

repetitions to average the inaccuracies, the relative volume change is only plotted for this setting (see Figure 3-11). In the same plot, the relative volume change of the UPPH carbon fiber SMC is given. Based on this experimental data, the UPPH SMC formulations have to be considered as compressible.

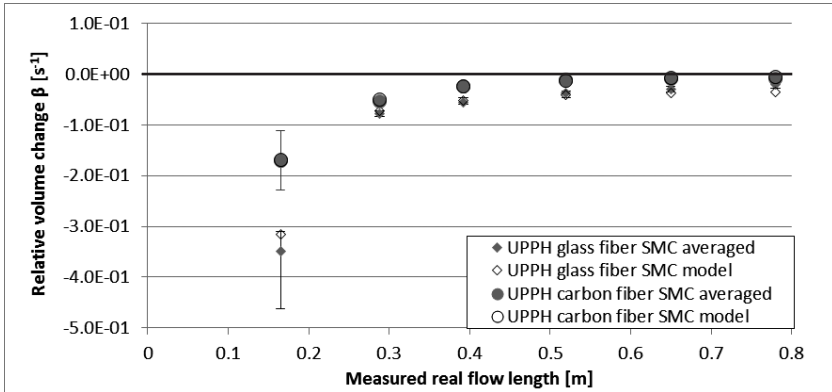


Figure 3-11: Relative volume change β from the experiments of the glass and carbon UPPH SMC for a nominal deformation rate of $D = 0.25 \text{ s}^{-1}$

3.4. Compressible Rheological 2D Shell-Model [Hoh17a]

After modelling the compressibility, a compressible rheological shell model is developed to take into account the new insights from Section 3.3. The basic rheology model used in this Section was developed by Dumont et al. [Dum03], [Dum07], [Org12] and will be modified to fulfill the compressibility condition. For incompressible SMC formulations, the same model can be used by using a constant relative volume change $\beta = 0$.

From previous studies, Dumont et al [Dum07] made the following assumptions for a plug flow model:

- SMC is a one-phase continuum medium. This means, that the paste (resin and filler) and the fibers have the same velocity and no fiber-matrix separation will occur
- The temperature in the material is practically isothermal [Bar79], except in the thin resin layer near the mold
- There will be no curing during the compression molding. As shown previously, the filling time is less than 15 s and together with the isothermal assumption, the reaction does not start during mold filling [Abr00]
- No external or acceleration forces will be considered, as they are very small relative to the viscous forces due to the deformation. Therefore the stress tensor is defined as

$$\boldsymbol{\sigma} = -p\boldsymbol{\delta} + \boldsymbol{\sigma}_V(\mathbf{D}), \quad (24)$$

where p is the hydrostatic pressure, $\boldsymbol{\sigma}_V$ the viscous stress tensor and \mathbf{D} the deformation rate tensor. Therefore, the first momentum balance equation is defined as

$$\text{div}(\boldsymbol{\sigma}) = \vec{0} \quad (25)$$

- Based on Section 3.3 the volumetric change is assumed spatially constant and isotropic [Gui12]

By using the coordinate system introduced in Figure 3-1 and using the middle plane of the current plate height as $x_3 = 0$ and the x_3 boundary conditions at the mold walls, Dumont et al. [Dum07] derived the following formulation for the strain rate :

$$\mathbf{D} = \begin{pmatrix} v_{1,1} & \frac{1}{2}(v_{1,2} + v_{2,1}) & 0 \\ \frac{1}{2}(v_{1,2} + v_{2,1}) & v_{2,2} & 0 \\ 0 & 0 & \frac{\dot{h}}{h} \end{pmatrix}, \quad (26)$$

where v_{ij} is defined as:

$$v_{i,j} = \frac{\partial v_i}{\partial x_j}. \quad (27)$$

As shown in the previous Section, the material is considered as compressible. This leads to the following mass balance equation:

$$\operatorname{div}(\vec{v}) = -\frac{\dot{\rho}}{\rho} = \dot{\epsilon}_v(t) = \beta(t), \quad (28)$$

with the velocity field \vec{v} , the density ρ , its change $\dot{\rho}$ and the volumetric strain rate $\dot{\epsilon}_v$.

Due to the plug-flow behavior, the 3D problem can be reduced to a 2D shell description in the e_1 - e_2 -plane. Due to the fact that the shear components $\mathbf{D}_{\gamma 3}$ ($\gamma \in \{1,2\}$) of the strain rate tensor are constrained to zero, arbitrary reaction terms ($T_{\gamma 3}$) must be added [Dum07]. Therefore, the stress tensor $\boldsymbol{\sigma}$ from eq. 24 can be rewritten as:

$$\boldsymbol{\sigma} = -p \boldsymbol{\delta} + T_{\gamma 3} (\vec{e}_\gamma \otimes \vec{e}_3 + \vec{e}_3 \otimes \vec{e}_\gamma) + \boldsymbol{\sigma}_V, \quad \gamma \in \{1,2\}. \quad (29)$$

To gain the momentum balance equation (eq. (25)) for the shell-approach, the equation is integrated over the thickness h of the SMC [Dum07]. Therefore, it can be written as:

$$-\overline{\operatorname{grad}} P + \frac{1}{h} (\vec{T}^+ + \vec{T}^-) + \operatorname{div} \overline{\boldsymbol{\Sigma}}^V = \vec{0}, \quad (30)$$

where the symbol “ $\overline{}$ ” indicates the 2D unknown field in e_1 - e_2 -direction of the 3D tensor, with the thickness averaged pressure P and the thickness averaged in-plane viscous stress $\overline{\boldsymbol{\Sigma}}^V$, defined as:

$$P = \frac{1}{h} \int_{-h/2}^{h/2} p \, dx_3, \quad (31)$$

$$\overline{\boldsymbol{\Sigma}}^V = \frac{1}{h} \int_{-h/2}^{h/2} \boldsymbol{\sigma}^V \, dx_3, \quad (32)$$

and the tangential stress vectors \vec{T}^+ and \vec{T}^- between the SMC and the upper ($x_3 = h/2$) and the lower ($x_3 = -h/2$) part of the mold, respectively:

$$\left(\vec{T}^+ + \vec{T}^-\right) \cdot \vec{e}_\gamma = [T_{\gamma 3}]_{-h/2}^{h/2}, \quad \gamma \in \{1,2\}. \quad (33)$$

By using the assumption that no external or acceleration forces will be considered (eq. (25)), and that the deformation rate is constant in the material at one point of time, which leads to

$$\frac{d\bar{\Sigma}^V}{dx_i} = 0, \quad (34)$$

the thickness averaged mass balance equation (eq. (30)) results in:

$$\begin{cases} -\frac{dP}{dx_1} + \frac{1}{h} \frac{d(\bar{T}^+ + \bar{T}^-)}{dx_1} = 0 \\ -\frac{dP}{dx_2} = 0 \end{cases}, \quad (35)$$

for the rheological tool flow. By using the power-law viscosity model proposed by Dumont et al. [Dum03] and the power-law friction stress model of Abrams and Castro [Abr03] modified to the 2D approach by Dumont et al. [Dum07], the averaged pressure $P(x_1)$ can be solved by integrating these equations along with the boundary condition at the flow front. The boundary condition for this integration differs from the incompressible one, since the compressible flow front (x_1) is defined by equation (21), where $l_{sx} = x_1$:

$$x_1(t) = \frac{l_o h_o}{h(t)} (\Delta t \beta(t) + 1). \quad (36)$$

This leads to the following equation for the thickness-averaged pressure with an initial charge sample at the left side:

$$P(x_1(t)) = -\eta_{ps} \left(\frac{1}{1+H} \right) \frac{1}{D_0^{n-1}} \left| \frac{\dot{h}}{h} \right|^{n-1} \frac{\dot{h}}{h} + \left(\frac{2\lambda}{m+1} \right) \frac{\dot{h}}{v_0^{m-1} h^2} \left| \frac{\dot{h}}{h} \right| \left[x_1^{m+1} - \left(\frac{l_0 h_0}{h(t)} (\Delta t \beta(t) + 1) \right)^{m+1} \right], \quad (37)$$

where η_{ps} is the corresponding extensional viscosity (compare Barnes [Bar00]) under a plane strain rate of $D_0 = 1.0 \text{ s}^{-1}$, H is a rheological function (compare Dumont et al. [Dum07]), n and m are the power-law exponents for the viscosity of the SMC and for the rheology of the boundary layer, respectively, and λ is the hydrodynamic friction coefficient.

Using the global form of the momentum balance equation, averaging it over the volume and inserting eq. (37) (compare Dumont et al. [Dum07]), leads to the following equation for the volumetric averaged axial stress $\langle \sigma_{33} \rangle$:

$$\langle \sigma_{33} \rangle = \eta_{ps} \frac{1}{D_0^{n-1}} \left| \frac{\dot{h}}{h} \right|^{n-1} \frac{\dot{h}}{h} + \left(\frac{2\lambda}{m+2} \right) \frac{\dot{h}}{h^{m+1}} \left(\left| \frac{\dot{h}}{v_0} \right| \right)^{m-1} \left(\frac{l_0 h_0}{h(t)} (\Delta t \beta(t) + 1) \right)^{m+1}. \quad (38)$$

By using eq. (30), the local thickness averaged axial stress Σ_{33} at the mold surface ($x_3 = \pm h/2$) can be determined by

$$\Sigma_{33}(x_1) = \eta_{ps} \frac{1}{D_0^{n-1}} \left| \frac{\dot{h}}{h} \right|^{n-1} \frac{\dot{h}}{h} - \left(\frac{2\lambda}{m+1} \right) \frac{\dot{h}}{h^{m+1}} \left(\left| \frac{\dot{h}}{v_0} \right| \right)^{m-1} \left[x_1^{m+1} - \left(\frac{l_0 h_0}{h(t)} (\Delta t \beta(t) + 1) \right)^{m+1} \right]. \quad (39)$$

These equations can be seen as the sum of the bulk rheology stress (first term) and the friction stress (second term).

3.5. Material Characterization with the Compressible Rheological Model

To determine the rheological parameters of the core region and the friction parameters of the lubrication layer, a two-step approach is used.

First, the hydrodynamic friction coefficient λ and the corresponding power law coefficient m are identified using the pressure difference between two sensors at a constant closing speed. By using equation (39) at the mold surface ($x_3 = \pm h/2$), this pressure difference can be expressed as:

$$\sigma_{33}(x_{II}) - \sigma_{33}(x_I) = -\frac{2\lambda}{m+1} \left(\frac{|\dot{h}|}{v_0} \right)^{m-1} \frac{\dot{h}}{h^{m+1}} [x_{II}^{m+1} - x_I^{m+1}]. \quad (40)$$

In the second step, the viscosity power-law coefficient n is fitted to the experimental pressure results at different nominal deformation rates using equation (39). To gain a representable strain-rate range, the results for the constant nominal deformation rates and the constant closing speed have to be used [Hoh17a]. Based on this coefficient, the reference extensional viscosity η_{ps} can be determined.

In the following Section, this procedure is applied to the test series of the different SMC formulations. Furthermore, the resulting material parameters are presented. The comparison of all material parameters are given and discussed in Section 3.6.

3.5.1. Class-A SMC formulations

For the Class-A SMC formulations, molding trials only with a constant closing speed were performed. Since the hydrodynamic friction coefficient characterization depends on the closing speed (cf. Section 3.5) and not on the deformation rate, the variation over the process range is relatively low. The experiments with a constant deformation rate would have led to a higher variation within the molding series. Based on the available data, a friction power-

law coefficient of $m = 0.6$ is determined for both materials. The hydrodynamic friction coefficient exhibits a small variation between the formulations. The normal Class-A SMC has a hydrodynamic friction coefficient of $\lambda_{\text{Class-A}} = 1.8 \text{ MNs m}^{-3}$, while the LD Class-A SMC has a slightly higher hydrodynamic friction coefficient of $\lambda_{\text{LD Class-A}} = 2.0 \text{ MNs m}^{-3}$.

For the LD Class-A SMC, additionally experiments were performed with paste without fibers. By using the same method, a friction power-law coefficient of $m = 0.6$ and a reduced hydrodynamic friction coefficient of $\lambda_{\text{LD Class-A, paste}} = 0.85 \text{ MNs m}^{-3}$ are determined.

After the determination of the friction parameters of the lubrication layer, the reference extensional viscosity is calculated. In a first step, the rheological stress σ_{V33} is plotted over the deformation rate D to determine the rheological power-law exponent n . Therefore, the reference deformation rate of $D_0 = 1 \text{ s}^{-1}$ is used. This correlation is shown in Figure 3-12. For the Class-A SMCs the exponents are identified with $n_{\text{Class-A SMCs}} = 0.44$. For the LD Class-A SMC, a coefficient of $n_{\text{LD Class-A SMC, paste}} = 0.58$ is evaluated. These two coefficients for the SMC and the paste are the same results as determined by Dumont et al. [Dum03]. [Hoh17b]

Using these rheological power-law coefficients, the reference viscosity for the Class-A formulations can be determined as $\eta_{\text{PS Class-A SMCs}} = 4.10 \text{ MPa s}$ and for the paste as $\eta_{\text{ps LD Class-A SMCs, paste}} = 0.75 \text{ MPa s}$.

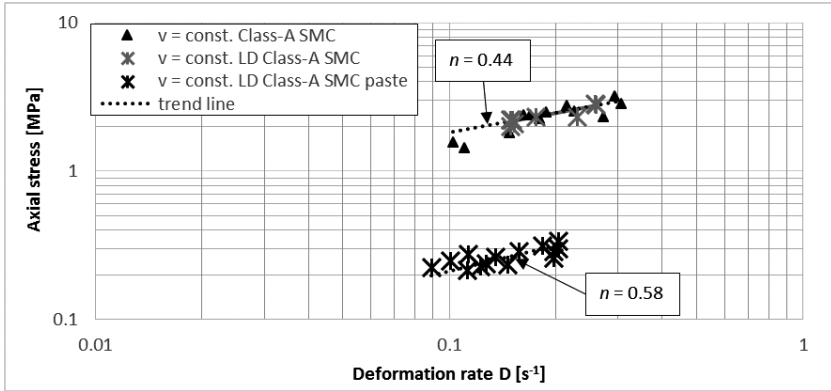


Figure 3-12: Fitting of the viscosity power-law exponent n with the results for the constant closing speed ($\dot{h} = 1 \text{ mm s}^{-1}$) of the Class-A, LD Class-A SMC and the LD Class-A SMC paste

3.5.2. Vinylester SMC formulation

For the VE-SMC characterization, a high number of experiments are available, covering a large range of process settings. Therefore, the material data could be determined over a large closing speed and deformation rate range with many data points (cf. Section 3.2.3).

By using the pressure difference expressed by eq. (40), a friction power-law coefficient of $m = 0.6$ and an averaged hydrodynamic friction coefficient of $\lambda_{\text{VE-SMC}} = 2.3 \text{ MNs m}^{-3}$ is determined. These values are close to those presented by Dumont et al. [Dum07].

After determining the friction coefficients, the viscosity and the viscosity power-law coefficient can be computed. These fitted results, together with the trend line, are plotted in Figure 3-13. By using the reference deformation rate of $D_0 = 1.0 \text{ s}^{-1}$ in eq. (38), the best viscosity power-law exponent is $n_{\text{VE-SMC}} = 0.27$, with a small variation over the different experiments. This value corresponds to the ones presented by Lee et al. [Lee81]. [Hoh17a]

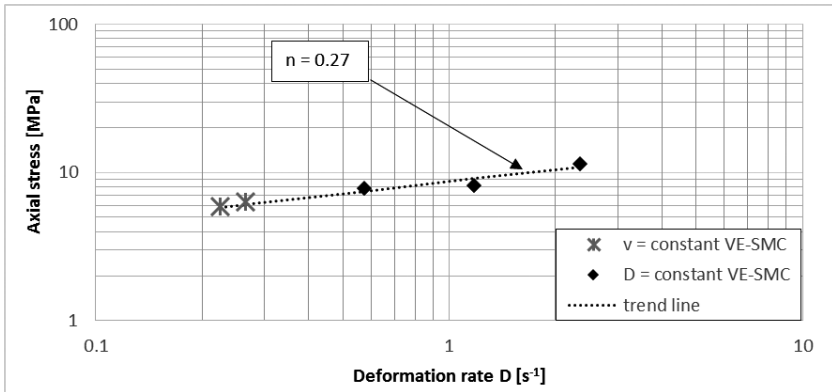


Figure 3-13: Fitting of the viscosity power-law exponent n with the results for the constant nominal deformation rates ($D = 0.5 \text{ s}^{-1}$, 1.0 s^{-1} and 2.0 s^{-1}) and the constant closing speed ($\dot{h} = 1 \text{ mm s}^{-1}$) of the VE-SMC formulation [Hoh17a]

3.5.3. UPPH SMC formulations [Hoh17b]

Due to the pressure distribution with the pressure peaks at the flow front of the UPPH glass fiber SMC, compared to the UPPH carbon fiber SMC (cf. Section 3.2.4 and 3.2.5), the characterization of the rheological parameters is only possible for the carbon fiber SMC. The presented compressible rheological model (cf. 3.4) cannot describe material property changes during the flow, which must be the reason for the pressure peaks at the flow front. To give a first description of these material property changes, a general modelling approach for the glass fiber SMC is presented in Section 3.7.

During the evaluation of the hydrodynamic friction coefficient for the UPPH carbon fiber SMC, it becomes apparent, that it is not possible to determine a constant value for the velocity controlled nor for the deformation-rate-controlled experiments. Comparing the three diagrams for three different time steps during the molding process in Figure 3-14, it can be recognized, that the coefficient has two thresholds. One is in the area of the initial charge (flow front smaller than 0.16 m) and the other one is in the flow area. This becomes

even clearer when taking the small leakage and therefore the pressure decrease of Sensor 1 into account. When the flow front reaches Sensors 4 and 5, the pressure at Sensor 1 is underestimated and therefore also the pressure difference. This causes the decrease of the hydrodynamic friction coefficient λ at $x = 0.035$ m.

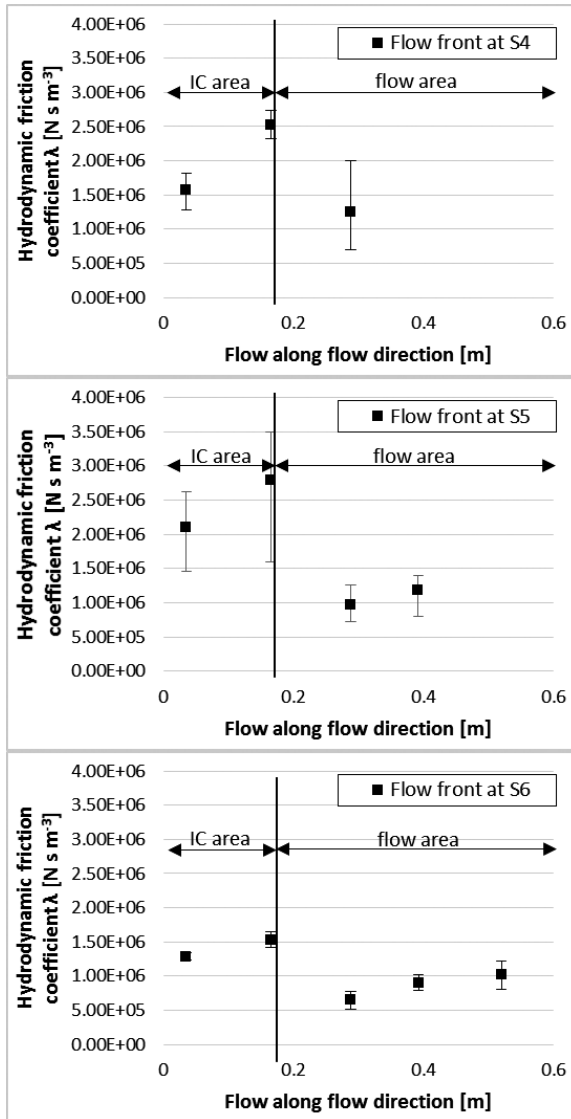


Figure 3-14: Progression of the hydrodynamic friction coefficient λ over time and location for the UPPH carbon fiber SMC and a constant closing speed of $\dot{h} = 1 \text{ mm s}^{-1}$ [Hoh17b]

The reason for these two different hydrodynamic friction coefficients cannot be related to the temperature nor to the thickness of the lubrication layer, as this would lead to a smaller value in the area of the initial charge. Since this effect does not appear for the glass fiber reinforced materials, it could be caused by the interaction of the carbon fibers with themselves or with the resin.

By plotting the axial rheological stress over the deformation rate, a best viscosity power-law exponent of $n_{UPPH\ C-SMC} = 0.27$ could be fitted (see Figure 3-15).

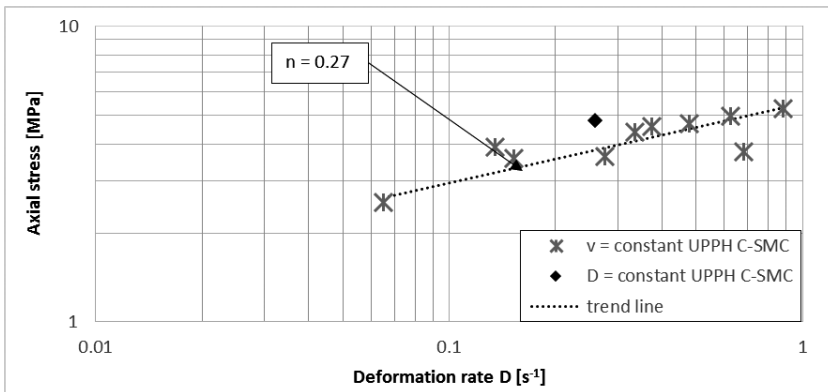


Figure 3-15: Fitting of the viscosity power-law exponent n with the results for the constant nominal deformation rates ($D = 0.25\text{ s}^{-1}$) and the constant closing speed ($\dot{h} = 1\text{ mm s}^{-1}$) of the UPPH C-SMC formulation

As detected for the friction characterization, the UPPH carbon fiber SMC shows a variation also for the extensional viscosity in the initial charge and the flow area. The averaged value for the extensional viscosity in the IC area is determined to $\eta_{ps\ IC} = 3.65\text{ MPa s}$, while it is $\eta_{ps\ flow} = 2.75\text{ MPa s}$ in the flow area. Again, this could not be ascribed to temperature distribution, lubrication layer thickness or other process parameters. Considering both variations for the friction and viscosity stresses, the anisotropy of the viscosity due to

fiber orientations and fiber volume changes could be an explanation. Both effects were numerically investigated by Tsigkopoulos et al. [Tsi09] and Bertóti et al. [Ber17]. They developed numerical anisotropic viscosity approaches, which describe the viscosity as a function of the fiber orientation. This correlates to the experimental observation that the difference between the initial charge area and the flow area depends on the closing speed (see Figure 3-16). The change of the closing speed leads to a different deformation gradient and therefore to different fiber orientation distributions. The reason why this effect only appears for the carbon fiber reinforced SMC might be the fiber bundle structure. For glass fibers, the bundles stay in a more or less round shape, while for carbon fibers, the bundles spread open to a flake-like structure (see Figure 3-17). This effect is intensified by the different bundle sizes, since the UPPH carbon fiber SMC is manufactured with 50k rovings, while 12k rovings are used for the UPPH glass fiber SMC. Therefore, other fiber interactions and fiber reorientation mechanisms take place. Another possible explanation for this behavior could be based on the different thickening mechanisms of Class-A respectively VE SMC compared to the UPPH SMC. The first two are thickened by an alkaline earth metal oxide (magnesium oxide). This thickening mechanism is investigated since 1970 [Van70] but still not understood satisfyingly [Kec16]. The UPPH SMC is thickened with isocyanate. Hereby, the hydroxyl and carboxyl groups of the UP form covalent bonds with the isocyanate and consequently increase the extensional viscosity of the paste [Sai96]. As the used isocyanate shows a reactivity of 2.7, a weak three-dimensional network will be the result of the cross-linking during maturation. Compression molding of the SMC should cause a partially break of this network at a certain strain. This would consequently lower the extensional viscosity of the SMC during molding.

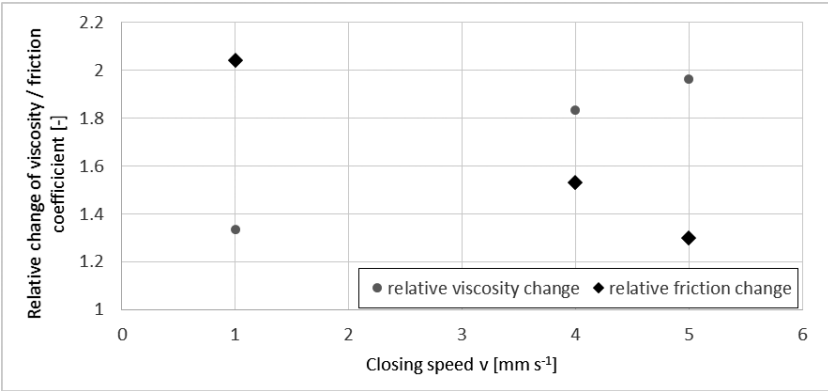


Figure 3-16: Relative change of the extensional viscosity and hydrodynamic friction between the initial charge area and the flow area of the UPPH carbon fiber SMC [Hoh17b]

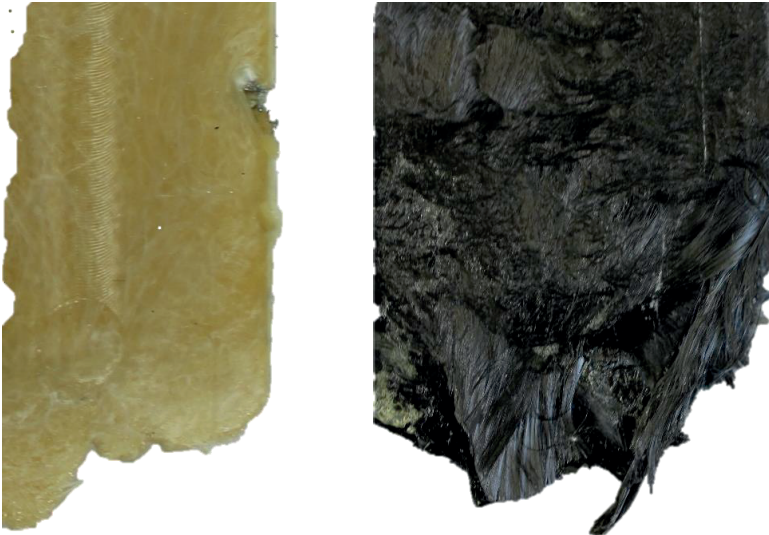


Figure 3-17: Comparison of the fiber bundle structure in the glass fiber reinforced VE SMC (left) and the UPPH carbon fiber SMC (right)

3.6. Effects of the material type on the rheological behavior and model parameters

Based on the variations in the SMC material composition, effects like compressibility and variations in the initial charge area and the flow area are observed. The Class-A SMC with fillers and a relatively low glass fiber volume content showed the typical rheological characteristic with similar material parameters to those presented by Dumont et al. [Dum03]. By increasing the fiber volume content and omitting the fillers, a substantial compressibility could be observed. The change from glass to carbon fibers leads to material behavior, which shows the same compressibility, but a significant change between the initial charge area and the flow area. This could be related to the structure and shape of the fiber bundles or of the matrix or both. While showing their specific differences in rheological behavior, all SMC formulations, except for the UPPH glass fiber SMC, can be modeled with the same basic model presented by Dumont et al [Dum03], [Gui12], [Fer17]. Within this model, only small modifications regarding compressibility and local dependencies (IC and flow region) of the viscosity and friction parameters due to local variation of fiber orientations according Section 3.4 and 3.5 are necessary.

Taking these information and characterization results into account, it is possible to choose a suitable modelling and characterization approach for a specific SMC. This helps to simplify the characterization procedure and to set the results into the correct context.

Furthermore, the power law coefficient for the friction term m can be assumed to be constant, independent of the material composition. The extensional viscosity coefficient n can be considered as constant depending on the SMC type. For SMC formulations with a high filler content it is 0.44, while the pure resin mixture of such an SMC has a coefficient of 0.58. By omitting the fillers for semi-structural SMC formulations, a coefficient of 0.27 can be used. Based on this, only the extensional viscosity η and the hydrodynamic friction coefficient needs to be determined for new SMC formulations.

Table 3-6: Comparison of rheological material data for a closing speed of $\dot{h} = 1 \text{ mm s}^{-1}$ (comp. [Hoh17b])

	Extensional viscosity η_{PS} at $D = 1 \text{ s}^{-1}$	n	Hydrodynamic friction coefficient λ at $\dot{h} = 1 \text{ mm s}^{-1}$	m
Class-A	4.10 MPa s	0.44	1.80 MN s m ⁻³	0.6
LD Class-A	4.10 MPa s	0.44	2.00 MN s m ⁻³	0.6
LD Class-A resin	0.75 MPa s	0.58	0.85 MN s m ⁻³	0.6
VE SMC	12.00 MPa s	0.27	0.80 MN s m ⁻³	0.6
UPPH SMC	3.65 MPa s (IC area)	0.27	1.23 MN s m ⁻³ (IC area)	0.6
	2.75 MPa s (flow area)		0.60 MN s m ⁻³ (flow area)	

3.7. Alternative flow kinetic of the UPPH glass fiber SMC [Hoh17c]

In Section 3.2.4, 3.3.3 and 3.5.3 the different behavior of the UPPH carbon fiber SMC, compared to the other SMC formulations, are discussed. To identify the reasons for this behavior, an experimental investigation based on optical and micro tomography scans were done. Based on these results, an alternative flow description is presented.

3.7.1. Experimental investigation

Optical and pressure based analyses

To identify the reason for the pressure peaks at the flow front of the UPPH glass fiber SMC, a series of short shots was conducted with two repetitions

for every step. During the first evaluation of these plates, three different areas are observed by optical assessment. At the flow front and at the opposite end of the plate (where the initial charge was placed), areas with a randomized oriented fiber distribution and complex curvature of the fibers at the surface are observed (Figure 3-18). In the center area between the other two areas, a quasi-isotropic fiber orientation with mainly straight fibers is observed at the surface.

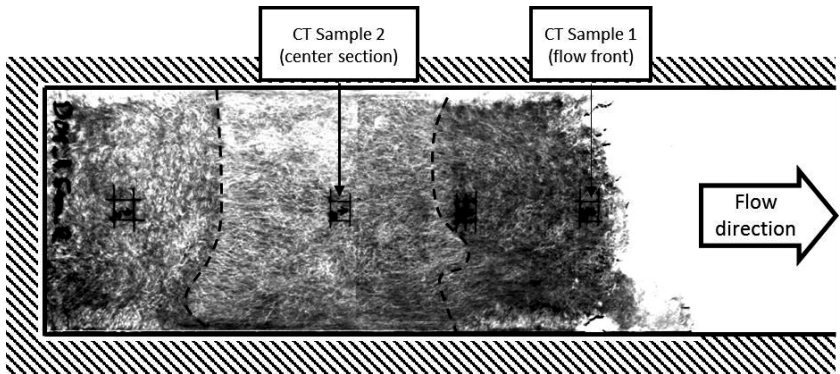


Figure 3-18: Gray-scale picture with high contrast of a UPPH glass fiber SMC short shot and CT Sample positions

To identify which of three regions is responsible for the pressure peaks, the local lengths of the peak are evaluated. Therefore, the point with the first significant pressure decreases after the pressure peak is used. By using the press data with the current gap height, the position of the current flow front is calculated [Hoh17a]. Using this flow length information and the position of the sensor with the pressure peak, the length of the primary responsible area could be calculated. Furthermore, the plates were gauged by using visual criteria according to Figure 3-18. Therefore, the three areas were measured. The results from the pressure evaluation and the length of the swirled flow front region (vortex area) are plotted in Figure 3-19 for both plates (repetitions) of the short-shots study with 4.5mm thickness. The optical method leads to only

one measuring point, but with the pressure evaluation method, a tracking of the flow front region could be done. As the correlation between the optical and the pressure evaluation seem to correspond, the flow front region with its highly swirled fiber orientation at the surface seems to be responsible for the pressure peak.

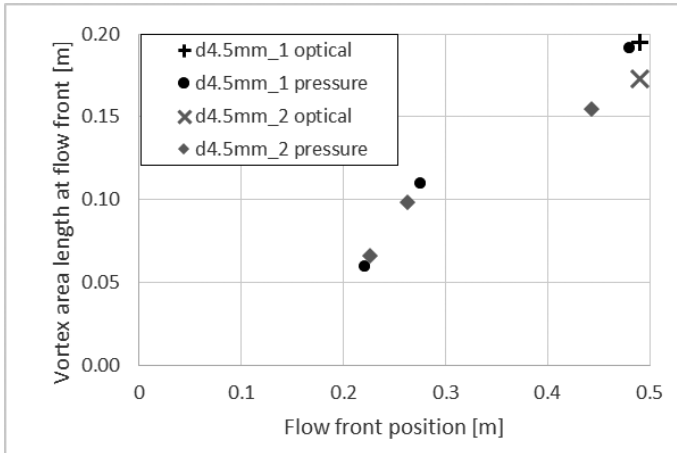


Figure 3-19: Length of the vortex area at the flow front: optical measured and extracted from pressure distribution

Micro tomography scans

To understand what is happening during the flow phase and why the three regions develop, a series of micro tomography scans were conducted by the Institute for Applied Materials (IAM-WK) at the Karlsruhe Institute of Technology (KIT). Therefore, four samples of 20 mm x 20 mm, two from the flow front region and one each from the center and initial charge region were excised from each 4.5 mm thick plate. The positions of these samples are indicated in Figure 3-18.

Comparing the scans from the flow front (Figure 3-20) and the middle region (Figure 3-21), the visual differences between these two regions can be confirmed. The flow front sample shows fibers, which are highly swirled. Furthermore, the original fiber bundles have been separated into smaller bundles or even single fibers at the flow front. In contrast to these vortex regions, the center region shows the typical fiber orientation originating from the manufacturing process. Especially in the cross-section, the randomly orientated fiber bundles can be recognized. At the surface, some separation and reorientation effect of the fiber bundles appeared.

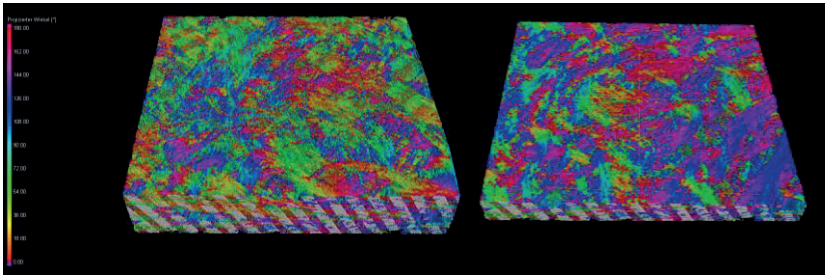


Figure 3-20: Micro tomography scan with color-coding of the fiber orientation direction of the flow front (sample 1): view on top of the sample (left) and sliced in the middle (right).

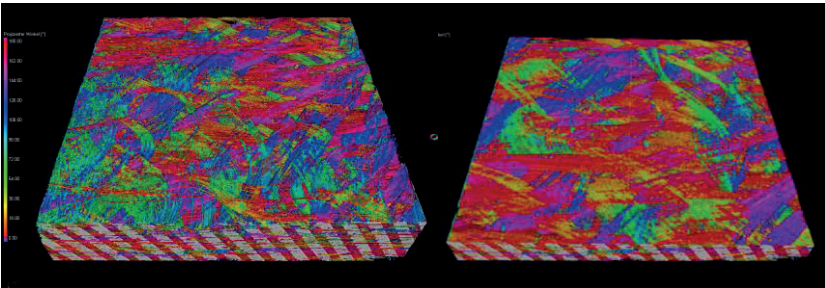


Figure 3-21: Micro tomography scan with color-coding of the fiber orientation direction of the sample from the center region (sample 2): view on top of the sample (left) and sliced in the middle (right).

3.7.2. Model Discussion

The typical flow model, which is also used for the rheological characterization of the carbon fiber SMC [Hoh17a], divides the material in two regions in thickness direction. Since the SMC initial charge is placed room-tempered into the hot mold, the outer layer of the material is heating up rapidly. Owing to the relatively low thermal conductivity, this layer has a varying thickness, in the area of only a few micrometer like shown by Shokrieh and Mosalmani [Sho14]. This layer contains no fibers and, because of the high temperature, the viscosity decreases dramatically and the layer functions as a lubrication layer. The charge core region stays relatively cold during the molding process. Due to these two different regions, the lubrication layer is exposed to a high shear rate, while the core charge is loaded by normal forces. Since SMC is a compressible, like shown in Section 3.3, and a Non-Newtonian fluid [Kot98], [Gib99], the shear and the extensional viscosity are not coupled by the Trouton ratio [Tro1906] and have to be determined separately.

The extensional-based deformation of the core region leads to a material flow, where the core charge stays in the middle of the plate thickness and no mixing in the thickness direction occurs. Therefore, the measured pressure can be divided into a rheological stress (from the core charge region) and the hydrodynamic friction stress (from the lubrication layer) (cf. eq. (1)).

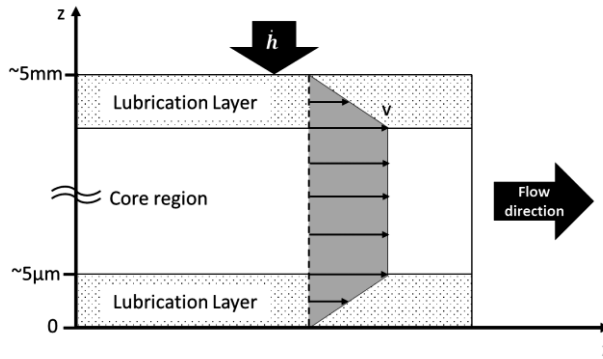


Figure 3-22: Schematically cross-Section of SMC material during the molding process

In contrast to this typical behavior of the carbon fiber SMC, the glass fiber SMC must have a different flow behavior to explain the pressure distribution. To identify this flow behavior, the evolutions of the three regions (vortex region adjacent to the mold walls and aligned region in the core region) over the molding process is analyzed using the short-shot study. Taking into account the micro tomography scans it seems that the core charge is moving in flow direction. Therefore, the lubrication layer or more precise in this case, the complete sheet at the mold surface is flowing into the vortex regions (see Figure 3-23). Furthermore, the core charge region is mainly transported in flow direction, while showing low elongation. In such a system, the main flow of the material would be at the mold surfaces, where the higher temperature leads to a lower viscosity.

The reason for the pressure peak could not be identified yet. It can be excluded, that the material is speeding up so much, that the hydrodynamic pressure becomes relevant. With a flow front speed of $v = 0.1 \text{ m s}^{-1}$ after 4 s of the molding process and a 10 times higher speed in the lubrication layer, this would only lead to an increase of 1.0 bar. It is more realistic, that the fiber-fiber-interaction in the vortex regions leads to an increase of the homogenized shear viscosity and therefore to higher stresses. Furthermore, the fiber

bundle separation and the curved fibers could cause an anisotropic viscosity shown by Bertóti and Böhlke [Ber17] and Tsigkopoulos et al. [Tsi09], which is higher than the isotropic viscosity. New methods to investigate this approach will be designed and conducted in the future within the GRK2078.

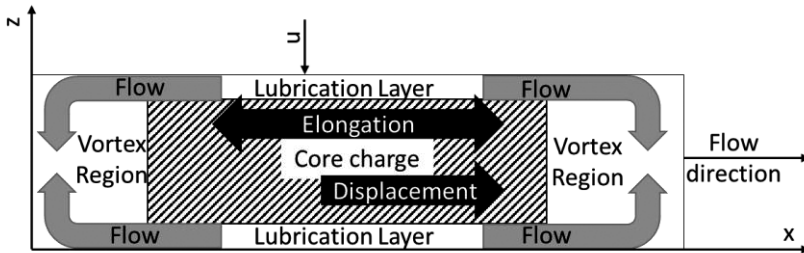


Figure 3-23: Schematically cross-Section of the probable flow of glass fiber UPPH SMC during the molding process

These two different flow behaviors are caused by the fiber type, as the paste is the same for both UPPH SMC materials. Therefore, the thermal conductivity and consequently the temperature distribution seem to be relevant. As the UPPH is still a new resin under research, the material parameters, and the material property effects during the compression molding process have to be investigated further. Furthermore, the ratio of the fiber stiffness to the matrix viscosity might have a significant effect [Pér15]. However, no reason for these two different flow regimes (see Figure 3-22 and Figure 3-23) of the glass and carbon fiber UPPH SMC could be verified so far. The UPPH resin will be further investigated within the International Research Training Group “Integrated engineering of continuous-discontinuous long fiber-reinforced polymer structures” and new results will be available within the next years.

3.8. Summary on rheological measurements

Chapter 3 “Rheological measurements” shows the difference of the flow behavior of different SMC formulations. For this purpose, a rheological in-mold tool was developed. This rheological tool has seven pressure sensors aligned in flow direction. By recording these pressure data and the press data simultaneously, a characterization of the SMC formulations is possible.

Standard Class-A material formulations show a flow regime and a resulting pressure distribution, which could be described by the models developed by Dumont et al. [Dum03], [Dum07], [Gui12]. Using this model, the two Class-A formulations presented in Section 3.2 are characterized.

To capture new application areas for SMC as a semi-structural material, the fiber content of SMC is increased while omitting the fillers. By changing the composition in this manner, it was shown, that these semi-structural SMCs could not be assumed to be incompressible anymore. Therefore, compressibility was added to the previous model by adding the relative volume change as a specific material property. This model was validated by using the semi-structural VE SMC.

To combine the semi-structural SMC with local unidirectional reinforcements, a new unsaturated polyester polyurethane hybrid resin (UPPH) was used for both components, the continuous and the discontinuous fiber reinforced materials. This UPPH resin has a B-stage to fix the preformed shape of the local reinforcements. The B-staging is also effecting the flow behavior of the discontinuous fiber reinforced SMC material. It was shown, that the carbon fiber SMC has different material properties in the initial charge area and the flow area, but could be described by the compressible rheological model. By changing the fiber type from carbon to glass fiber, this UPPH SMC is changing its flow behavior. It was presented, that the flow front has high-pressure peaks, while the remaining areas follow the normal typical pressure pattern. Using these pressure distributions and additional CT scans, a new flow pattern was proposed. This characterization can be used as a basic assumption to

build up an alternative stress model to Dumont et al., which can describe SMC formulations, which do not have a distinctive bulk flow.

4. Process simulation of hybrid SMC

In the first section of this chapter, the current state of the art process simulation is evaluated by using the pressure distributions of the rheological measurements of Chapter 3. Due to the inaccuracy of the obtained pressure predictions of the state of art software, the Coupled-Eulerian-Lagrangian (CEL) approach is used to implement a new SMC-specific material model. Therefore, section 4.2 is focusing on the basic modelling and the implementation of these models. Furthermore, a first consideration of homogeneous local reinforcements in the compression molding process is given. In section 4.3, the validation with the pressure results from section 3.2 is performed, as well as a quantitative validation with the IRTG reference structure.

4.1. Application and Evaluation of state of art commercial compression molding software

To evaluate the state of art commercial compression molding software tools, the characterization pressure distribution of the Class-A SMC (cf. Section 3.2.1) is used. Therefore, the mold is modeled with the exact sensor position within Autodesk® Moldflow® to compare the pressure results at the exact same position. Due to the equation of state formulation in Moldflow, the SMC material is compressed at the beginning of the molding process. To compensate this compressibility, the initial charge height is increased slightly from 8.4 mm to 9.0 mm. The model setup is shown in Figure 4-1.

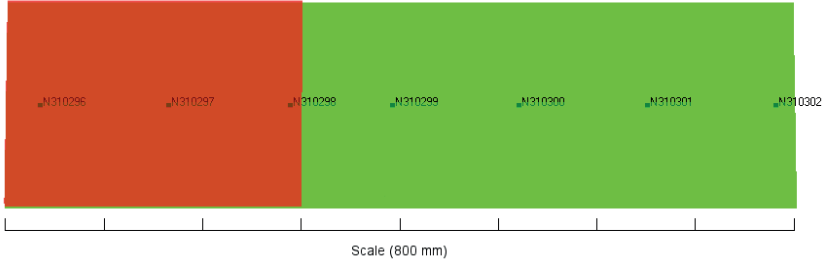


Figure 4-1: Compression molding model with Moldflow, green: final cavity; red: initial charge position; black points: sensor positions

Since Moldflow has its historical origin in the injection molding simulation of thermoplastic materials, the shear- and extensional viscosity are coupled by the Trouton ratio [Tro1906] for incompressible Newtonian fluids by

$$\frac{\eta_{shear}}{\eta_{ext}} = \frac{1}{3} . \quad (41)$$

Therefore, only the shear viscosity is calculated by using the Castro-Macosko [Cas82] reactive viscosity model

$$\eta(\alpha, T, \dot{\gamma}) = \frac{\eta_0(T)}{1 + \left(\frac{\eta_0(T)\dot{\gamma}}{\tau^*}\right)^{n-1}} \left(\frac{\alpha_g}{\alpha_g - \alpha}\right)^{(C_1 + C_2\alpha)}, \text{ with} \quad (42)$$

$$\eta_0(T) = B \exp\left(\frac{T_b}{T}\right), \quad (43)$$

which is an extended Cross Williams-Landel-Ferry (Cross-WLF) model for reactive resins. In these equations, τ^* , B , T_b , C_1 , C_2 and α_g are data-fitted coefficients, α is the current degree of cure in the range between 0 and 1. To fit the material parameters of the reactive viscosity model, the pressure distributions from the Class-A SMC characterization (see Section 3.2.1) are used. Using the best fit over all seven pressure sensors, the pressure distribution shown in Figure 4-2 is predicted by the commercial tool. At the beginning of

the compression molding process, the simulated curves (grey) do not have the characteristic pressure increase, which is followed by the thresholds. During the flow phase, the simulated pressure shows the same pattern as the experimental data, but it is overestimating the pressure towards the end of the compression mold process. Due to this overestimation, the maximum pressure is reached too early and therefore, the pressure decrease due to the reduced closing speed begins at a higher relative gap height.

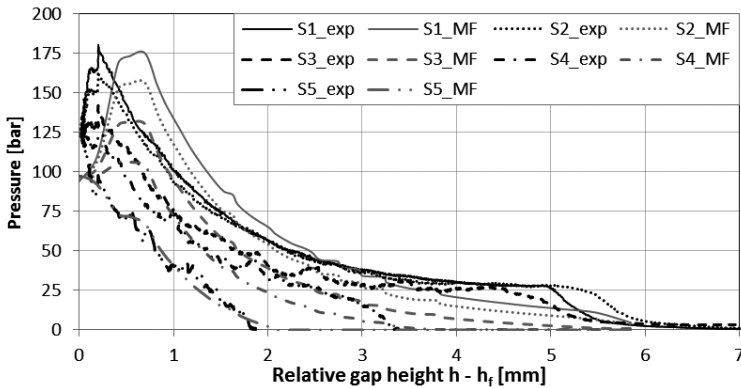


Figure 4-2: Comparison between the pressure distribution from the experiments (black) and the commercial simulation tool based on the fitted reactive viscosity model (grey)

Another important criterion for the comparison is the fiber orientation. In Figure 4-3, the degree of alignment (first eigenvalue) of the fiber orientation tensor \mathbf{A} is plotted for the final plate thickness on the top and bottom surface as well as in a center cutting plane. The fiber orientation of the initial charge is defined as quasi-isotropic, which is a typical assumption for SMC. Therefore, the first and second eigenvalues (equal A_{11} and A_{22}) are set to 0.5. To predict the fiber re-orientation during the molding process, the Folgar-Tucker model with the ARD-RSC extension (cf. Section 2.4) is used. In the fiber orientation plots, which are distributed over the thickness via three Sections, two effects can be observed. The first one is that the fiber orientation on the two surfaces

of the plate is not changing over the flow length. Only near the left tool wall, where the initial charge was placed, a slight decrease of the alignment can be observed. Despite the initially identical fiber orientation, both surfaces show a slightly different fiber orientation. The second effect is that the fiber orientation in the center plane shows a different behavior. Near the short tool side, where the initial charge was placed, the maximal fiber alignment can be observed. In the center, the gradient is opposed to the one at the surfaces. The fiber alignment decreases over the flow length.

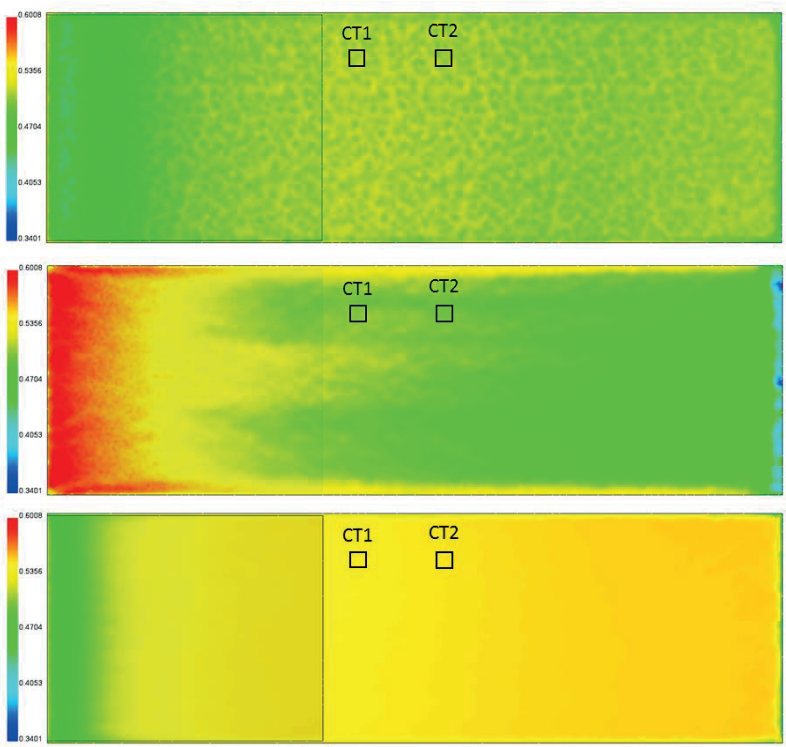


Figure 4-3: Alignment of the fiber orientations predicted by the commercial simulation tool by starting with a quasi-isotropic fiber orientation distribution in the initial charge: top: Top surface view middle: Cutting surface in the middle plane bottom: bottom surface view

To validate the fiber orientation distribution, two CT-scans were made by the Institute for Applied Materials (IAM-WK) [Bry14] to evaluate the distribution through the thickness. Moreover, a series of tensile tests in and perpendicular to the flow direction has been performed in previous work and can be used to evaluate the anisotropy over the flow length.

The two CT-scans were extracted at approximately half the plate's length. The exact position is given in Figure 4-3. To compare the fiber orientation with the predicted ones, the three fiber orientation tensor components A_{11} , A_{22} , A_{12} are compared, since they describe the 2D fiber orientation in the plate plane (see Figure 2-9). These distributions over the thickness are given in Figure 4-4. As the sample size is smaller than the fiber length, a small deviation between the fiber orientations can be accepted, since SMC shows local statistically distributed scatterings. Therefore, the prediction of A_{22} and A_{12} fiber orientation distribution components seems to match, while A_{11} is predicted considerably smaller than measured by CT. Taking into account the form of the fiber orientation tensor and the plate's thickness to fiber length ratio, the sum of A_{11} and A_{22} should be equal to one. Since no fibers could be orientated in thickness direction, the A_{33} component has to be zero. However, it can be observed, that this criterion is not fulfilled for the commercial process simulation tool. It has constant A_{33} component of approximately 0.2, which is could not be detected in reality.

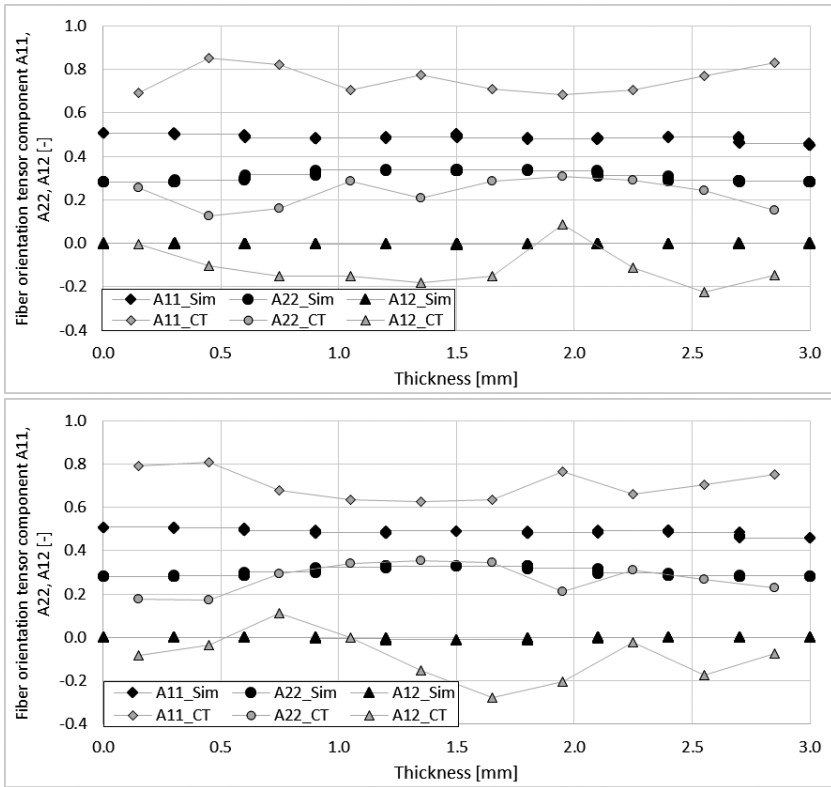


Figure 4-4: Comparison between the fiber orientation distribution from the simulation and CT-scans (from [Bry14]): CT-Position 1 at x = 339 mm, y = 200 mm (top) and CT-Position 2 at x = 431 mm, y = 200 mm (bottom)

To evaluate the anisotropy over the flow length, tensile tests are used, as they are less elaborate than CT measurements. The resulting Young's moduli in both in-plane directions are given in Figure 4-6. This figure clearly shows a uniform anisotropy over the flow length, with some small deviations and slight effects close to the wall at the initial charge position. In contrast, the fiber orientation distribution from the commercial process simulation tool shows an anisotropy change during the molding process along the flow length

(cf. Figure 4-4). This anisotropy change is relatively high where the initial charge was placed, but also present in the flow area, where a smaller fiber reorientation occurs. These orientation effects can be explained by the shear flow domination in the commercial tool. Figure 4-5 shows two cross-sections of the flow front during the compression molding process. The shear rate and the velocity in flow direction are showing the typical thermoplastic fountain flow behavior, which has nothing in common with the SMC typical plug-flow.

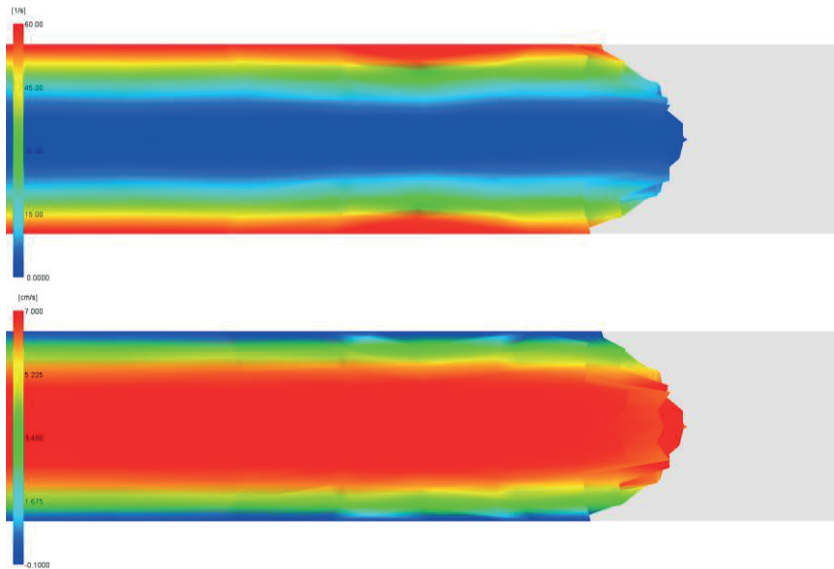


Figure 4-5: Shear rate (top) and velocity in flow direction (bottom) at the flow front during the compression molding simulation with the commercial simulation tool

Considering the fiber reorientation of the combined ARD-RSC Folgar-Tucker model (Section 2.4, eq. (11)), it can be seen that the shear rate is dominating the fiber re-orientation compared to the stretch flow. Therefore, the shear-flow dominated flow in the commercial process simulation tool does not have the capability to predict the correct fiber orientations for the plug-flow dominated SMC flow.

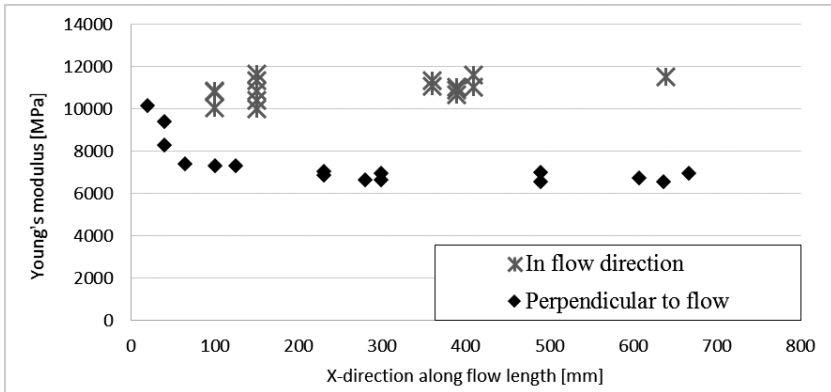


Figure 4-6: Progression of the Young's modulus over the plate length in and perpendicular to the flow direction (data from Mrkonjic et al. [Mrk15])

4.2. Compression molding simulation by using the CEL approach within Abaqus

Due to the inaccuracies in the flow field and in the fiber orientation prediction of the commercial compression molding software, a new method needs to be developed to model the typical SMC plug flow. Therefore, the Coupled-Eulerian-Lagrangian (CEL) method within Abaqus is used, as it can describe a material flow as well as Fluid-Structure-Interactions (cf. section 2.5). The following subsections introduce the modelling approaches and the implementation in the Abaqus subroutine environment. Furthermore, the main process setting effects and the interaction between the SMC material and the reinforcements is discussed.

4.2.1. Development of a deformation-rate based material modelling for SMC

To overcome the disadvantages of the commercial compression molding software, a separate modelling of the core region and the lubrication layer is crucial. The lubrication layer develops due to the temperature gradient between the hot surface and the cold SMC material and is containing no fibers. Due to the relatively low thermal conductivity, this lubrication layer is only a few micrometers thick, depending on the exact process conditions [Lee87], [Sho14] (see Figure 3-22). Due to the relatively low viscosity in this lubrication layer compared with the viscosity in the core region, a high velocity gradient occurs and therefore a high shear deformation. Due to this effect, the core region shows a plug flow behavior, since no velocity gradient over the thickness occurs. These two flow behaviors cannot be described with the same material model and require separate formulations. Consequently, the stress in an element that comprises both regions can be expressed as

$$\boldsymbol{\sigma} = -p\mathbf{I} + \boldsymbol{\Sigma}_{fric} + \boldsymbol{\sigma}_{rheo} \quad , \quad (44)$$

where p represents the pressure due to compression, $\boldsymbol{\Sigma}_{fric}$ the friction stress in the lubrication layer and $\boldsymbol{\sigma}_{rheo}$ the rheological stress in the core region. The modelling of these stresses is described in the following Subsections.

Core region

As shown in Section 3.3 and 3.8, the SMC material is a compressible Non-Newtonian fluid. Therefore, the Trouton ratio (see eq. (41)) between the shear and extensional viscosity is not valid. Due to this fact, the shear η_{shear} and extensional viscosity η_{ext} need to be calculated separately. For the extensional viscosity, the same basic formulation is used as in the rheological characterization modelling, and previous experiments show a good correlation (cf. Section 3.4):

$$\eta_{ext}(\mathbf{D}) = \eta_{ps} \left(\frac{\|\mathbf{D}\|}{D_0} \right)^{n-1}, \quad (45)$$

where η_{ps} represents the plain strain extensional viscosity (comp. Section 2.2 and 3.4). This equation needs to be extended to consider the temperature dependencies. Le Core et al. [Le O2] have examined the temperature dependence for the SMC paste for the extensional viscosity and achieved a good agreement with an Arrhenius equation. Therefore, the extensional power law function is extended with an Arrhenius function, so it can be written as

$$\eta_{ext}(\mathbf{D}, T) = \eta_{ps} \left(\frac{\|\mathbf{D}\|}{D_0} \right)^{n-1} \exp\left(-b \left(\frac{1}{T_0} - \frac{1}{T} \right)\right). \quad (46)$$

In this equation, T_0 and b are fitted parameters.

The extensional viscosity as well as the shear viscosity show an increase in their amplitude while the stress rate is reduced. This leads to quite large viscosities for infinitesimal low extensional and shear rates, which could lead to unphysical deformations. Therefore, a maximal extensional and shear viscosity is defined by using a minimal extension rate and a minimal shear rate, respectively. This behavior is observed for many materials and therefore, it is considered for example in the Cross-WLF viscosity model. These two minimum rates are considered as material parameters in the material card.

For the shear viscosity, the same model is used as in the commercial compression molding tool (see eq. (42)). In contrast to the commercial process simulation tool, this model is acceptable, since the shear flow and, therefore, the shear viscosity has a minor influence on the total stress compared with the extensional based stresses.

Based on this equation, the rheological stress can be written as:

$$\boldsymbol{\sigma}_{rheo}(\mathbf{D}, T) = \eta_{elong}(\mathbf{D}, T) \text{dev}(\mathbf{D}) + \eta_{shear}(\alpha, T, \dot{\gamma}) \dot{\boldsymbol{\gamma}}, \quad (47)$$

were $\text{dev}(\mathbf{D})$ represents the deviatoric components of the deformation rate tensor \mathbf{D} .

To solve this rheological stress, the deformation rate tensor \mathbf{D} needs to be calculated. Therefore, the deformation gradient \mathbf{F} and the stretch tensor \mathbf{U} are used to do the decomposition of the deformation rate tensor \mathbf{D} . To do so, both tensors are used to calculate the velocity gradient \mathbf{L} , the deformation rate \mathbf{D} and the asymmetric part of the decomposition (spin matrix) \mathbf{W} in the element and the global coordinate system. The main decomposition of the deformation gradient tensor \mathbf{F} is given Figure 4-7. The deformation gradient is defined by deriving the coordinates of the current configuration x_i from the coordinates of the reference configuration x_0 . In the case of the CEL method, the reference configuration (see Figure 2-10) is the configuration at the beginning of the increment. Therefore, the deformation gradient is defined as

$$F_{ij} = \frac{d \chi_i(\vec{X}, t)}{d X_j}, \quad (48)$$

where $\chi_i(\vec{X}, t)$ is the current position of a material point and X_j the position of the considered material point in the undeformed output or the reference configuration. Due to the CEL formulation with the mapping step, this is equal to the configuration at the beginning of the increment.

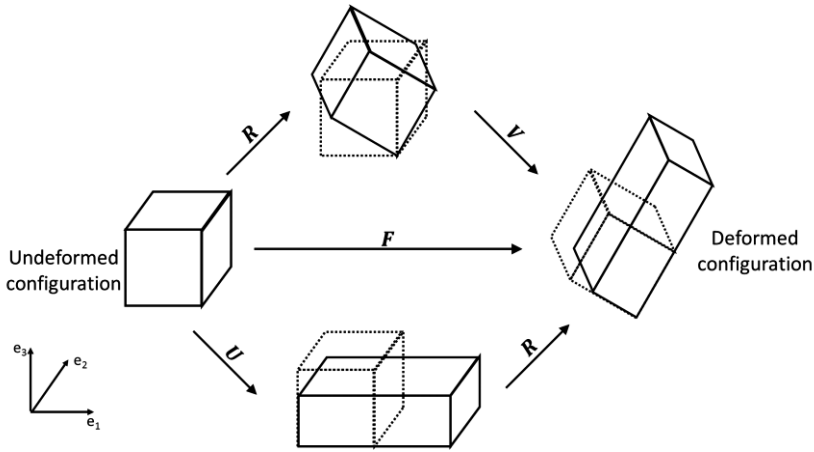


Figure 4-7: Polar decomposition of deformation gradient tensor F

Based on this, the velocity gradient L , the deformation rate in the second intermediate configuration D and the spin matrix W can be calculated by using the intermediate stage of the strain rate tensor $\dot{\epsilon}$, the elastic part of the body rotation matrix R^{el} and the symmetric plastic parts of the velocity gradient \bar{D}^{pl} , as:

$$L = \frac{\partial \bar{v}}{\partial \bar{x}} = \dot{F} F^{-1}. \quad (49)$$

The spin matrix W and the intermediate stage of the strain rate tensor $\dot{\epsilon}$ are the decomposition of the velocity gradient L , defined as $L = \dot{\epsilon} + W$, and can therefore be expressed as:

$$W = \frac{1}{2} \left(\left[\frac{\partial \bar{v}}{\partial \bar{x}} \right] - \left[\frac{\partial \bar{v}}{\partial \bar{x}} \right]^T \right) = \frac{1}{2} (L - L^T), \quad (50)$$

$$\dot{\epsilon} = \frac{1}{2} \left(\left[\frac{\partial \bar{v}}{\partial \bar{x}} \right] + \left[\frac{\partial \bar{v}}{\partial \bar{x}} \right]^T \right) = \frac{1}{2} (L + L^T). \quad (51)$$

By dividing the deformation gradient tensor \mathbf{F} and its composition into an elastic and a plastic part, the following correlations can be used:

$$\mathbf{R}^{el} = \mathbf{F}^{el} \cdot \mathbf{U}^{elT}, \quad (52)$$

$$\overline{\mathbf{D}}^{pl} = \mathbf{R}^{el} \cdot \dot{\boldsymbol{\varepsilon}} \cdot \mathbf{R}^{elT}, \quad (53)$$

$$\mathbf{D} = \mathbf{R}^{el} \cdot \overline{\mathbf{D}}^{pl} \cdot \mathbf{R}^{elT}. \quad (54)$$

Beside this incompressible formulation, a formulation based on the determinant of the deformation gradient tensor is used, which represents the volumetric change of an element. For that purpose, the compressible velocity gradient can be expressed as

$$\mathbf{L}_{iso} = \frac{\dot{L}}{\det(\mathbf{F})^{1/3}}. \quad (55)$$

Based on this equation, the compressible second intermediate configuration of the deformation tensor \mathbf{D} are calculated in the same way. This formulation of the deformation forms the basis to predict the material stresses and the fiber orientation evolution.

Lubrication layer

Due to the high thickness ratio between the lubrication layer and the core region in the order of three magnitudes, the thin layer should not be modeled as a separate phase. This would lead to a discretization which current computation cluster cannot handle. Therefore, the stresses from the lubrication layer Σ_{fric} are modeled as a friction term at the mold surface. For that purpose, the same friction model as for the rheological characterization developed by Abrams [Abr03] (comp. Section 3.4) is used:

$$\Sigma_{fric} = -\lambda \left(\frac{\|\vec{v}\|}{v_0} \right)^{m-1} \frac{\vec{v}}{\|\vec{v}\|} \otimes \frac{\vec{n}}{\|\vec{n}\|}, \quad (56)$$

where λ represents the hydrodynamic friction coefficient, \vec{v} the velocity tensor, m the power-law coefficient for the friction stress and \vec{n} the surface normal of the mold surface, which is perpendicular to the velocity tensor \vec{v} .

Both material formulations are defined as scalar functions. Therefore, the stresses need to be calculated in every element in the local coordinate system defined by the eigenvectors of the deformation rate tensor \mathbf{D} and the velocity field \vec{v} , respectively.

Compression pressure

The pressure due compression p is calculated based on the incompressible hyperelastic specific deformation energy w_0 . The general stress definition based on the three-dimensional continuum consideration is defined as:

$$\boldsymbol{\sigma} = \rho \mathbf{F} \frac{dw_0}{dE} \mathbf{F}^T, \quad (57)$$

with the Green-Lagrangian strain tensor \mathbf{E} . To ensure a hyperelastic incompressible material formulation, the specific deformation energy w_0 is defined as:

$$w_0 = \frac{p}{\rho_0} (\det(\mathbf{F}) - 1). \quad (58)$$

By deriving the specific deformation energy w_0 and using the definition of the bulk modulus K of

$$K = -V \frac{dp}{dV} = \rho \frac{dp}{d\rho}, \quad (59)$$

the compression pressure can be expressed as by using the resulting stress $\boldsymbol{\sigma}$

$$\mathbf{p} = \frac{K}{2} \ln(\det(\mathbf{F})) \mathbf{b}^{-1}, \quad (60)$$

where \mathbf{b} is the Left-Cauchy-Green tensor, which is defined as

$$\mathbf{b} = \mathbf{F} \cdot \mathbf{F}^T. \quad (61)$$

4.2.2. Implementation of the SMC-Material model

The material models are implemented within a user material subroutine (VUMAT), since the usage of a formulation based on a user equation of state (VUEOS) and a user viscosity subroutine (VUVISCOSITY) using the Trouton ratio. As described before, this fixed relation between shear and extensional viscosity needs to be extended for the SMC material formulation and could therefore not be used in this case. Furthermore, not all necessary input parameters for the fiber orientation models are available with a combination of VUEOS and VUVISCOSITY, while they are available within a VUMAT.

To implement the superposition of the three stress terms (cf. eq. (44)) most efficiently, the lubrication layer stress term should be implemented as a mold surface friction term. Since none of the standard friction models implemented in Abaqus Explicit has the correct form, a user subroutine friction model (VUFRICITION) needs to be implemented. Due to the Lagrangian and Eulerian step within the CEL method and their implementation within Abaqus, this subroutine is not supported within CEL. The same applies for the used interaction subroutine (VUINTERACTION). Therefore, all stress terms have to be calculated in the VUMAT subroutine.

The pressure stress and the rheological stress need to be calculated for all filled Euler elements, while the friction stress term is only active, if an SMC filled Eulerian element is in contact with a Lagrangian mold surface element. Within the VUMAT subroutine, this cannot be tested directly with build-in functions or queries. Therefore, the interaction information needs to be passed from other subroutines. As the usage of the VUFRICITION is not possible, no other subroutine can pass this information directly to the VUMAT. To overcome this problem, a series of scripts and subroutines are implemented,

which identify the Eulerian elements that are in interaction by geometrical tests. Therefore, a self-implemented plug-in within Abaqus CAE initializes the geometrical information. This information is stored in individual state variables (SDV) for every Eulerian element. Since the state variables are transported with the fluid, latter are stored as a field variable in a second step, as they are not transported. Due to the definition of the initialization step, it is not possible to define the parameters directly as field variables for the EC3D8R element type in Abaqus CEL. This transfer from the SDV to the FLD is done for every new considered element within the user subroutine to redefine field variables (VUSDFLD). As this leads to a parallel processing of data in different subroutines and writing into the same array in different threads, the user-defined external subroutine VUEXTERNAL is used to secure the thread safety. These non-transported field variables are then used to compare the initialized information with the total motion of the moving mold side in the VUSDFLD. Therefore, the total motion of the moving mold side is passed in by the user defined amplitude subroutine (VUAMP). This information is then passed back to the VUMAT to activate the friction stresses for these Eulerian elements.

A schematic illustration of the order and interactions of scripts (dark blue), subroutines (mint-colored) and internal information (black) is given in Figure 4-8. Detailed information about single scripts and subroutines are given below.

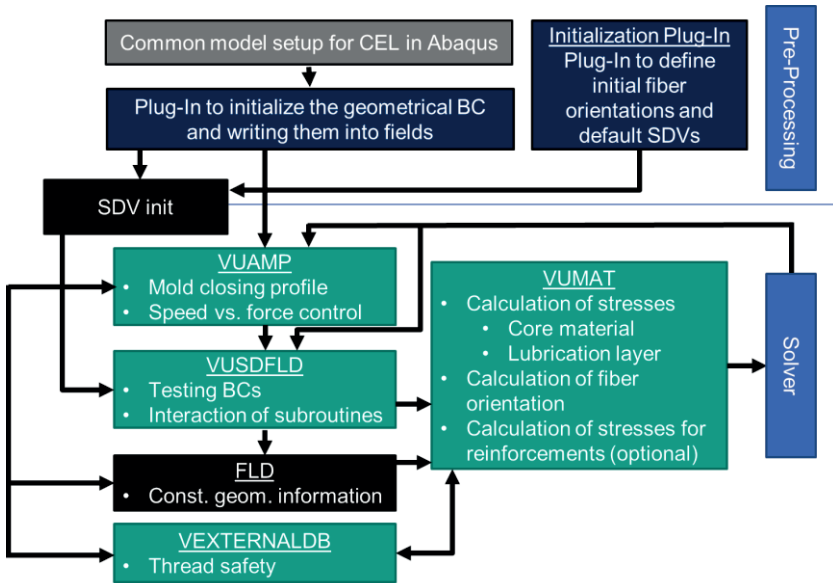


Figure 4-8: Schematic illustration of the order and interaction of scripts (dark blue), subroutines (green) and internal information (black) of the SMC process simulation

Initialization Plug-In

The lubrication layers occur on the moving and on the fixed mold surface. Therefore, different approaches are necessary to detect the Eulerian elements, which are in interaction with the Lagrangian mold elements. Since the Eulerian elements have no relative velocity to the fixed mold surface, always the same elements are in interaction. Therefore, the flag as well as the interaction area between the elements and the normal vector of the fixed mold surface are stored as state variables by the plug-in. For the interaction with the moving mold surface, the distance between the element and the moving mold surface in closing direction is necessary. When the nearest mold surface element in closing direction is detected, the minimum and the maximum distance of this Eulerian element are stored in the state variables as well as the

normal vector of the corresponding element of the moving mold surface. To calculate the interaction area between the mold surface and the Eulerian element in the VUMAT, the coordinates of the eight nodes of the Eulerian element as well as one reference point of the nearest mold surface are stored as state variables. To hand over the necessary input to the plug-in, a drop down menu is integrated in the user interface to choose the part instances for Euler mesh, moving mold and fixed mold (see Figure 4-9). In the next step, the closing direction with the amplitude information is inserted for the detection of the moving mold element.

To prevent a difference between the predefined closing direction and the one inserted in the user interface, the user-defined information is also used to create the boundary conditions. Since the amplitude of the moving mold boundary condition is controlled by a used amplitude subroutine (VUAMP), the initial amplitude needs to be defined. Therefore, a subroutine specific property value is used. Since this specific property cannot be assigned via Abaqus CAE, the keyword editor is used within this initialization plug-in.

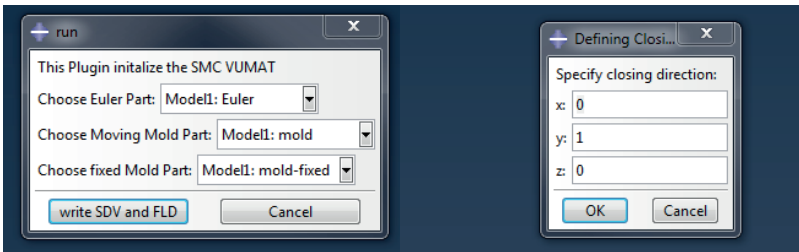


Figure 4-9: Initialization Plug-in interface to initialize the geometrical information for the lubrication layer detection

The second part of the plug-in can be used to initialize the fiber orientation of predefined element sets, which represent the initial charge. This can be done by assigning the fiber orientation to element sets or to each individual element by using the state variables. Since the initialization of the geometric in-

formation defines the state variables of each element, the initial fiber orientation distribution also needs to be defined element-wise. Since this definition is not available within Abaqus CAE and in order to simplify the function for the user, the plug-in offers the definition of fiber orientation distribution for predefined element sets (see Figure 4-10). By using the keyword editor, the initial fiber orientation distribution is then written into the model.

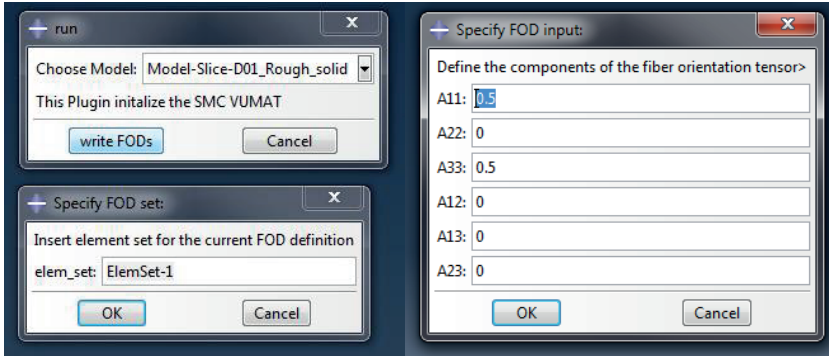


Figure 4-10: GUI to initialize the fiber orientation tensor for predefined element sets of the initial charge

VUAMP - Closing speed control of the moving mold

The user amplitude subroutine VUAMP is used to determine the closing speed of the current increment. The amplitude of the closing speed in the first increment is achieved from the Initialization Plug-in, by the property definition. For the further increments, the amplitude is calculated depending on the chosen closing mode. Since the closing direction is defined by the unity vector, the closing speed amplitude is independent of the closing direction.

Besides the update of the amplitude, the VUAMP calculates the total displacement of the moving mold in closing direction from the beginning of the step. This information is needed in the VUMAT to identify the Eulerian elements, which are in interaction with the moving mold surface. This could not be done

directly within the user amplitude subroutine, as it is not accessing the single elements. Therefore, the current total movement is passed to the VUSDFLD to be processed thereby using a global array. Since the VUAMP has no direct output to state or field variables, the global array is the only possibility to transfer data. In this case, a global array is an array that can be freely assigned and called by all subroutines.

Within the VUAMP, an updated amplitude for a constant deformation rate or a constant closing speed can be calculated. Up to now, no switch from speed to force control is implemented, but all interfaces for such a control are pre-defined within the subroutine.

VUSDFLD - User defined state variables and field subroutine

This subroutine has the two targets: to identify the Eulerian elements which are in interaction with the mold surface and to transfer the geometrical information from the state variables to the field variables. This is necessary to prevent the usage of averaged geometrical information, which could occur due to the advective transport and therefore mixture of state variables information.

To identify the interaction elements, the current total displacement is achieved from the VUAMP and is compared with the two limits of the minimal and the maximal distance to the nearest mold surface point at the initial state. By using a flag, this interaction information is passed to the VUMAT by the state variables. Since the VUSDFLD is called before the VUMAT, the transport of the state variables is not relevant. To prevent a simultaneous multiple usage of the global array, the thread safety needs to be secured. Therefore, a mutex initialized within the user defined external program subroutine (VEXTERNALDB) is used. This mutex blocks the global array for other processes, while one process is accessing and is writing input to it.

The geometrical information for the interaction needs to be stored as element-based information. Therefore, the state variables are used, as they are the only available element-based arrays in the initial step. The field variables can only be initialized at the nodes, which would lead to a mixture of information on the element level. Due to the effect that the state variables are transported by the advective terms, a mixture would occur leading to wrong geometrical information. Within the VUSDFLD, it is possible to define field variables at the integration points, which are the element centers for the Eulerian elements (EC3D8R or EC3D8RT). Therefore, all geometrical information is transferred from the state to the field variables during the first increment. Apart from that, since the CEL method is not considering every Eulerian element in every increment, it is checked, whether a new element is processed and, if necessary, the information is transferred.

VUMAT - User material subroutine

Within this VUMAT, the SMC material stresses and the fiber orientation distributions are calculated. For the stress calculation, the superposition of the compressibility pressure p , the rheological stress σ_{rheo} and the hydrodynamic friction stress Σ_{fric} is used (cf. eq. (44)). To calculate these stresses, the developed models from Section 4.2.1 are used.

The compressibility pressure is based on the incompressible hyperelastic material formulation given in eq. (60). Therefore, the bulk modulus is implemented as a material property, which is stored in the material card.

The rheological stress is calculated using an anisotropic viscosity tensor η dependent on the deformation gradient \mathbf{D} , which is composed of the extensional and shear viscosity. Therefore, the extensional and the shear viscosity are using different models. For the shear viscosity, the reactive-viscosity model (see eq. 42) is used. To calculate the extensional viscosity, the temper-

ature dependent power-law function from eq. 46 is implemented. The coefficients of the shear and extensional viscosity models are implemented as materials properties, which can be easily modified within the material card in Abaqus CAE.

The third stress component is the friction stress of the lubrication layer. As already described in the plug-in and VUSDFLD Section, this term is activated by a flag, which indicates, that the current Euler element is in interaction with the mold surface. In this case, the stress is calculated by using eq. 56. If the Euler element is in interaction with the fixed mold surface, the interaction area is precalculated and stored in the geometrical information in the field variables, before the simulation is started by the plug-in script. For the interaction with the moving mold, the interaction has to be calculated during every increment. Therefore, the coordinates of the corresponding element nodes as well as a reference point of the surface and its surface normal are used. This information is also part of the element specific field variables. The two parameter of this model are also part of the material card within Abaqus CAE.

Beside the stress update, the fiber orientation changes due to the flow kinetics are calculated. Since the fiber orientation is transported with the material, the advective transport properties of the state variables are used to store the components of the fiber orientation tensor and to ensure the correct transport. Due to this transport, the stochastically based constraint of $\text{tr}(\mathbf{A}) \equiv 1$ needs to be checked and restored at the beginning of every increment, if necessary.

After transferring the fiber orientation tensor into its eigenvector coordinate system, the fiber orientation change is calculated by using the Folgar-Tucker ARD-RSC model (cf. Section 2.4). To approximate the fourth order fiber orientation tensor \mathbb{A} from the second order tensor \mathbf{A} , the Invariant Based Optimal Fitting (IBOF) closure approximation is used (cf. Section 2.4). Therefore, the new fiber orientation tensor can be calculated by

$$\mathbf{A}_{new} = \mathbf{A}_{old} + \dot{\mathbf{A}} dt . \quad (62)$$

After transferring this new fiber orientation into the global coordinate system, the tensor is stored in the state variables, which are passed to the next increment.

4.2.3. Effects of simulation settings on numerical stability and accuracy

Two parameters have a major influence on the simulation quality: the bulk viscosity and the time increment range.

The bulk viscosity introduces an extra damping to the simulation, associated with the volumetric strain. Although it is intended for high-speed events, it also has an influence on the Fluid-Structure-Interaction in the SMC simulation. Especially in the contact regions between the tool surface and the SMC material, a high influence of the bulk viscosity on the penetration can be observed. Due to this penetration, a parameter study based on the default values is made. By increasing both, the linear and the quadratic bulk viscosity parameter, a better interaction surface with a lower penetration can be achieved. Three results with the default, an increased and a decreased linear and quadratic bulk viscosity parameter set by one decade is plotted in Figure 4-11. Furthermore, the resulting total pressure is given in this plot. For the reduced and the original linear and quadratic bulk viscosity parameter set, the pressure is nearly the same. For the increased parameters, the pressure is significantly higher and the simulation is terminated due to numerical problems. Due to these effects, an increase above the factor of 10 of the linear and the quadratic bulk viscosity parameter reduces the penetration, but leads to numerical instabilities in the simulation and should therefore be avoided.

4. Process simulation of hybrid SMC

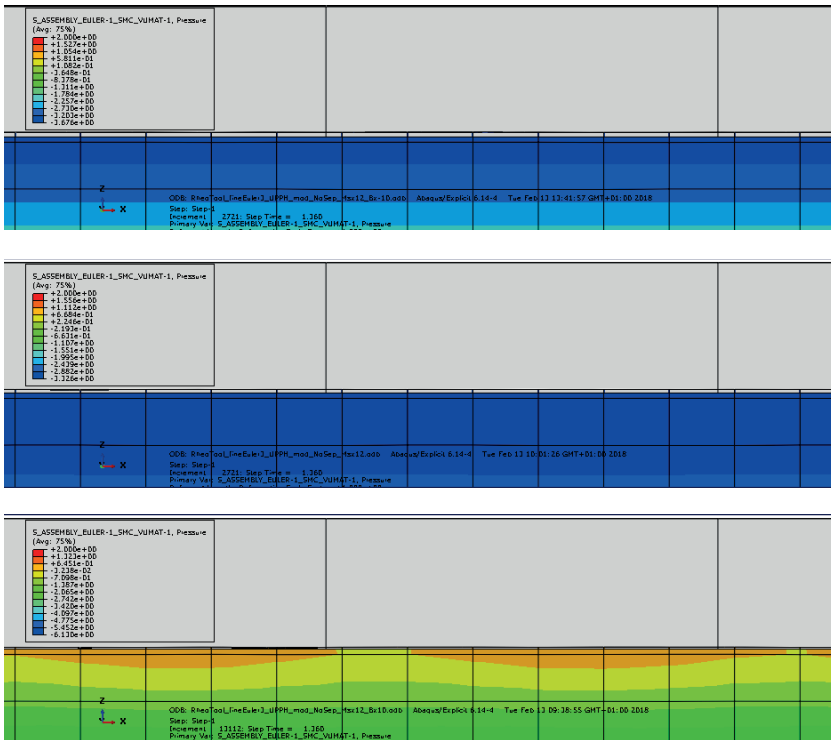


Figure 4-11: Evaluation of the penetration of the SMC through the mold surface depending on the bulk viscosity parameter: reduced (top), original (middle) and increased parameter set (bottom)

The second important setting for a Coupled-Eulerian-Lagrangian simulation is the range of the valid time increment range. Typically, this increment value is calculated automatically by using the element maximum eigenvalue and the speed of sound in the SMC material. Depending on the complexity of the cavity and the mesh quality, this increment can be too large. Therefore, a maximum increment is recommended in the range of $1e-4$ to $1e-5$ s to ensure the correct considering of local deformation effects.

4.2.4. Consideration of local reinforcements

The possibility to consider local reinforcements is one of the advantages of the CEL compression molding approach. Since the CEL formulation divides the increment into a Lagrangian and an Eulerian step (cf. Section 2.5), the interaction of the SMC and a local reinforcement is considered in the Lagrangian step. In this step, the Fluid-Structure-Interaction is simplified to a Structure-Structure-Interaction using an extrapolated surface for the SMC material (cf. Section 2.5). Therefore, the tangential and the normal contact behavior need to be defined. Furthermore, the thermal conductivity could be defined, if the local reinforcement and the SMC are placed into the mold with different temperatures. Since the basic contact model used for the interaction between the SMC material and the tools is considering the interaction of every section element with every other section, the reinforcement-SMC and reinforcement-tool-interaction need to be defined by assigning contact surface pairs.

Since the material is flowing around the reinforcements and due to the penetration method for the interaction, it is recommended to use solid elements for the reinforcements. This ensures the distinctive determination of the surfaces and their normal, as well as the flow directions at which they are located. Otherwise, the direction of the restoring force is not necessarily correctly defined (see Figure 2-13).

In most cases, the local reinforcement reduces the gap height significant. Therefore, a special focus on the mesh near the reinforcement is necessary. To predict a correct flow, at least four elements over the thickness are required. This leads to an essential mesh refinement around the reinforcement and its probable moving direction to ensure the minimum element numbers during the whole molding process.

For the material properties of the reinforcements, every available formulation defined for solid elements can be used. Furthermore, self-written user material subroutines (VUMAT) can be used. If this is done, a survey of the

material sections within both VUMATs is required to clearly identify the relation between the element and the corresponding material. Such a VUMAT can be used to consider the material behavior of unidirectional tape reinforcement and their fiber reorientation and fiber volume change.

After the individual property assignment, the interaction properties need to be defined. Compared to the standard SMC compression molding simulation, interactions between the SMC and the local reinforcements and if necessary between the reinforcement and the molding tool have to be modelled. Examples of such a consideration of isotropic local reinforcements by using a standard elastic material card are presented and discussed in Section 4.3.2.

4.3. Validation of hybrid SMC process simulation

To validate the SMC model developed and implemented in Sections 4.2.1 and 4.2.2, two different parts are used. On the one hand, the pressure distribution is compared with the results from the characterization experiments from Section 3.2. Beside the pressure, the fiber orientation distribution of the CT-scans (Section 4.1) is used as a validation criterion. On the other hand, the IRTG reference structure with local unidirectional reinforcements is simulated to evaluate the flow behavior of the SMC. For this part, the fiber orientation and the reinforcement displacement are compared with the experiments.

4.3.1. 2D flow within the rheological tool

4.3.1.1. Model configuration

In this first validation step, the rheological tool presented in Section 3.1 and the pressure results shown in 3.2 are used. Therefore, the local effects and pressure changes should be resolved within the CEL model of the tool. In order to stay with a reasonable number of elements, only a section of the rheological tool is simulated. To ensure the same flow as in the real process, symmetrical boundary conditions are assumed. This is permissible since the

pressure sensors are aligned in the middle of the tool. The model has a width of 10 mm, which is resolved with three elements. Three elements are used as a compromise to avoid fully constraint elements, if one element is used, on the one side, and to keep the number of elements low on the other side. In flow direction, the element edge length is set to 0.5 mm to precisely describe the flow front. This leads to a total number of 240 000 Eulerian elements.

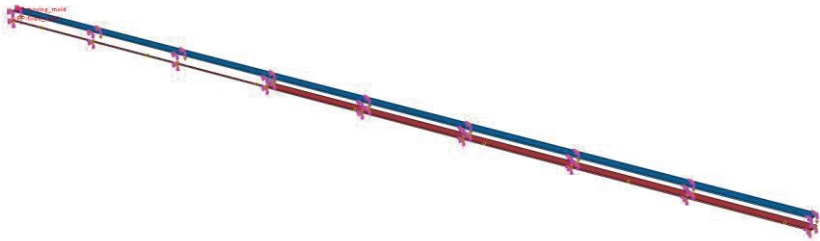


Figure 4-12: Boundary conditions of the Lagrangian Elements for the rheological tool CEL model with the initial charge (beige) configuration of the semi-structural SMCs

For the validation, the Class-A SMC, the Vinylester SMC and the UPPH carbon fiber SMC are simulated. The Low-Density Class-A SMC is omitted, since it has nearly the same material properties as the standard Class-A SMC (see Table 3-6).

For the process settings, the same values as for the characterization methods are used. To reduce the amount of simulations, only one closing speed of $\dot{h} = 1 \text{ mm s}^{-1}$ is considered. To ensure the correct viscosity of the SMC material, the initial temperature is set as 303.15 K (30 °C), which is also the reference temperature in the Arrhenius equation (see eq. (46)).

4.3.1.2. Simulation results

To validate the simulation models with the experiments, various simulations were carried out. Therefore, the different initial charge configurations for the different material formulations were considered as well as different mold

closing configurations with constant closing speeds and constant deformation rates.

During the simulation runs, an overall problem with the rheological tool model has emerged. Due to the boundary conditions with the moving tool side and the fixed tool side, only two degrees of freedom are left. These are the flow in x-direction and the compressibility of the SMC. Depending on the stress magnitudes of the rheological stress due to the deformation rate (see eq. 47) and the compression pressure (see eq. 60) this leads to a high compression of the material. Based on this compression and the resulting stored energy, little numerical variation within the model leads to high local stresses when the volume is expanding again, and therefore, to high local deformations. In some cases, this leads to very small time increments which are too small to simulate the whole compression process within an acceptable computational time. In other cases, these deformations lead to too high deformations and an error in the simulation. To identify the reason for these issues, a mesh refinement was done. This study showed no improvements regarding these local effects, so that mesh effects could be ruled out. In a next step, the rheological tool model was tested by using the same models as for the Moldflow simulations as well as standard implemented models from Abaqus. To utilize the models used by Moldflow, the Castro-Macosko model was implemented in a viscosity user subroutine (VUVISCOSITY) and the 2-Domain Tait Model in an user defined equation of state subroutine (VUEOS). Within these subroutines, the same material parameters as in the Moldflow simulations were used. This simulation also shows very small time increments in the same range as the SMC specific subroutines but slightly smaller. Furthermore, also this simulation gives an error after $5e-5$ s due to local density changes (see Figure 4-13 and the corresponding high stresses, which lead to too high element deformations).



Figure 4-13: Local density change within the Castro-Macosko model with the 2-Domain-Tait model

Additionally the standard Abaqus Mie-Grüneisen [Bae] equations of state and a constant viscosity in the same range as before were used. This simulation has a six decades smaller time increment, which means, that no results could be generated. The main reason for the very small time increments can be traced back to the viscosity value. By reducing the viscosity by one decade, the time increment is also reduced by one decade. This becomes obvious when looking at eq. 47, where the viscosity has a linear correlation with the stress and therefore with the deformation.

By comparing the results of the SMC specific material model, the Castro-Macosko model combined the 2-Domain-Tait model and the standard Mie-Grüneisen model with a constant viscosity, the advantages of the new developed SMC specific material model becomes clear. Due to the high viscosities of the SMC during the compression molding process small time increments cannot be avoided. Due to the separation of the extensional and shear viscosity, the SMC specific material model can handle them better than the standard models.

Since previous tests showed the capability of the presented SMC compression molding approach by using the CEL method for 3D flows, this is only a problem of this restricted model. One of these test results is given in Figure 4-14.

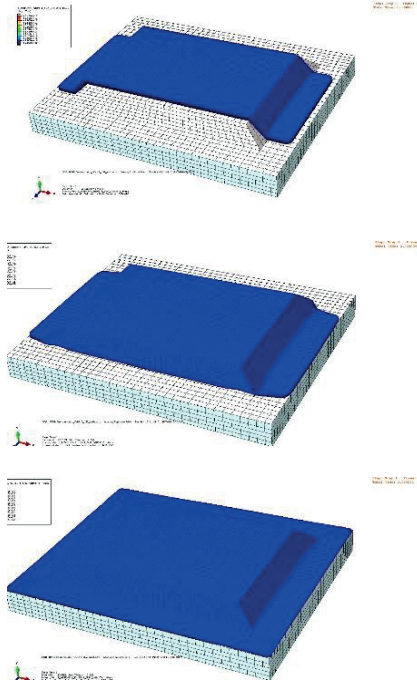


Figure 4-14: Results of a test mold filling simulation during the development process

To find the reason for the issues, the SMC specific material stresses (rheological and friction stress) and the compression pressure of a simulation run with a VE-SMC material at the sensor position 1 and 2 are shown in Figure 4-15. In this Figure, it can be recognized that the first typical stresses emerge after 0.075 s step time. This is due to the initial gap between the SMC and moving mold side of 0.05 mm to avoid initial problems. Therefore, the moving mold is in contact with the material after 0.05 s and the first material flow occurs after this. After the flow begins, the compression pressure reaches a 20 time

higher level than the rheological stresses. After approx. 0.7 s step time the first inaccuracies in the simulation occurs and the stress values at Sensor 1 are dropping. These phenomena are occurring all along the model and cannot be traced back to geometrical or numerical reasons.

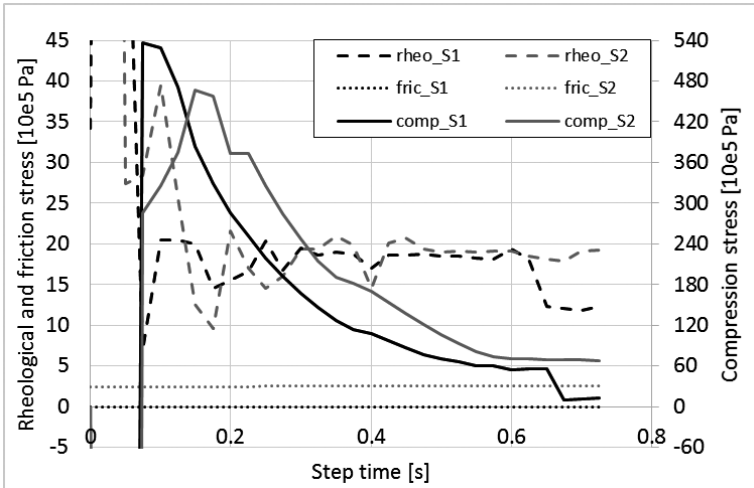


Figure 4-15: Rheological, friction and compression pressure stress for a VE-SMC material formulation at sensor position 1 and 2

Having a detailed look at the rheological and friction stress a slide oscillation of the rheological stresses can be observed. This is due to the change of the deformation rate tensor \mathbf{D} due to the compression changes. It can be also observed, that the friction stresses from the simulation is different from the analytical model. The friction stresses at Sensor 1 is zero over the given step time. This difference occurs, since the analytical model uses an integral measure over the complete flow length, while within the simulation discrete stresses are calculated. Within the simulation model, the total pressure is the integral equivalent to the superposition of the rheological and the friction stress in the analytical model. Here, the discrete friction stress at Sensor 1 is lower than the stress at Sensor 2, since no axial flow occurs at the end of the

rheological tool, the friction stress needs to be zero (see eq. 56). For the friction stress at Sensor 2 a slide increase can be observed, since the velocity of the material is increasing at a fixed point during the compression molding process.

Nevertheless, the simulation results show the typical plug-flow. Three short-shots are shown in Figure 4-16. Within this Figure, a slide ahead running of the SMC material near the mold surface can be observed. This is a typical SMC specific material behavior, which was already observed by Barone and Caulk [Bar85] (see Figure 2-4).

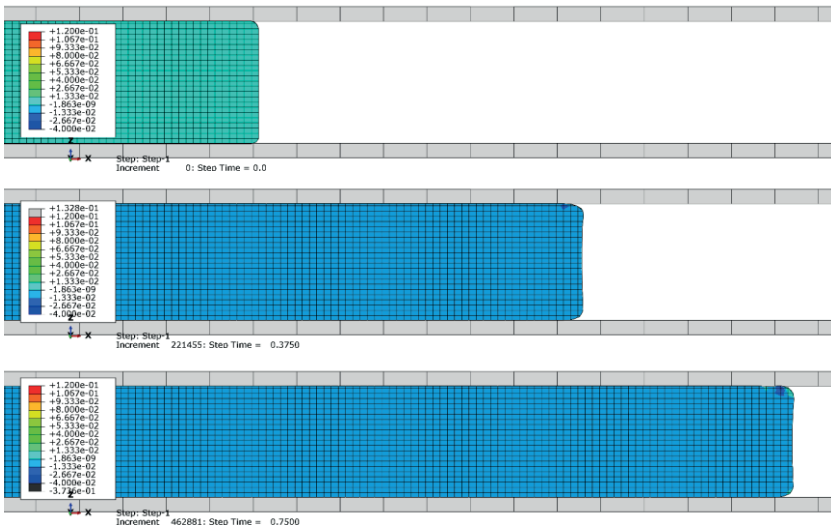


Figure 4-16: Evaluation of the flow front with the compression stresses at $t = 0$ s (top), $t = 0.375$ s (middle) and $t = 0.75$ s (bottom)

Since the simulations are not finishing, no validation with the experiments can be performed. Nevertheless, to show the capability of the new developed material model, the different material formulations are compared with each

other. Therefore, a quantitative evaluation can be performed, since flow effects due to the different initial conditions are excluded. To do so, the Class-A configuration with an initial charge length of $l_0 = 300$ mm is used.

These simulations have the issues with the compression behavior like the previous presented VE-SMC simulation results. Nevertheless, a sensitivity to the material parameter can be observed, when comparing the stable step times. The Class-A SMC has the shortest stable step time, while the VE-SMC runs twice as long and the UPPH-SMC thrice the time. This result, together with the pre-studies, shows a special sensitivity to the rheological stress power-law coefficient n . Since this is higher for the Class-A SMC compared to the semi-structural SMCs (see Table 3-6), a higher sensitivity to changes of the deformation rate tensor \mathbf{D} occurs. This can also be seen in the lower stable time increment during the simulation. Since the compression leads to such local changes, it is to be expected that within the Class-A SMC simulation high element distortions occur earlier.

To compare the simulation results, the stress distributions for the Class-A SMC is given in Figure 4-17, for the VE SMC in Figure 4-18 and for the carbon fiber UPPH SMC in Figure 4-19. All these three pressure curves show the SMC typical pattern with the high increase at the beginning due to the rheological stress and the threshold after this first increase. The semi-structural SMC formulations show some overshoots at the beginning, but converge to the threshold after a short time. This is once again an effect of the compression stress and the resulting local deformation rate change.

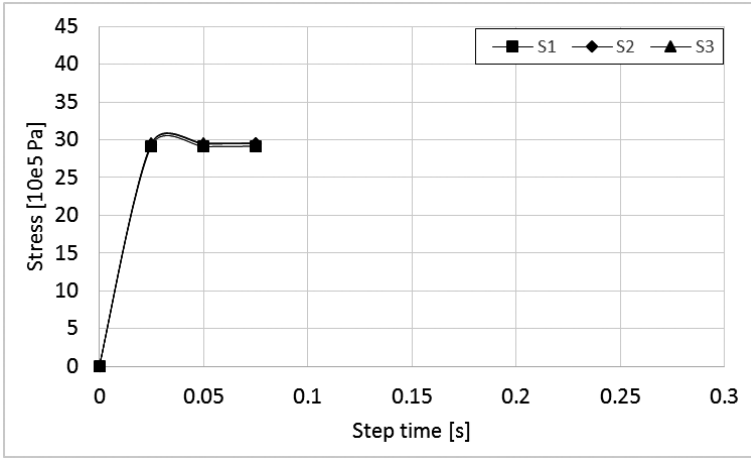


Figure 4-17: Simulated stress distribution for Sensor 1 to 3 for the Class-A-SMC material

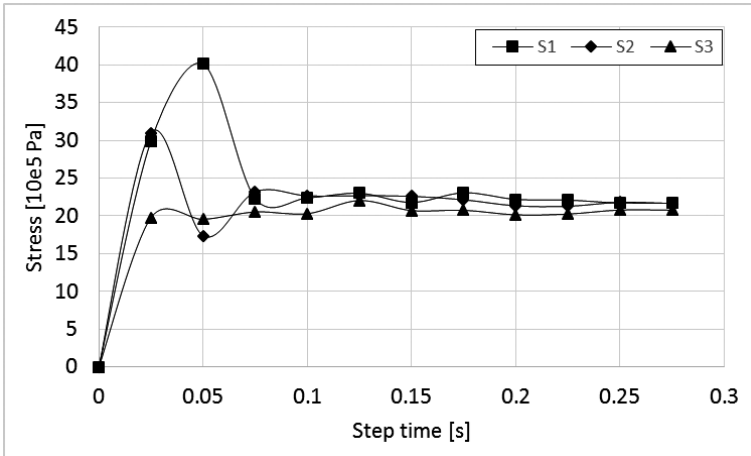


Figure 4-18: Simulated stress distribution for Sensor 1 to 3 for the VE-SMC material

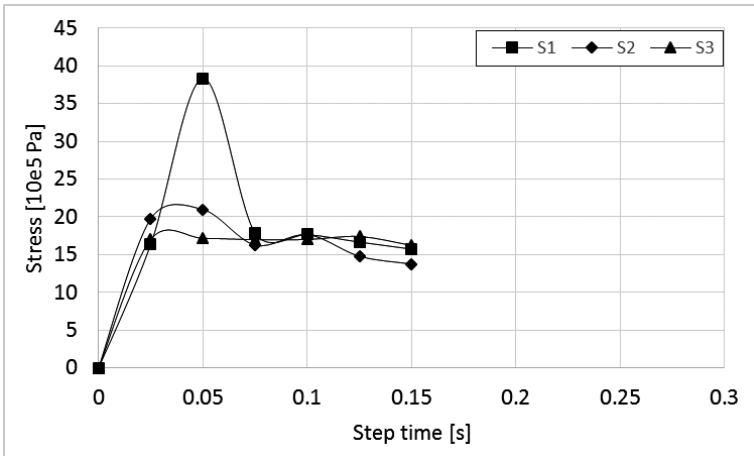


Figure 4-19: Simulated stress distribution for Sensor 1 to 3 for the carbon UPPH-SMC material

Comparing these three figures it can be observed, that the correct tendencies of the pressure peaks compared to the material parameters (see Table 3-6) are obtained. The Class-A SMC has a higher extensional viscosity and a higher rheological power-law coefficient than the UPPH carbon fiber SMC. Consequently, the predicted stress is also higher. The VE-SMC has the same material parameter as the UPPH carbon fiber SMC, but a higher extensional viscosity. Therefore, the predicted stress is higher.

Nevertheless, comparing the VE-SMC and the carbon UPPH SMC, gives the reasons for the difference to the experiments. Comparing the experimental pressure curves for the VE-SMC (see Figure 3-5) and the UPPH SMC (see Figure 3-7) and on the extensional viscosities given in Table 3-6, the VE-SMC should have a three times higher stress threshold than the carbon UPPH SMC while having the same deformation rates. Nevertheless, the simulation shows a 30 % higher pressure for the VE-SMC formulation. Having a detailed look at the simulation results, Figure 4-20 shows a comparison of the compression based on the determinant of the deformation gradient ($\det(\mathbf{F})$) and Figure

4-21 a comparison of the displacement in flow direction for the two semi-structural SMC materials. These two figures show the effect of the compression on the displacements and therefore also on the deformation rate (see eq. 49 to 54). Already after 0.025 s simulation time, the VE SMC process simulation shows a higher compression (lower determinant of the deformation gradient) compared to the UPPH SMC process simulation. This can be attributed to the higher rheological stresses due to the higher reference plain strain extensional viscosity of the VE SMC. Since the compression leads to a reduction of the volume, some material is flowing opposed to the flow direction near the end of the cavity (negative material displacement at the left end in Figure 4-20 and Figure 4-21). This change of the idealized constant deformation along the material leads to a reduced deformation rate tensor D and therefore to a reduction of the local rheological stresses. Furthermore, an oscillating displacement near the flow front can be observed. In this area, the displacement is changing between zero and the maximum value. Since these high gradients are not occurring once, but over the half material, this is once again an effect of minimal numerical changes in the compression at an increment.

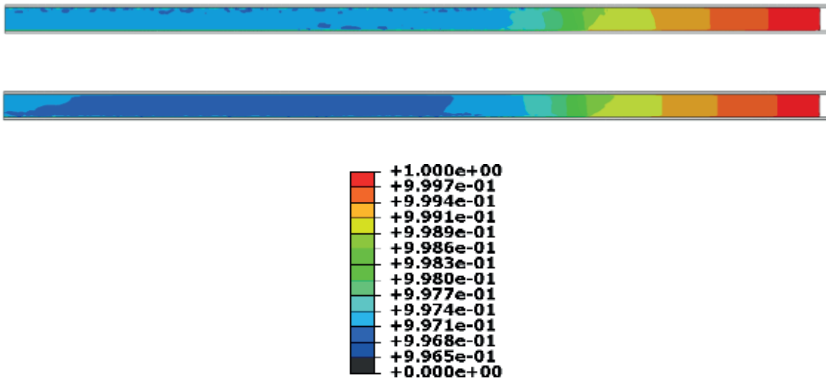


Figure 4-20: Comparison of the compressibility ($\det(F)$, see eq. 60) of the carbon UPPH SMC (top) and VE SMC (bottom) after 0.025 s simulation time

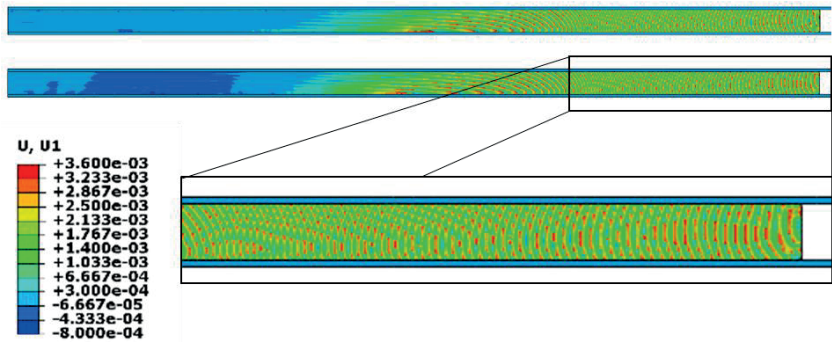


Figure 4-21: Comparison of the displacement in flow direction (U_1) of the carbon UPPH SMC (top) and VE SMC (bottom) after 0.025 s simulation time

Since the presented simulation results are made with the Class-A SMC initial configuration, a comparison of the VE-SMC simulation with the experiments can be done roughly. Therefore, both pressure curves are combined in Figure 4-22. The experimental pressure curves have the compaction phase at the beginning, where the entrapped air is released and inhomogeneities in the thickness are smoothed. Since the simulation starts with ideal conditions, this is not modeled and therefore different times are needed until the rheological stress threshold is reached. If this is considered within the definition of the Initial Charge thickness, this has no effect for the further simulation. Furthermore, the thickness inhomogeneities are the reason why the experimental curves are not on top of each other in this phase. Nevertheless, this Figure shows the correct stress prediction of the rheological stress during this phase.

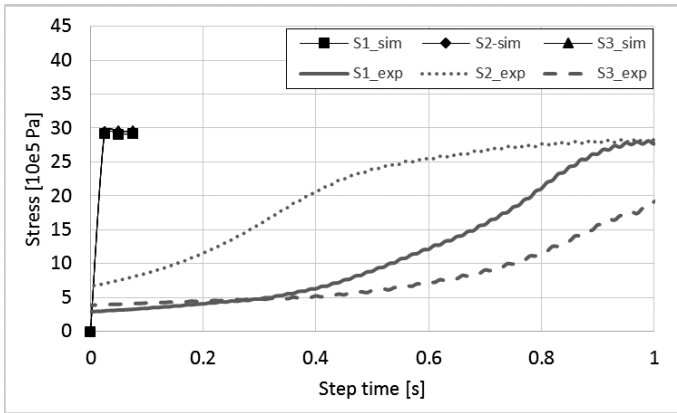


Figure 4-22: Comparison of the simulation results with the experiments of the Class-A material formulation

These process simulation results show the possibilities of the new developed SMC process simulation based on the CEL approach. Comparing the simulation results from the commercial compression molding simulation with the SMC-specific material model results within CEL the advantages of the new approach becomes obvious. Comparing the flow fronts of the commercial simulation tool (see Figure 4-5) with the SMC-specific material model (see Figure 4-21) and the pressure curves (see Figure 4-2 and Figure 4-15) the correct flow kinetic with the SMC specific plug-flow can be predicted with the new approach. Due to this flow kinetics with the elongation based core region and the resin-rich lubrication layer, the pressure distribution can be predicted better due to the superposition of the rheological and friction stresses. Furthermore, the reliable flow prediction leads to a better prediction of the Fiber Orientation Distribution, since they only depends on the flow fields.

Nevertheless, due to the issues with the compression behavior during the compression molding simulation, these simulations were not able to finish without an error. Therefore, better suitable compression pressure models needs to be developed, which can fulfill the criteria for the Coupled-Eulerian-

Lagrangian approach and the SMC specific compression behavior. Therefore, some extensions, which might replace the scalar bulk modulus by a tensor, could help to overcome the current issues. Such a tensor should not lead to an anisotropic bulk modulus but should describe the bulk modulus as a function of stresses, compression state and other state variables.

4.3.2. IRTG reference structure without ribs

4.3.2.1. Model configuration

Within the International Research Training Group (IRTG) GRK2078, a reference structure was developed to show the different effects of the local unidirectional reinforcements in combination with SMC. This reference structure applies the rheological tool from Section 3.1, which has a replaceable insert in the middle section. By using this insert, a beading is introduced into the flat plate (see Figure 4-23). The beading angles are chosen differently in order to achieve asymmetric deformation of the molded part in the basic configuration in a four-point bending test. The beading angles towards the long plate ends are defined as 45° , while the other angles are set to 60° (positive y-direction) and 40° (negative y-direction). To create more homogeneous tensions, two unidirectional reinforcements with slightly different widths were inserted. The shape and the position of these two unidirectional reinforcements are also given in Figure 4-23 (green part).

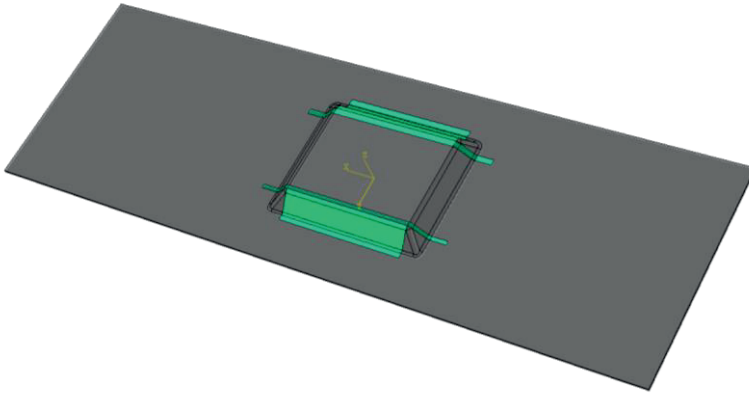


Figure 4-23: IRTG reference structure with the position of the local reinforcements (green)

The preformed initial charge was placed over the beadings. The top layer of the initial charge had a cutout for the unidirectional reinforcements (see Figure 4-24), so they are fixated at the beginning of the molding process (see Figure 4-24). The mold closing speed was set to 1 mm s^{-1} and the maximum press pressure to 2500 kN. Due to the inserts, the pressure measuring system used for the rheological characterization could not be used during the part manufacturing.

In the real part manufacturing, the semi-structural UPPH carbon and glass fiber SMC (cf. Section 3.2.4 and 3.2.5) were used as SMC materials. Due to the different and uncommon flow behavior of the UPPH glass fiber SMC (cf. Section 3.7), only the carbon fiber SMC is simulated. For the process settings, a closing speed of $\dot{h} = 1 \text{ mm s}^{-1}$ were used. The initial charge had a temperature of 303.15 K (30 °C), while the tool was tempered to 418.15 K (145 °C).

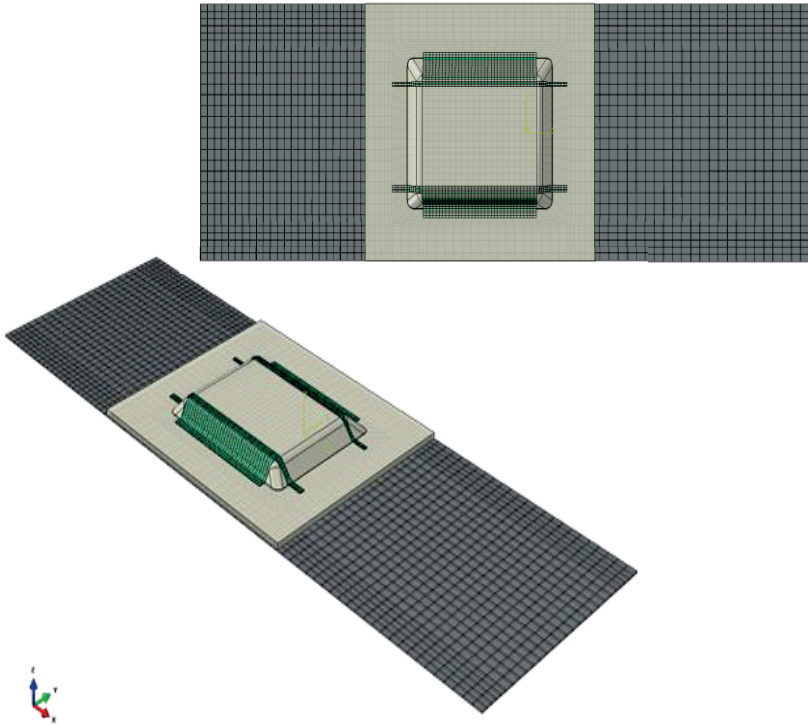


Figure 4-24: Initial configuration of the process simulation of the IRTG reference structure with the local unidirectional reinforcements (green) and the initial charge (beige)

To achieve a mesh with Eulerian elements, which are mainly aligned in flow direction and which have a high mesh quality, a block-structured meshing method is used. Therefore, the Eulerian domain is predefined within a CAD model by defining the maximum mold opening distance and the necessary element overlap over the Lagrangian mold surfaces (cf. Section 2.5). To ensure a high mesh resolution in the area of the beading, while having a reduced resolution in the flat area, an O-Grid is inserted (see Figure 4-25) within ICEM CFD. Furthermore, a mesh refinement is introduced in the thickness direction

to ensure the minimum element number at the end of the molding simulation. Therefore, different layers with different element heights and a smoothing via biasing is introduced. After exporting and converting the mesh, it could be used within Abaqus.

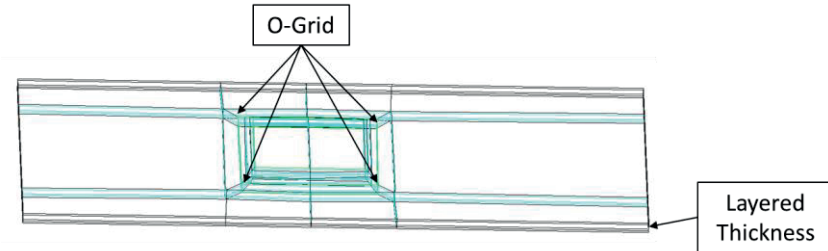


Figure 4-25: Blocking of the Eulerian mesh of the IRTG reference structure

To model the precured local unidirectional reinforcements, homogenized material properties based on a Cantilever test (DIN 53362) provided by the Institute of Production Science (wbk) were used. The interaction between the mold surface and the reinforcement is assumed to be rough, so that no slip will occur, if both are in contact.

The initial charge of the SMC is formed to the 3D geometry of the beading. Therefore, the fiber orientation is not homogeneously quasi transversal isotropic in the global x-y plane. To predefine the correct fiber orientations in the flanks of the beading, a script is written to subdivide the element set provided by the volume fraction tool, which defines the position of the initial charge within the Eulerian elements. After getting the sets for the initial charge elements in the different flank regions, the correct rotated quasi transversal isotropic fiber orientation tensor could be predefined in the model.

Due to the high number of elements and the relatively long flow length, the calculation with the same material parameters and process condition as in the experiments would take more than one month. Therefore, the lubrication

layer is not considered in this model, as the effect for such a one-dimensional flow can be neglected, since no pressure controlled closing speed is applied and no pressure validation is done. Furthermore, a mass scaling is done, which decreases the computational time dramatically, but slightly increases the compressibility of the material at the beginning of the compression molding process. According to numerical pre-studies, these simplifications effect the result in an acceptable range compared to the amount of saved computational time.

4.3.2.2. Simulation results

To validate the simulation results quantitatively, the patch displacement is the most important criteria. Although no UD-patch material model was used, but an isotropic one, the propensity to patch displacement or deformation can be evaluated. A representative picture of the final plate with the patches is given in Figure 4-26. This picture shows a configuration with the UPPH glass fiber SMC with continuous carbon fiber patches, also based on the UPPH resin. The patches are made out of two layers with a $[0, 90]$ configuration. By evaluating the displacements of the local patches of the six manufactured samples, almost no displacement was observed in the main area (see Figure 4-26). Only at the end of the tapes, where the thin arms are, some displacement could be observed (see Figure 4-26 bottom). In some cases, a small rotation of the whole patch could be observed in the final part, which was traced back to little misalignments during the stacking of the tapes and the initial charge due to the manual process. Since these rotations are initially introduced, also no displacement occurs during the process.

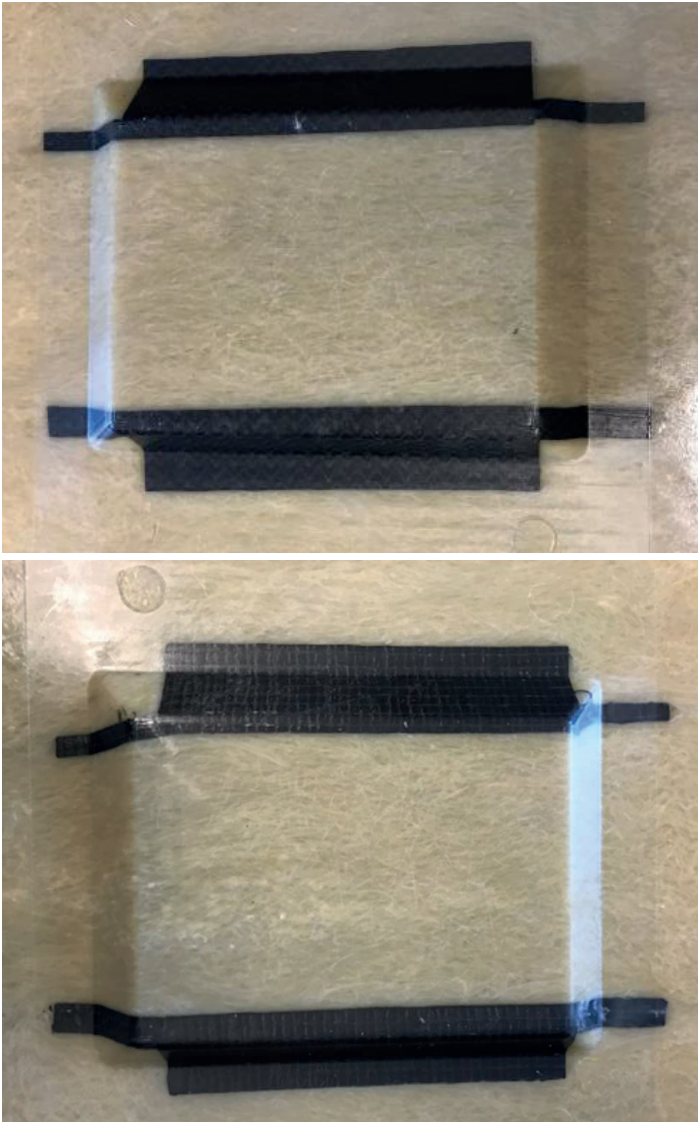


Figure 4-26: Photos of the molded reference structure with local reinforcements with no deformation of the tapes (top) and slide deformation at the end of the tapes (bottom) [But17]

To compare the simulation results with the experiments, the patch displacements divided into the three coordinate directions are given in Figure 4-27, Figure 4-28 and Figure 4-29. The in-plane directions (x and y), plotted in Figure 4-27 and Figure 4-28, show nearly no displacements of the patches. Since the mold-opening gap in the flanks is changing differently than the planar areas, a forming of the tapes into the final configuration can be observed. At the end of the tapes, were they are very small, further displacements can be observed. For the lower tape, this end region is elongated in flow direction up to 1.35 mm and shows a small deflection of 0.5 mm. For these in-plane displacements it can be observed, that both tapes are behaving differently. This is due to the different shapes of the tapes as well as the different angles of the flanks. This effect was also observed during the experiments, since the non-symmetric geometry of the reference structure leads to a non-symmetric flow. The prediction of these different deformation behaviors of both tapes shows the advantages of the SMC specific material model with the Fluid-Structure-Interaction.

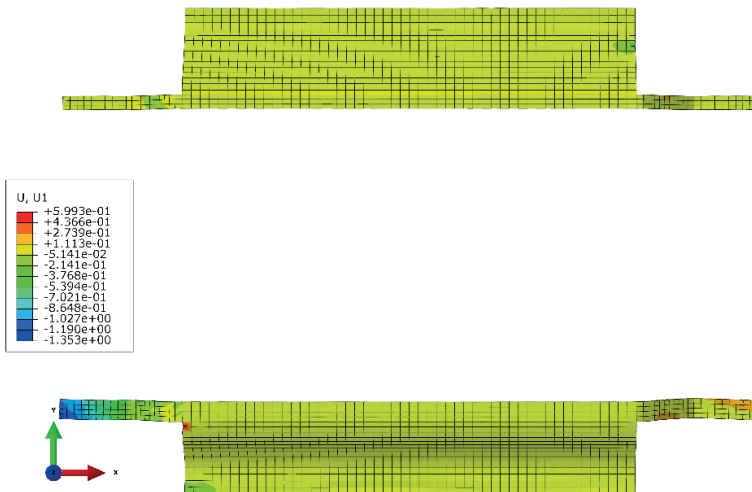


Figure 4-27: Displacement of the tapes during the compression molding process in flow direction

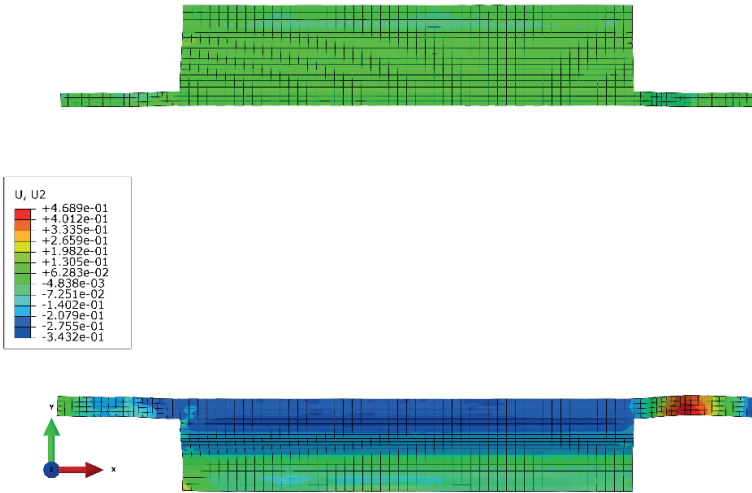


Figure 4-28: Displacement of the tapes during the compression molding process in-plane perpendicular to the flow direction

In Figure 4-29 the displacement of the tapes in closing direction is given. Since the tapes are placed on top of the initial charge, they need to follow the upper mold movement. Therefore, they need to push back the SMC material under it without being compressed. The simulation results show that the planar regions of the tapes are following the displacement, while in the flank regions higher displacements can be observed. This is once again a forming process since the initial tape shape is not exactly the finale one. This forming in the flank area leads to a higher deformation of the lower patch in the main in-plane area (in Figure 4-29 at the very bottom) due to the relative stiff patch material. As a consequence, this displacements leads to a higher deformation of the SMC material and therefore to a higher pressure under this patch area (see Figure 4-30). The prediction of such an interaction is a clear advantage towards all available SMC process simulation tools.

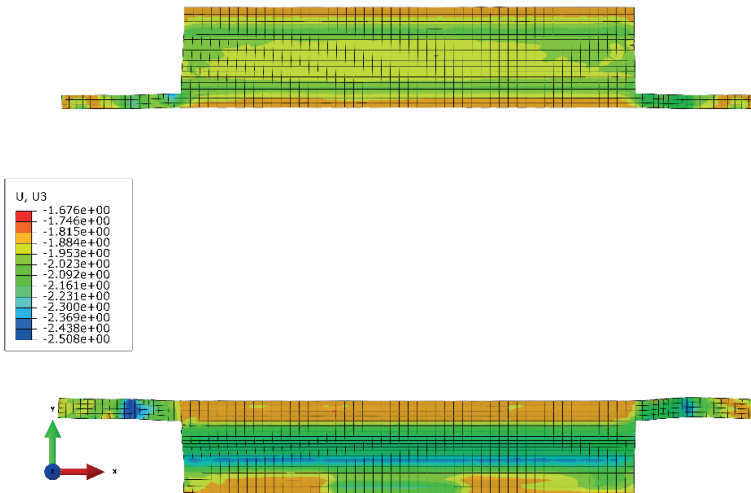


Figure 4-29: Displacement of the tapes during the compression molding process in compression direction (bottom)

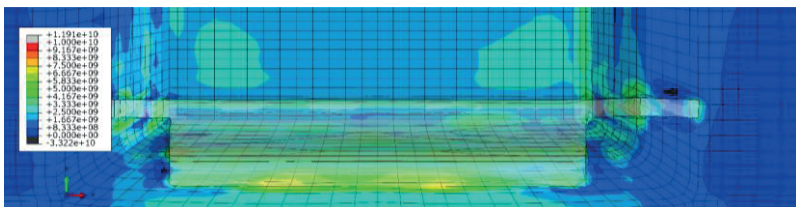


Figure 4-30: Pressure of the SMC under the lower patch due to the patch deformation

Comparing the experiments with the process simulation results in terms of the patch displacement, good agreements can be achieved, since the tape is following the tool movement in closing direction, but no displacement in the in-plane direction occurs. Besides the displacements it can be also observed, that no SMC material is flowing between the tool side and the patches. This

indicates that the interaction properties and simulation setting (see Section 4.2.3) are also valid for this type of simulation with further Lagrangian parts.

4.4. Summary process simulation

In this chapter, the inaccuracies of commercial compression molding software for SMC were shown. To overcome these problems, a new simulation method based on the Coupled-Eulerian-Lagrangian approach is developed and presented. This approach has the capability to predict the stresses of the SMC-specific core region and lubrication layer. Furthermore, the interaction with local reinforcements or inserts is possible. During the validation, these approaches and their functionality were generally shown. By comparing the first threshold level of the rheological stresses at the beginning of the compression molding process for the Class-A SMC formulation, the correct pressure could be predicted in the simulation. Due to the compression behavior of the simulated material, the match for the semi-structural SMC formulations were not as good as the one for the Class-A SMC formulations. In the second step, the interaction of local reinforcements with the SMC was shown. By using the IRTG reference structure the correct displacement in flow direction was predicted as well as the forming process in the closing direction.

These two examples show the advantages of the new developed SMC specific material model. The model has the capability to predict the correct SMC specific pressure distribution with its rheological and friction parts. Furthermore, the full interaction of the SMC with local reinforcements was shown, which is currently a unique method for Sheet Molding Compound compression molding.

5. Process simulation within a CAE chain for long-fiber reinforced composites

Due to the fiber reorientation during the compression molding process, the consideration of the final fiber orientation distribution is crucial for the structural simulation. Since this also affects the design, a holistic approach is necessary. Therefore, the Institute of Vehicle System Technology (FAST) – Lightweight Technology is focusing on the CAE-Chain, which combines different simulation tools and enables the transfer of information between them. Therefore, the single FE simulation tools, which are used during the steps Design, Optimization, Process Simulation, Mapping and Structural Simulation, are connected. In this CAE-chain, each step has criteria that must be fulfilled before results are passed to the next step. Otherwise, a process internal optimization tries to fulfill the criteria by changing free parameters. If this is not possible or if the internal optimization fails, the previous step is done again with a varied parameter set. [Hoh16b]

The structure of the CAE chain developed at KIT-FAST is presented in Figure 5-1.

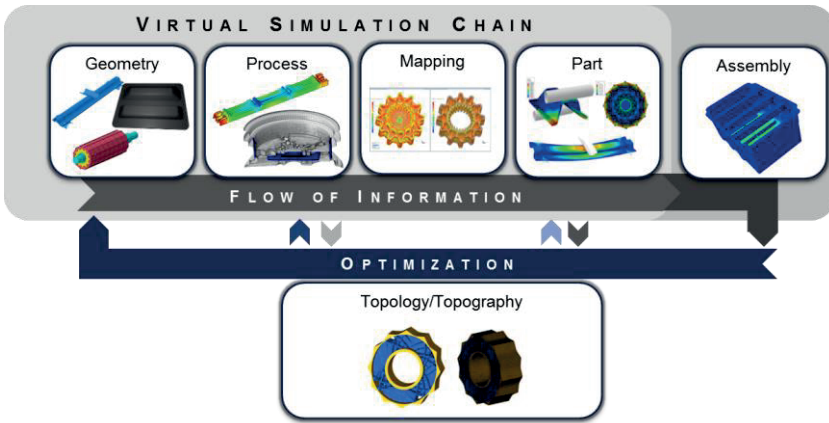


Figure 5-1: Steps of the CAE-Chain at KIT-FAST [Hoh16b]

To transfer the information from the short or long fiber process simulation (injection or compression molding) to the structural simulation, a plug-in called *Fibermap* is developed within Abaqus, which can export and process the fiber orientation distributions. Furthermore, the mapping, clustering and a homogenization are part of the plug-in. All these steps of the *Fibermap* plug-in can be executed via a GUI within Abaqus (see Figure 5-2) or via single scripts by using the Abaqus command line.

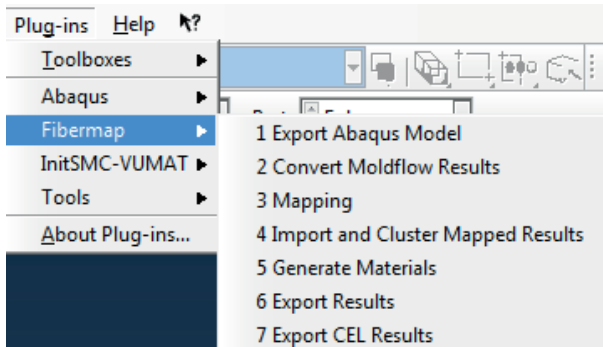


Figure 5-2: GUI selection tree of the Fibermap plug-in within Abaqus

The processing of the mesh and result information is done using the neutral transfer format VTK. The VTK-file uses the ASCII encoding and consists of the mesh with the corresponding nodes and elements as well as the result information. This information is assigned to attributes. Therefore, various different types of results can be stored in a single VTK-file. In the following sections, the main steps of the CAE-chain provided by the *Fibermap* plugin are described. Therefore, the steps export of results, mapping and homogenization are discussed and the used methods are explained.

5.1. Export of results

The processing of the fiber orientation is realized for the simulation with the commercial process simulation tool Moldflow as well as for the internally extended Abaqus CEL process simulation. Due to the different input file formats, two different scrips are necessary. The subscript “Convert Moldflow Results” uses the exported Patran mesh and the element based fiber orientation as input (see Figure 5-3). These two files have to be generated within the commercial process simulation tool before using the script. In some cases, not-filled elements can cause some issues for the post processing. Therefore, the

“Autoremove” function is inserted to give the user the option to remove these unfilled elements. As the outcome of the script, a VTK file including the fiber orientation distribution is generated. In this VTK file, the fiber orientation distribution is defined in the tensor notation. Therefore, a 3×3 result matrix is given for every element.

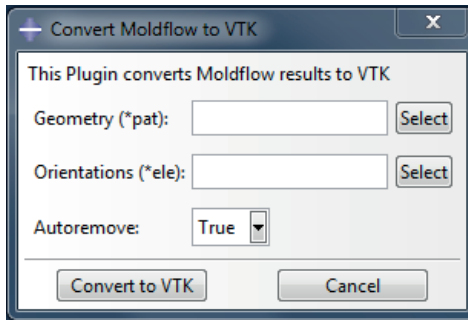


Figure 5-3: GUI of the VTK converter for the process simulation with Moldflow

For the export of the fiber orientation from the process simulation with Abaqus CEL, the VTK file is generated from the result (odb) file, which needs to be opened in Abaqus CAE. Since the fiber orientation distribution is stored as a state variable (cf. Section 4.2.2), the Eulerian part instance and the Eulerian volume fraction (EVF) Section need to be chosen. These inputs enable an internal access to the corresponding state variables within Abaqus CAE. Due to the parallel computing, the element numbering provided by Abaqus is not in accordance with the VTK convention. Therefore, a renumbering of the elements is done to ensure a valid output. The generated VTK file is also using the tensor notation of the fiber orientation results.

To enable an easy generation of the VTK file from the CEL process simulation results, the Export CEL Results GUI from the *Fibermap* Plug-in can be used. This GUI provides all available jobs, steps, instances and Eulerian Sections within separate dropdown menus to avoid wrong input to the export script (see Figure 5-4).

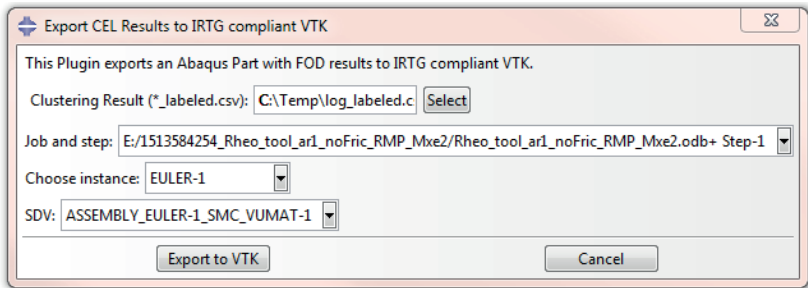


Figure 5-4: GUI of the VTK converter for the process simulation with Abaqus CEL

Beside the processing of Abaqus CEL results, it is also possible to convert results from Moldflow. Therefore, the patran file and the element based result information need to be exported from Moldflow. These two files can then be converted to a VTK-file within the *Fibermap* Plugin.

5.2. Mapping of process simulation results

In the most cases, the structural simulation uses a different mesh than the process simulation. Therefore, the information needs to be mapped from the one to the other mesh. This is done by mapping tools. Within the CAE chain, the mapping is done by using MapLib, which is part of the MpCCI Multi-Physics Software Solutions provided by the Fraunhofer Institute for Algorithms and Scientific Computing (SCAI). This script-based tool needs two VTK files, the source mesh with the result information and the target mesh. While the VTK file with the result information is generated by the *export results* scripts, the target mesh VTK file needs to be generated separately. If the target mesh is available within Abaqus, the *Fibermap* Plug-in offers an exporting tool (see Figure 5-5). By choosing the desired part in an opened model, the VTK file of the target mesh is generated, with the correct element and node order convention.

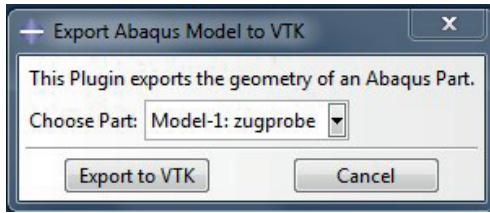


Figure 5-5: GUI of the export script for the structural simulation mesh

Beside the two VTK meshes, the MapLib mapper needs a configuration input. Within this configuration file, the mapping algorithms as well as the neighborhood search options are defined. These options have a significant effect on the mapping quality and need to be chosen depending on the structural mesh type (solid or shell), see below. All inputs can be passed to the mapping tool by the Mapping GUI (see Figure 5-6). As a result, a new VTK file based on the structural target mesh input with the mapped information from the source mesh is generated.

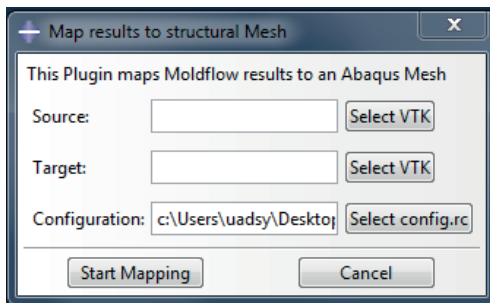


Figure 5-6: GUI for the input of the MpCCI MapLib mapping tool

To identify the best mapping algorithm, a generic study with finer and rougher target meshes is performed. An exemplary mapping result of this study from a solid 4 x 4 to a solid 5 x 5 mesh is shown Table 5-1. The five avail-

able algorithms for solid target meshes show slight differences near the transition zone of the two different fiber orientations of the original mesh. The element-based and the node-based results are slightly different since the fiber orientations information are element based with one integration point. Therefore, the node-based information is averaged. This averaging could lead to some inhomogeneities for some mapping algorithms. The Weighted Element formulation is especially developed for the usage in a CAE-chain with element based information [Mag16]. This approach is using the geometrical element information and weights them depending on the volume content. Due to this fact, the results are not continuous and therefore closer to the original mesh information. All other mapping algorithms are using a node based mapping, which leads to an initial deviation due to the averaging. Therefore, together with the other results of the study, the “Weighted Element” algorithm turned out to be the best. For further information regarding the different algorithms and their neighborhood search options it is referred to the MpCCI MapLib manual [Spi12].

Table 5-1: Comparison of the different mapping algorithms from a solid 4 x 4 to a solid 5 x 5 mesh based on the first component (A_{11}) of the fiber orientation tensor

	Element	Node
Original mesh		
Shape Function		
Shape Function		
Flux		
Weighted Element		

5.3. Linear elastic homogenization with anisotropic material cards

The import of the mapped result information and the homogenization is divided into two separate scripts to enable different homogenization methods within the *Fibermap* Plug-in. In the first step the import and the clustering are performed. This clustering prevents the generation of one material card for every single element. Due to this clustering, similar fiber orientations are conflated in one group. To ensure the correct orientation of the global fiber orientation, a material orientation is assigned for every element. The clustering uses the eigenvalues (a_1, a_2, a_3) of the fiber orientation tensor to find similar material properties, as the fiber orientation tensor can be expressed in its eigenvector coordinate system as:

$$\mathbf{A} = \begin{pmatrix} A_{11} & A_{12} & A_{13} \\ \text{sym} & A_{22} & A_{23} \\ & & A_{33} \end{pmatrix}_{e_x, e_y, e_z} = \begin{pmatrix} a_1 & 0 & 0 \\ \text{sym} & a_2 & 0 \\ & & a_3 \end{pmatrix}_{\bar{e}_1, \bar{e}_2, \bar{e}_3}. \quad (63)$$

Due to the convention that the sum of the eigenvalues must be equal to one and the sequence of $a_1 \geq a_2 \geq a_3$, the following limits can be distinguished:

$$\mathbf{a}_{iso} = \begin{pmatrix} 0.333 \\ 0.333 \\ 0.333 \end{pmatrix}, \quad \mathbf{a}_{planar} = \begin{pmatrix} 0.5 \\ 0.5 \\ 0 \end{pmatrix}, \quad \mathbf{a}_{uni} = \begin{pmatrix} 1 \\ 0 \\ 0 \end{pmatrix}. \quad (64)$$

Due to these limits, the possible eigenvalue space can be reduced to the triangle plotted in Figure 5-7. The K-Means method is very well suited for grouping point sets of this magnitude. The aim of this method is to solve the following optimization task:

$$\text{Min} \left(\sum_{c=1}^C \sum_{n_i \in C_c} \|n_i - \mu_c\|^2 \right). \quad (65)$$

In this equation, C is the desired number of clusters, C_c the set of points in the c -th cluster and the μ_c the midpoint of the c -th cluster. An algorithm to solve this problem is the so-called Lloyd's algorithm, which is implemented in

the Python library SciPy. Due to the Abaqus CAE implementation, this cannot be used within Abaqus. Therefore, a log file is used to solve this problem in an external program and to call the results from the list.

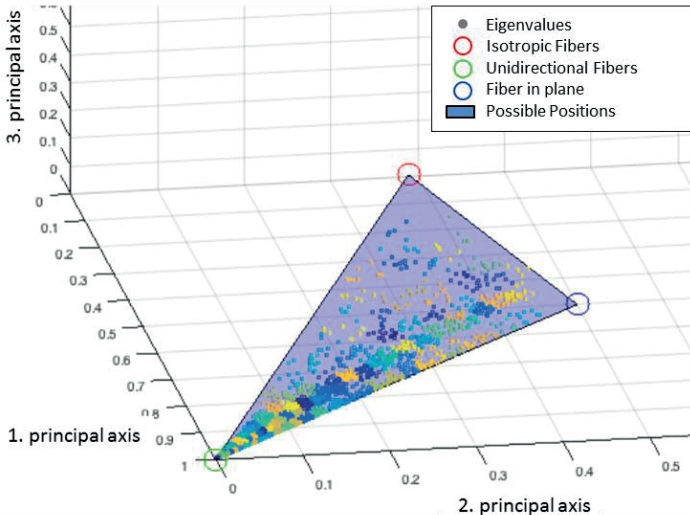


Figure 5-7: Clustering of material properties based on the eigenvalues of the fiber orientation tensor. Nodes in the same clusters have the same color. [Mey16]

All necessary input can be passed to the clustering script by using the GUI (see Figure 5-8). Within this GUI, the mapped result VTK file and the corresponding target part need to be selected. If a region of the target part should be omitted, the reserved element sets option could be used. This could be relevant, if the part consists of multiple Sections or part instances with different materials.

The number of the clusters can be defined in the dropdown menu of the “Desired Number of Materials”. To ensure the accuracy as well as an acceptable computation time, 30, 100 or 200 clusters can be selected. If more than 200

clusters are used, the preprocessing is slowed down and the amount of required memory during the simulation is increasing.

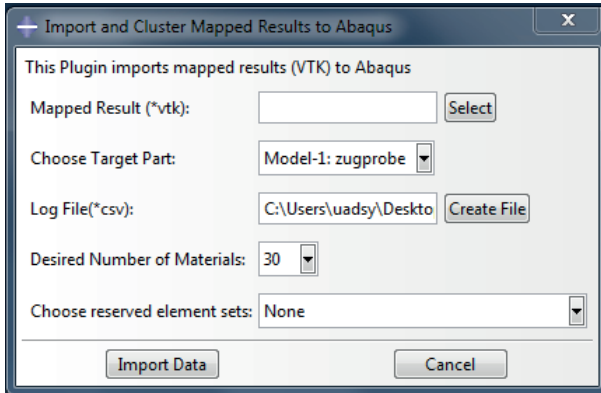


Figure 5-8: GUI to import and cluster mapped results from a VTK file to Abaqus

After the material clustering, the homogenization is done. Therefore, different homogenization approaches for stiffness and thermal properties are available, which are all based on linear-elastic material properties of the fiber and the matrix.

For the stiffness homogenization, the Tandon-Weng approach is used to define the fourth order Eshelby tensor \mathbb{S} of unidirectional inclusions [Tan84]. This tensor describes the mechanical properties of a fiber-like spheroidal inclusion under equal strain. Starting with the same properties for the matrix and the inclusion, a unidirectional two phase formulation is described by Tandon and Weng [Tan84]. For the description of non-unidirectional composite materials, a tessellation over the hemisphere of possible fiber orientations is performed to generate an array of unidirectional anisotropic mechanical material properties. Within this approach, the fourth order fiber orientation tensor \mathbb{A} is required. Therefore, the IBOF closure approximation (cf. Section 2.4 and eq. 15) is used. To calculate the fourth order anisotropic stiffness matrix \mathbb{C}

based the tessellated unidirectional stiffness properties the fiber orientation tensor, the averaging approach from Advani and Tucker [Adv87] is used.

The homogenization of the thermal properties follows the same process. For the generation of the unidirectional thermal properties, different methods depending on the used material system are available. The Laws approach [Law73] is based on a self-consistent theory and is developed for a multi-phase problem ($n > 2$) material and can describe anisotropic heterogeneous composites. When this approach is reduced to the two phases fiber and matrix, it is equal to the Rosen-Hashin method [Ros70], which is also available. Furthermore, the Scharpery method [Sch68] for mainly unidirectional and the Chamberlain [Cha68] approach for unidirectional transverse-isotropic composites is implemented.

The linear elastic material and the thermal properties of the fiber and the matrix can be inserted to the homogenization via the GUI (see Figure 5-9). Furthermore, the scalar fiber aspect ratio and the fiber volume content have to be defined. Due to the object-based script programming and the prepared dropdown menu, further stiffness or strength homogenization approaches can be implemented easily. Based on the settings during the clustering, this script generates the chosen amount of anisotropic material cards and assigns the corresponding material orientation to every element.

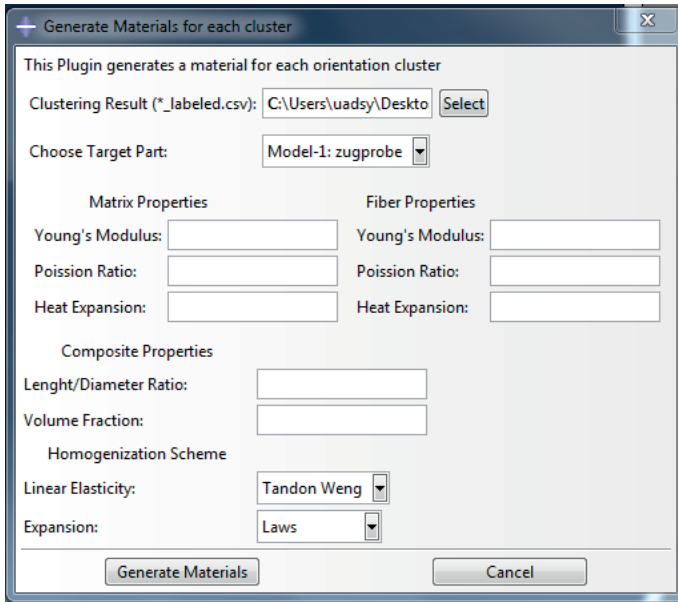


Figure 5-9: GUI to define the material properties of matrix and fiber to homogenize the long fiber composite based on the fiber orientation tensor

If results from structural simulations are used in further Abaqus simulations, the homogenized material properties can be exported into the VTK format. Therefore, the clustering result and the part instance can be selected in the export GUI (see Figure 5-10). This tool can also be used if Abaqus should not be used for the (thermo-) mechanical simulation.

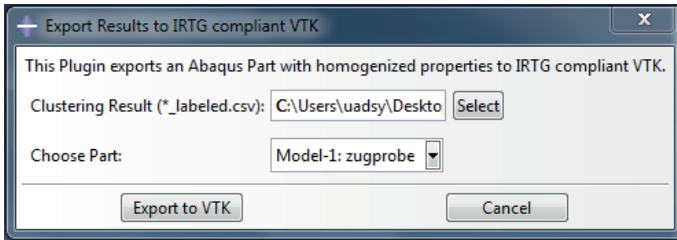


Figure 5-10: GUI to export homogenized material properties into the VTK format

5.4. Effects of the consideration of fiber orientation in the structural simulation

To show the effects of this CAE-chain, the results from the IRTG reference structure (cf. Section 4.3.2) are used. Therefore, two tension specimens are simulated, one with the mapped fiber orientation and the other with a homogeneous quasi-isotropic in-plane fiber orientation. The position of the tensile bar is given in Figure 5-11. Since the standard tensile specimen is slightly longer than the top surface of the beading, the clamping is considered isotropic where no mapped material is available.

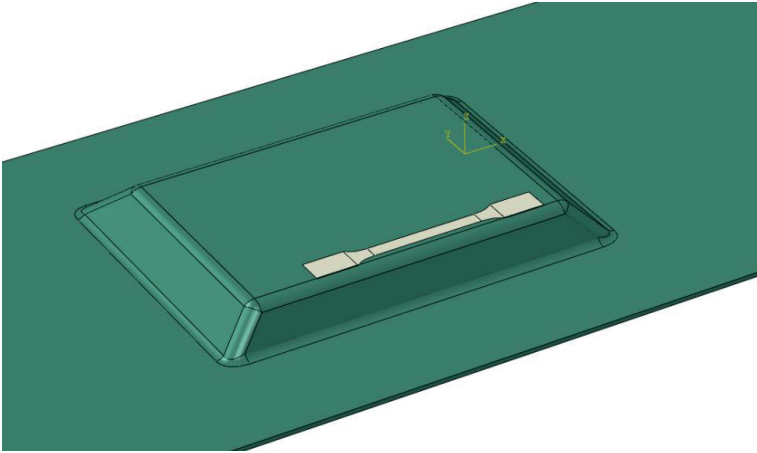


Figure 5-11: Position of the tensile bar in the IRTG reference structure

For the homogenization, 100 clusters are used. For both cases, the isotropic material properties given in Table 5-2 are used for the fibers and the resin. By assuming an averaged fiber diameter of 13 μm and a fiber length of 25 mm, the aspect ratio is approximately 2000. The fiber volume content is set to 40 %.

Table 5-2: Material data for the homogenization

	Glass Fiber	Resin
Young's Modulus [GPa]	73.0	3.1
Poisson's Ratio [-]	0.39	0.22

By using the stiffness homogenization tool from Section 5.3, the material cards and the corresponding element sets are generated. To model the 1D load to the tensile bar specimen, the surfaces of the left clamping area are

constraint in all directions, while the right areas are only constrained in y- and z-direction. To apply the load in x-direction, a surface shear load is applied (see Figure 5-12).

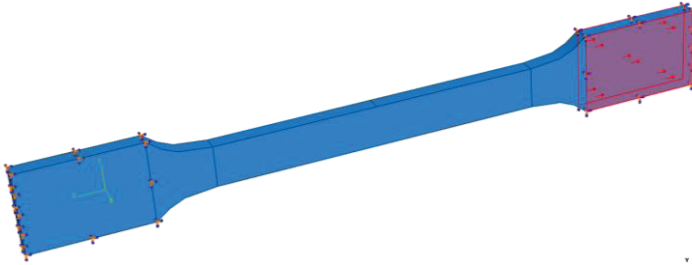


Figure 5-12: Boundary conditions and loads of the tensile bar specimen

The results of the structural simulation are shown in Figure 5-13 with the von Mises stress distribution and in Figure 5-14 with the displacement. By comparing the results from the mapped and the quasi-isotropic simulation, the mapped result shows slightly higher stress peaks and a slightly higher displacement. From this, it can be derived, that the average stiffness is lower compared to the quasi-isotropic sample. Furthermore, the mapped specimen shows non-symmetric local variations, resulting from the non-symmetric geometry of the IRTG reference structure. This leads to a non-symmetric stress and deformation distribution. As these variations occur also over the thickness, a small out of plane torsion is predicted.

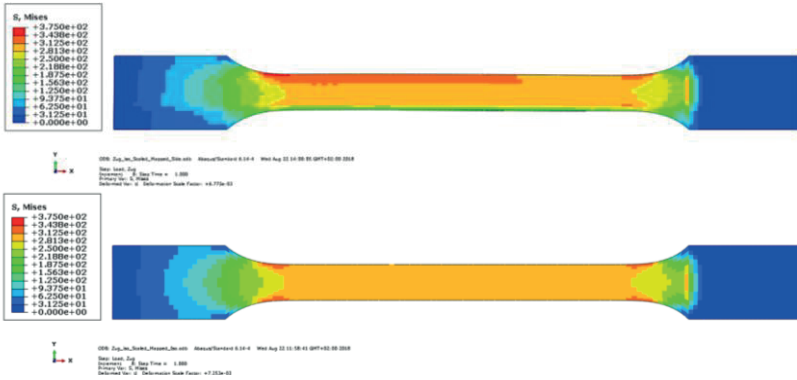


Figure 5-13: Von Mises stresses of the deformed tensile bars: mapped fiber orientation (top) and quasi-isotropic fiber orientation (bottom) from the IRTG reference structure

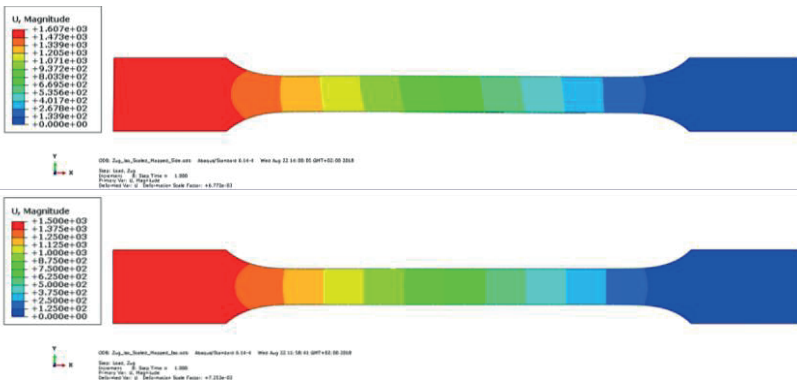


Figure 5-14: Displacement of the deformed tensile bars: mapped fiber orientation (top) and quasi-isotropic fiber orientation (bottom) from the IRTG reference structure

This simple example shows the need of the consideration of manufacturing effects from the process simulation in the (thermo-) mechanical simulation. Furthermore, these effects need to be considered within the CAE-chain (see Figure 5-1) to optimize the process parameters (e.g. position of the initial

charge or the mold closing speed) or the geometry of the part within a topology optimization.

5.5. Summary CAE Chain for long-fiber reinforced composites

The process chain with the combination of the compression molding simulation and the structural simulation was shown for Sheet Molding Compound. Since also results from Moldflow can be used within the *Fibermap* Plugin, the presented CAE chain is also applicable to injection molding of thermoplastic and thermoset materials, as well as for the compression molding of long-fiber reinforced thermoplastics.

By showing the different steps of the CAE chain with the export of results, converting to the neutral VTK-format, mapping, homogenization and structural simulation, the user-friendly application was proven. The comparison of a homogeneous distributed fiber orientation and the mapped results from the process simulation at a tensile specimen show the need of such a CAE chain, since the maximal displacement differs by 7%. Since the consideration of the manufacturing induced fiber orientations leads to more realistic results in the structural simulation, global safety factors can be reduced, which leads to a reduced part weight and can be therefore the key to increase the usage of SMC.

6. Conclusion

For the mass production of fiber-reinforced polymers with Class-A surfaces, Sheet Molding Compound (SMC) is an outstanding material due to its good price to stiffness ratio and its very outstanding price to weight ratio. Due to the high possible degree of automatization and very low amount of waste due to a high material utilization factor, SMC is widely used in the automotive and the commercial vehicle industry. Nevertheless, new developments of new SMC formulations with higher fiber volume contents and sometimes with carbon fibers extends the application area for SMC towards semi-structural parts [Hen17]. Due to these new applications, the holistic simulation of SMC parts becomes more important. Since commercial simulation tools are not suitable for the process simulation of SMC, new approaches need to be developed.

Up to now, no standard is set to characterize the flow behavior of SMC to gain the material parameter for the process simulation. The latest developments were using simple compression rheometer with two pressure sensors to measure the pressure difference along the flow length [Dum07] [Gui12]. With this approach, the resin-rich lubrication layer at the mold surface and the relatively cold core region can be characterized under conditions close to the real process. The disadvantage of this available rheological tool is that multiple molding trials are necessary for one characterization run. Due to the inhomogeneity of SMC, this can lead to avoidable, method induced deviations. To overcome this disadvantage, a new rheological tool with a long flow path and seven pressure sensors was developed in the present work to obtain more reliable material data. Simultaneously, all press data are recorded.

With this new rheological tool, four SMC materials were investigated. The first SMC material formulation is a typical Class-A SMC for exterior automotive parts. The second one is also a Class-A SMC formulation, where the replacement of a certain amount of fillers with micro hollow glass spheres led to a Low-Density Class-A SMC, developed by the Fraunhofer ICT. The third SMC

formulation is a semi-structural SMC, based on a Vinylester resin. This material has no fillers and an increased fiber volume content to carry higher loads in the final part. The fourth material is also a semi-structural SMC based on an Unsaturated Polyester Polyurethane Hybrid (UPPH) resin. This formulation contains no fillers and a further increased fiber volume content. To show the opportunities of the semi-structural SMC materials, this UPPH SMC was produced with glass and carbon fibers.

Due to the new design of the rheological tool and the characterization of different SMC material formulations, the appearance of material compressibility could be detected along the flow length. Since Guiraud [Gui12] showed the compressibility under isothermal conditions for room-tempered SMC with an external lubrication film, the compressibility could now be shown under real process conditions. By quantifying this material behavior, the compressibility could be proven for the semi-structural SMC formulations over a large process window of closing speeds (constant velocity and constant nominal deformation rate). Contrary to this, the standard Class-A SMC formulations with fillers show an incompressible behavior. By using an empirical formulation, the compressibility was fitted over the process range to consider it in the material characterization models. Based on this compressibility model, the characterization model developed by Dumont et al. [Dum07] was extended to suit these semi-structural SMC materials. By using this new compressible model, which can also be used for incompressible material formulations, all SMC formulations except the glass fiber UPPH SMC were characterized. In a next step, the material parameters are compared with each other and with the data from the literature. Based on these data, some regularities could be derived. So it emerged that the power-law coefficients of the models for the lubrication layer and the core region could be determined only depending on the material formulation. This reduces the characterization effort from four to two material parameters, which leads once again to a higher quality of the material data. Based on all this experience, this tool design with the corresponding compressible model has the potential to become a standard approach to characterize SMC materials for advanced simulation models.

Beside the material characterization for viscosity and compressibility, further new findings on material behavior could be made. Although the UPPH SMCs with glass and carbon fibers use the same resin, different flow behaviors were observed. While the carbon fiber UPPH SMC has a similar flow behavior like the other SMC formulations, the glass fiber UPPH SMC shows a different flow behavior. The standard SMC flow behavior is dominated by the thin resin-rich lubrication layer, which leads to an extensional deformation behavior in the core region. Since the pressure distribution of the glass fiber UPPH SMC with its pressure peaks at the flow front could not be described with such a flow behavior, optical evaluations and CT-scans were made to identify the reasons for the pressure peaks. Based on these evaluations, a probable flow model, which could describe this behavior, was developed. The basic idea of this model is that the lubrication layer consists of the outer sheet of the initial charge stack, which is flowing along the mold surface, while the core region is elongated only barely. This presented proposed flow model needs to be proven with further investigations. This is especially important since no fiber orientation could be predicted without a reliable flow model. This is one of the main issues when such a semi-structural SMC material is supposed to be used for automotive industry.

The process simulation of SMC is the second focus of this thesis. Up to now, most process simulation models use a 2.5D shell approach based on a Hele-Shaw model with a varying thickness over the molding process. These models consider the lubrication layer and the core region by superimposing different models for both regions. Since this approach has problems when it comes to junctions, e.g. at ribs, these models are not suitable for nowadays needs. Furthermore, new developments in the area of combining SMC with local unidirectional fiber reinforcements require 3D approaches with a full Fluid-Structure-Interaction. Therefore, commercial 3D SMC process simulation tools were compared with the experimental results. Even after a fitting of material parameter, these commercial tools were not able to predict the typical SMC pressure behavior with the high pressure increase at the flow front due to the

rheological stress which is followed by a threshold and the exponential pressure increase due to the hydrodynamic friction stress, while the material is flowing along the sensor. The differences between the experiments and the results from the commercial tool could be related to the used material models. The commercial tools are using the Castro-Macosko [Cas82] model, which originates from the thermoplastic compression molding models and accounts for shear viscosity only. Therefore, neither the lubrication layer at the mold surface, nor the resulting deformation rate depending elongational behavior can be predicted.

To overcome these disadvantages in the process simulation, a new approach based on the Abaqus Coupled-Eulerian-Lagrangian method was developed. This method offers a full Fluid-Structure-Interaction and can model large deformation due to the combination of the Eulerian and Lagrangian approach. To enable this method to simulate the compression molding process of SMC, a user material subroutine (VUMAT) was developed, which contains the stress updates and the fiber orientation models. To calculate the current stresses in each increment, a superposition of the rheological stresses and the hydrodynamic friction stresses is performed. Therefore, the 2.5D models are extended to full 3D ones. Additionally, a compression pressure due to the compression of the volume elements is considered. For the rheological stresses, a separate modelling of the extensional and shear viscosity is done, since the SMC needs to be considered as a Non-Newtonian compressible material. Therefore, the Trouton ratio [Tro1906] which couples the extensional and shear viscosity is not valid. For the extensional viscosity, a deformation rate depending power-law approach is extended by an Arrhenius function to consider the temperature dependent material behavior. For the shear viscosity, the state of art Castro-Macosko model is used. Since the lubrication layer is too thin to model it with a separate element layer within acceptable computational time, it is modeled with a friction model. Therefore, a slip condition at the tool surface is used to ensure the correct velocity field of the core region. Additionally, the hydrodynamic friction stresses are applied to the ele-

ments at the tool surface by using the velocity-dependent power-law approach, suggested by Abrams et al. [Abr03]. To describe the fiber reorientation during the compression molding simulation, the ARD-RSC model [Phe09a] is used. Within this model, a closure approximation to calculate the fourth order fiber orientation tensor out of the second order fiber orientation tensor is necessary. Therefore, the IBOF-closure [Chu02] is used, which is a compromise between accuracy and calculation time. Since not all necessary information are available within the VUMAT, several subroutines and scripts were written to pass all information from the initial configuration and the current time increment to the VUMAT.

To validate this new process simulation model, the rheological tool from the characterization experiments was used. With the simulations of the different SMC material formulation, the typical SMC pressure pattern with the initial pressure increase and the following threshold could be predicted. Nevertheless, these simulations revealed issues with the compressibility behavior of the SMC, which leads to errors in the simulation. Depending on the rheological stresses and due to the compressibility of the material, the material volume is locally reduced. Due to numerical oscillations, this compression can localize dramatically, which leads to an extreme element deformation. Since the compression pressure model is not part of this work and further investigations need to be done, this issue was not solved. Therefore, a new model for the compression pressure needs to be developed, which might replace the scalar bulk modulus with a tensor modulus to consider deformation rate or velocity dependencies. Since this issues with the compression pressure are amplified within this model due to the reduced degrees of freedom (only U1 and p), further tests with a 3D geometry were performed. Therefore, the reference structure from the International Research Training Group was used. This reference structure also contains local unidirectional reinforcements, which were considered in the simulation model. The simulation results show the capability of the new SMC-specific process simulation approach. While the SMC is flowing in the cavity, the displacement of the local reinforcements could be predicted due to the full Fluid-Structure-Interaction within the CEL

method. For this simulation, the local reinforcements were considered isotropic and homogeneous. For further works, a more realistic unidirectional tape model should be used to predict the deformation more realistic, especially if higher deformations are expected.

To use the results from the process simulation for further simulations, the third focus of this thesis is to establish a virtual CAE-chain to transfer information between the process and the structural simulation. Therefore, the script-based *Fibermap* tool was developed, which can export finite element models and results of the process simulation to the neutral VTK-format, map information between different meshes and homogenize the material stiffness based on the fiber orientation tensors. The mapping is done by using the mapping library MapLib, which is part of the MpCCI Multi-Physics Software Solutions provided by the Fraunhofer Institute for Algorithms and Scientific Computing (SCAI). MapLib is therefore integrated in the scripts for an easier usage. The stiffness homogenization step is divided into two sub-steps. In the first step, a clustering based on the fiber orientation tensors is done to avoid the creating of a material card for every element. By using the K-Means method, the possible fiber orientation tensors are clustered into 30, 100 or 200 groups, which makes the pre- and post-processing easier and reduces the initialization time for the solver. Based on these clusters, which have one center fiber orientation tensor each, the homogenization is done. Therefore, a two-step scheme is used by combining Tandon-Weng approach [Tan84] for the unidirectional homogenization with the fiber tensor based averaging proposed by Advani and Tucker [Adv87]. Here, once again, the IBOF closure is used to calculate the fourth order Eshelby tensor for the ellipsoid inclusion of the fiber in the matrix material. Besides the stiffness homogenization, also a thermal expansion coefficient homogenization can be performed. To do so, the same two-step approach is used, but different homogenization schemes for the unidirectional homogenization are used.

To show the effect of the CAE-chain, a comparison between the standard quasi-isotropic method and the mapped fiber orientation tensor dependent

material properties is performed. Therefore, the fiber orientation results of the IRTG reference structure are mapped onto a tensile bar. This simple example illustrates the differences due to a change of the elongation by 7%. By the consideration of the process simulation results with better material models, the structural simulation comes closer to the experimental results and therefore, global safety factors can be reduced. This can be one key to increase the usage of SMC in the automotive industry. To further improve the CAE-chain in the context of the automotive demands, homogenization of strength and damage evolution need to be developed and added to the *Fiber-map* tool.

Summarizing the three main focuses of this thesis, it could be shown that the reliable characterization, an SMC-specific process simulation model and the transfer of the results to the structural simulation, improves the prediction quality for the final SMC part. When neglecting one of these steps, the prediction quality will increase dramatically and part damages or too heavy parts are the result. Since both are knock-out criteria in the nowadays automotive development process, it is highly recommended to follow the presented process even while increasing the characterization effort and the computational time.

Nomenclature

Greek Symbols

α_1, α_2	fitting parameter of relative volume change model	[-]
α_g	gelation conversion	[-]
β	relative volume change	[s ⁻¹]
$\dot{\gamma}$	magnitude of the strain rate tensor	[-]
$\dot{\boldsymbol{\varepsilon}}$	strain rate tensor	[-]
$\dot{\varepsilon}_v$	volumetric strain rate	[-]
η	extensional viscosity	[Pa s]
η_{PS}	pure strain extensional viscosity	[Pa s]
κ	scalar reduction factor	[-]
λ	hydrodynamic friction coefficient	[N s m ⁻³]
ξ	ellipsoid particle shape function	[-]
ρ	density	[g cm ⁻³]
$\dot{\rho}$	time-related density derivative	[g cm ⁻³ s ⁻¹]
Σ_{33}	local thickness averaged axial stress	[Pa]
$\bar{\Sigma}^V$	thickness averaged in-plane viscous stress tensor	[Pa]
$\boldsymbol{\sigma}$	stress tensor	[Pa]

$\langle \sigma_{33} \rangle$	volumetric averaged axial stress	[Pa]
σ_{fric}	friction stress tensor	[Pa]
σ_{rheo}	rheological stress tensor	[Pa]
σ_{v}	viscous stress tensor	[Pa]
τ^*	fitting parameter of the Castro-Macosko viscosity model	[Pa]
ϕ	mapping function from the initial material point	[-]
$\hat{\phi}$	mapping function from the reference $\hat{\Omega}$ to the spatial domain Ω	[-]
x	motion of the material in the spatial domain Ω	[m s ⁻¹]
χ	initial values of the particle motions in the reference domain $\hat{\Omega}$	[m s ⁻¹]
Ψ	fiber orientation function	[-]
Ω	spatial domain	[-]
Ω_0	initial configuration in the material domain	[-]
$\hat{\Omega}$	reference domain	[-]

Latin Symbols

A	second order fiber orientation tensor	[-]
A_{11}, A_{22}, A_{33}	Fiber orientation in 1, 2 or 3	

	directions respectively	[-]
A_{int}	interaction area	[m ²]
\mathbb{A}	fourth order fiber orientation tensor	[-]
B	fitting parameter of the Castro-Macosko viscosity model	[kg m ⁻¹ s ⁻¹]
b	width	[m]
\mathbf{b}	Left-Cauchy-Green tensor	[-]
$b_1 - b_5$	fitting parameters of the ARD model	[-]
$\beta_1 - \beta_6$	fitting parameters of the IBOF closure approximation	[-]
C	number of clusters	[-]
\mathbf{C}	ARD fiber interaction tensor	[-]
C_1, C_2	fitting parameters of the Castro-Macosko viscosity model	[-]
\mathbf{D}	deformation rate tensor	[s ⁻¹]
D_0	reference deformation rate	[s ⁻¹]
D_c	compressibility change deformation rate	[s ⁻¹]
$\overline{\mathbf{D}}^{pl}$	symmetric plastic parts of the velocity gradient	[s ⁻¹]
d	diameter	[m]
\mathbf{F}	deformation gradient tensor	[-]
g	penetration length	[m]

H	rheological function according to Dumont et al. [Dum07]	[-]
\dot{h}	closing speed	[m s ⁻¹]
h	height	[m]
h_0	initial height of the IC stack	[m]
h_f	finale plate height	[m]
\mathbf{I}	identity matrix	[-]
K	bulk modulus	[Pa]
k	fitting parameter of relative volume change model	[-]
L	velocity gradient	[s ⁻¹]
\mathbb{L}	fourth order analytical functions of the eigenvalues of \mathbf{A}	[-]
l	length	[m]
l	fitting parameter of relative volume change model	[-]
l_0	initial length of the IC stack	[m]
l_{def}	reference length of relative volume change model	[m]
l_{max}	rheological tool length	[m]
l_{incomp}	incompressible flow front position	[m]
l_{sx}	position of sensor x in the rheological tool	[m]
\mathbb{M}	fourth order analytical functions eigenvectors of \mathbf{A}	[-]

m	friction power-law coefficient	[-]
n	rheological power-law coefficient	[-]
$\mathbf{n} / \vec{\mathbf{n}}$	surface normal vector	[-]
P	thickness averaged pressure	[Pa]
\mathbf{p}	fiber orientation vector	[-]
p	pressure	[Pa]
\mathbf{R}	body rotation matrix	[-]
\mathbf{R}^{el}	elastic part of the body rotation matrix	[-]
S	distribution function of the components in a fourth order Tensor	[-]
\mathbf{T}	arbitrary reaction terms of the stress tensor	[Pa]
T_0	reference temperature	[K]
T_b	fitting parameter of the Castro-Macosko viscosity model	[K]
t	time	[s]
\mathbf{U}	stretch tensor	[-]
v	velocity	[m s ⁻¹]
V	Volume	[m ³]
v_0	reference velocity	[m s ⁻¹]
\mathbf{W}	vorticity tensor/spin matrix	[s ⁻¹]

X_0	coordinates of the reference configuration	[m]
x_i, x_{i1}	evaluating length in flow direction	[m]
x_i	coordinates of the current configuration	[m]

Abbreviation

ALE	Arbitrary Lagrangian Eulerian
ar	aspect ratio
ARD	Anisotropic Rotary Diffusion
CEL	Coupled-Eulerian-Lagrangian
D-SMC	Direct-SMC
EVF	Eulerian volume fraction
FAST	Institute of Vehicle System Technology
FLD	field variable
IAM-WK	Institute for Applied Materials
IBOF	Invariant Based Optimal Fitting closure approximation
IC	initial charge
ICT	Fraunhofer Institute for Chemical Technology
IRTG	International Research Training Group
LD	Low density

ORW3	improved orthotropic fitted closure approximation for a wild range of interaction coefficient value
RSC	Reduced Strain Closure
SCAI	Fraunhofer Institute for Algorithms and Scientific Computing
SDF	Strain Reduction Factor
SDV	state variables
SMC	Sheet Molding Compound
UD	unidirectional
UP	Unsaturated Polyester
UPPH	unsaturated polyester polyurethane hybrid resin
VE	Vinylester
VUAMP	user defined amplitude subroutine
VUEOS	user defined equation of states
VUEXTERNAL	user defined external subroutine
VUFRICITION	user defined subroutine friction subroutine
VUINTERACTION	used defined interaction subroutine
VUSDFLD	user defined state variables and field subroutine
VUMAT	user defined material subroutine
VUVISCOSITY	user defined viscosity subroutine
wbk	Institute of Production Science

WLF	Williams-Landel-Ferry (model)
XFEM	Extended Finite Element Method

Table of Figures

Figure 2-1:	Composition of a typical Class-A SMC in wt.-% [Hoh15].....	8
Figure 2-2:	Principle of SMC production [Che16].....	9
Figure 2-3:	Process steps for the manufacture of SMC components with cutting, stacking, placing of the initial charge in the mold and the final part [Che16].....	11
Figure 2-4:	Experimental investigation of the flow behavior of SMC by using differently colored SMC sheets [Bar85].....	13
Figure 2-5:	Schematic illustration of the squeeze flow rheometer [Sil81].....	17
Figure 2-6:	Schematic illustration of the simple compression rheometer. To gain simple compression, the mold surfaces are lubricated [Dum03].....	18
Figure 2-7:	Schematic illustration of the plane strain/channel flow rheometer. To gain plane strain, a 1D flow is enforced [Dum03].....	19
Figure 2-8:	Schematic illustration of a spiral flow tool [Rab08].....	21
Figure 2-9:	Fiber orientation distribution and the corresponding reduced 2D second order fiber orientation tensor.....	24
Figure 2-10:	Maps between Lagrangian, Eulerian and ALE domain.....	29
Figure 2-11:	Comparison of the kinetic for an ALE formulation with Lagrangian and Eulerian description [Bel14].....	30
Figure 2-12:	Lagrangian and Eulerian Steps in the CEL approach [Ben04].....	31
Figure 2-13:	Definition of the penetration for pure and void elements [Ben04].....	32

Figure 3-1:	Position of the SMC initial charge and the pressure sensors along the lower mold part of the rheological tool [Hoh17a]	34
Figure 3-2:	Experimental setup for the rheological measurements....	35
Figure 3-3:	Exemplary pressure distribution of the standard Class-A SMC for a closing speed of $\dot{h} = 1 \text{ mm s}^{-1}$	38
Figure 3-4:	Exemplary pressure distribution of the LD Class-A SMC for a closing speed of $\dot{h} = 1 \text{ mm s}^{-1}$ [Hoh17b]	41
Figure 3-5:	Exemplary pressure distribution of the VE-SMC for a closing speed of $\dot{h} = 1 \text{ mm s}^{-1}$	44
Figure 3-6:	Exemplary pressure distribution of the UPPH glass fiber SMC for a closing speed of $\dot{h} = 1 \text{ mm s}^{-1}$	47
Figure 3-7	Emplary pressure distribution of the UPPH carbon fiber SMC for a closing speed of $\dot{h} = 1 \text{ mm s}^{-1}$ [Hoh17b]	49
Figure 3-8:	Compression molding experiments of the VE-SMC: pressure over relative gap height for (a) Sensor 1 and (b) Sensor 4 for different nominal deformation rates ($D = 0.5 \text{ s}^{-1}$, 1.0 s^{-1} and 2.0 s^{-1})	51
Figure 3-9:	Comparison of the relative volume change β of the VE-SMC between measurement and modelling for three nominal deformation rates $D = 0.5 \text{ s}^{-1}$, 1.0 s^{-1} and 2.0 s^{-1} during the molding process [Hoh17a].....	52
Figure 3-10:	Averaged relative volume change β from the Class-A SMCs experiments for a constant closing speed of $\dot{h} = 1 \text{ mm s}^{-1}$	54
Figure 3-11:	Relative volume change β from the experiments of the glass and carbon UPPH SMC for a nominal deformation rate of $D = 0.25 \text{ s}^{-1}$	55
Figure 3-12:	Fitting of the viscosity power-law exponent n with the results for the constant closing speed ($\dot{h} = 1 \text{ mm s}^{-1}$) of	

	the Class-A, LD Class-A SMC and the LD Class-A SMC paste	62
Figure 3-13:	Fitting of the viscosity power-law exponent n with the results for the constant nominal deformation rates ($D = 0.5 \text{ s}^{-1}$, 1.0 s^{-1} and 2.0 s^{-1}) and the constant closing speed ($h = 1 \text{ mm s}^{-1}$) of the VE-SMC formulation [Hoh17a].....	63
Figure 3-14:	Progression of the hydrodynamic friction coefficient λ over time and location for the UPPH carbon fiber SMC and a constant closing speed of $h = 1 \text{ mm s}^{-1}$ [Hoh17b]....	65
Figure 3-15:	Fitting of the viscosity power-law exponent n with the results for the constant nominal deformation rates ($D = 0.25 \text{ s}^{-1}$) and the constant closing speed ($h = 1 \text{ mm s}^{-1}$) of the UPPH C-SMC formulation	66
Figure 3-16:	Relative change of the extensional viscosity and hydrodynamic friction between the initial charge area and the flow area of the UPPH carbon fiber SMC [Hoh17b]	68
Figure 3-17:	Comparison of the fiber bundle structure in the glass fiber reinforced VE SMC (left) and the UPPH carbon fiber SMC (right).....	68
Figure 3-18:	Gray-scale picture with high contrast of a UPPH glass fiber SMC short shot and CT Sample positions	71
Figure 3-19:	Length of the vortex area at the flow front: optical measured and extracted from pressure distribution	72
Figure 3-20:	Micro tomography scan with color-coding of the fiber orientation direction of the flow front (sample 1): view on top of the sample (left) and sliced in the middle (right).....	73
Figure 3-21:	Micro tomography scan with color-coding of the fiber orientation direction of the sample from the center	

	region (sample 2): view on top of the sample (left) and sliced in the middle (right).	73
Figure 3-22:	Schematically cross-Section of SMC material during the molding process.....	75
Figure 3-23:	Schematically cross-Section of the probable flow of glass fiber UPPH SMC during the molding process	76
Figure 4-1:	Compression molding model with Moldflow, green: final cavity; red: initial charge position; black points: sensor positions	80
Figure 4-2:	Comparison between the pressure distribution from the experiments (black) and the commercial simulation tool based on the fitted reactive viscosity model (grey) ...	81
Figure 4-3:	Alignment of the fiber orientations predicted by the commercial simulation tool by starting with a quasi-isotropic fiber orientation distribution in the initial charge: top: Top surface view middle: Cutting surface in the middle plane bottom: bottom surface view	82
Figure 4-4:	Comparison between the fiber orientation distribution from the simulation and CT-scans (from [Bry14]): CT-Position 1 at x = 339 mm, y = 200 mm (top) and CT-Position 2 at x = 431 mm, y = 200 mm (bottom)	84
Figure 4-5:	Shear rate (top) and velocity in flow direction (bottom) at the flow front during the compression molding simulation with the commercial simulation tool	85
Figure 4-6:	Progression of the Young's modulus over the plate length in and perpendicular to the flow direction (data from Mrkonjic et al. [Mrk15])	86
Figure 4-7:	Polar decomposition of deformation gradient tensor F ...	90
Figure 4-8:	Schematic illustration of the order and interaction of scripts (dark blue), subroutines (green) and internal information (black) of the SMC process simulation	95

Figure 4-9:	Initialization Plug-in interface to initialize the geometrical information for the lubrication layer detection	96
Figure 4-10:	GUI to initialize the fiber orientation tensor for predefined element sets of the initial charge	97
Figure 4-11:	Evaluation of the penetration of the SMC through the mold surface depending on the bulk viscosity parameter: reduced (top), original (middle) and increased parameter set (bottom)	102
Figure 4-12:	Boundary conditions of the Lagrangian Elements for the rheological tool CEL model with the initial charge (beige) configuration of the semi-structural SMCs	105
Figure 4-13:	Local density change within the Castro-Macosko model with the 2-Domain-Tait model	107
Figure 4-14:	Results of a test mold filling simulation during the development process	108
Figure 4-15:	Rheological, friction and compression pressure stress for a VE-SMC material formulation at sensor position 1 and 2	109
Figure 4-16:	Evaluation of the flow front with the compression stresses at $t = 0$ s (top), $t = 0.375$ s (middle) and $t = 0.75$ s (bottom)	110
Figure 4-17:	Simulated stress distribution for Sensor 1 to 3 for the Class-A-SMC material	112
Figure 4-18:	Simulated stress distribution for Sensor 1 to 3 for the VE-SMC material	112
Figure 4-19:	Simulated stress distribution for Sensor 1 to 3 for the carbon UPPH-SMC material	113

Figure 4-20: Comparison of the compressibility ($\det(F)$, see eq. 60) of the carbon UPPH SMC (top) and VE SMC (bottom) after 0.025 s simulation time 114

Figure 4-21: Comparison of the displacement in flow direction (U_1) of the carbon UPPH SMC (top) and VE SMC (bottom) after 0.025 s simulation time 115

Figure 4-22: Comparison of the simulation results with the experiments of the Class-A material formulation 116

Figure 4-23: IRTG reference structure with the position of the local reinforcements (green) 118

Figure 4-24: Initial configuration of the process simulation of the IRTG reference structure with the local unidirectional reinforcements (green) and the initial charge (beige) 119

Figure 4-25: Blocking of the Eulerian mesh of the IRTG reference structure 120

Figure 4-26: Photos of the molded reference structure with local reinforcements with no deformation of the tapes (top) and slide deformation at the end of the tapes (bottom) [But17] 122

Figure 4-27: Displacement of the tapes during the compression molding process in flow direction 123

Figure 4-28: Displacement of the tapes during the compression molding process in-plane perpendicular to the flow direction 124

Figure 4-29: Displacement of the tapes during the compression molding process in compression direction (bottom) 125

Figure 4-30: Pressure of the SMC under the lower patch due to the patch deformation 125

Figure 5-1: Steps of the CAE-Chain at KIT-FAST [Hoh16b] 128

Figure 5-2:	GUI selection tree of the Fibermap plug-in within Abaqus	129
Figure 5-3:	GUI of the VTK converter for the process simulation with Moldflow	130
Figure 5-4:	GUI of the VTK converter for the process simulation with Abaqus CEL.....	131
Figure 5-5:	GUI of the export script for the structural simulation mesh	132
Figure 5-6:	GUI for the input of the MpCCI MapLib mapping tool	132
Figure 5-7:	Clustering of material properties based on the eigenvalues of the fiber orientation tensor. Nodes in the same clusters have the same color. [Mey16]	136
Figure 5-8:	GUI to import and cluster mapped results from a VTK file to Abaqus	137
Figure 5-9:	GUI to define the material properties of matrix and fiber to homogenize the long fiber composite based on the fiber orientation tensor	139
Figure 5-10:	GUI to export homogenized material properties into the VTK format	140
Figure 5-11:	Position of the tensile bar in the IRTG reference structure.....	141
Figure 5-12:	Boundary conditions and loads of the tensile bar specimen	142
Figure 5-13:	Von Mises stresses of the deformed tensile bars: mapped fiber orientation (top) and quasi-isotropic fiber orientation (bottom) from the IRTG reference structure.....	143
Figure 5-14:	Displacement of the deformed tensile bars: mapped fiber orientation (top) and quasi-isotropic fiber orientation (bottom) from the IRTG reference structure.....	143

List of Tables

Table 3-1:	Composition of the paste of the Class-A SMC.....	37
Table 3-2:	Composition of the paste of the Low-Density Class-A SMC [Kec16]	40
Table 3-3:	Composition of the paste of the semi-structural VE SMC	42
Table 3-4:	Press settings of the VE-SMC molding trials [Hoh17a].....	44
Table 3-5:	Composition of the paste of the semi-structural UPPH SMC	46
Table 3-6:	Comparison of rheological material data for a closing speed of $h = 1 \text{ mm s}^{-1}$ (comp. [Hoh17b])	70
Table 5-1:	Comparison of the different mapping algorithms from a solid 4 x 4 to a solid 5 x 5 mesh based on the first component (A_{11}) of the fiber orientation tensor.....	134
Table 5-2:	Material data for the homogenization	141

References

- [Abr00] Abrams, L. M.; Castro, J. M.: Practical guidelines for predicting steady state cure time during sheet molding compound (SMC) compression molding. In *Polymer Composites*, 2000, 21; pp. 931–940.
- [Abr03] Abrams, L. M.; Castro, J. M.: Predicting molding forces during sheet molding compound (SMC) compression molding. I: Model development. In *Polymer Composites*, 2003, 24; pp. 291–303.
- [Adv87] Advani, S. G.; Tucker, C. L.: The Use of Tensors to Describe and Predict Fiber Orientation in Short Fiber Composites. In *Journal of Rheology*, 1987, 31; pp. 751–784.
- [Adv90a] Advani, S. G.; Tucker, C. L.: Closure approximations for three-dimensional structure tensors. In *Journal of Rheology*, 1990, 34; pp. 367–386.
- [Adv90b] Advani, S. G.; Tucker, C. L.: A numerical simulation of short fiber orientation in compression molding. In *Polymer Composites*, 1990, 11; pp. 164–173.
- [Åke00] Åkermo, M.; Åström, B. T.: Modelling component cost in compression moulding of thermoplastic composite and sandwich components. In *Composites Part A: Applied Science and Manufacturing*, 2000, 31; pp. 319–333.
- [AVK13] AVK-. Industrievereinigung Verstärkte Kunststoffe eV.K. Ed.: *Handbuch Faserverbundkunststoffe/Composites. Grundlagen, Verarbeitung, Anwendungen*. Springer Fachmedien Wiesbaden, Wiesbaden, 2013.

- [Bae] von Baeyer: Handbuch der Physik. Herausgegeben von H. Geiger und K. Scheel. Band X. Verlag J. Springer, Berlin 1926. In Zeitschrift für Angewandte Chemie, 1926, 39; p. 1134.
- [Bar00] Barnes, H. A.: A handbook of elementary rheology. Univ. of Wales Institute of Non-Newtonian Fluid Mechanics, Aberystwyth, 2000.
- [Bar79] Barone, M. R.; Caulk, D. A.: The effect of deformation and thermoset cure on heat conduction in a chopped-fiber reinforced polyester during compression molding. In International Journal of Heat and Mass Transfer, 1979, 22; pp. 1021–1032.
- [Bar85] Barone, M. R.; Caulk, D. A.: Kinematics of flow in sheet molding compounds. In Polymer Composites, 1985, 6; pp. 105–109.
- [Bar86] Barone, M. R.; Caulk, D. A.: A Model for the Flow of a Chopped Fiber Reinforced Polymer Compound in Compression Molding. In Journal of Applied Mechanics, 1986, 53; p. 361.
- [Bar87] Barone, M. R.; Osswald, T. A.: Boundary integral equations for analyzing the flow of a chopped fiber reinforced polymer compound in compression molding. In Journal of Non-Newtonian Fluid Mechanics, 1987, 26; pp. 185–206.
- [Bar88] Barone, M. R.; Osswald, T. A.: A boundary element analysis of flow in sheet molding compound. In Polymer Composites, 1988, 9; pp. 158–164.
- [Bel14] Belytschko, T.: Nonlinear finite elements for continua and structures. Wiley, Chichester, 2014.
- [Bel78a] Belytschko, T. B.; Kennedy, J. M.: Computer models for subassembly simulation. In Nuclear Engineering and Design, 1978, 49; pp. 17–38.

- [Bel78b] Belytschko, T.; Kennedy, J. M.; Schoeberle, D. F.: QUASI-EULERIAN FINITE ELEMENT FORMULATION FOR FLUID-STRUCTURE INTERACTION. In American Society of Mechanical Engineers (Paper), 1978.
- [Ben04] Benson, D. J.; Okazawa, S.: Contact in a multi-material Eulerian finite element formulation. In Computer Methods in Applied Mechanics and Engineering, 2004, 193; pp. 4277–4298.
- [Ben89] Benson, D. J.: An efficient, accurate, simple ale method for nonlinear finite element programs. In Computer Methods in Applied Mechanics and Engineering, 1989, 72; pp. 305–350.
- [Ben92] Benson, D. J.: Computational methods in Lagrangian and Eulerian hydrocodes. In Computer Methods in Applied Mechanics and Engineering, 1992, 99; pp. 235–394.
- [Ber17] Bertóti, R.; Böhlke, T.: Flow-induced anisotropic viscosity in short FRPs. In Mechanics of Advanced Materials and Modern Processes, 2017, 3; p. 751.
- [Bry14] Brylka, B. et al.: Microstructure-based modeling of temperature-dependent stiffness of SMC, Bad Herrenalb, Germany, 2014.
- [Büc16] Bücheler, D.; Henning, F.: Hybrid resin improves position and alignment of continuously reinforced prepreg during compression co-molding with sheet molding compound. ECCM17 - 17th European Conference on Composite Materials, München, Germany, 2016.
- [Büc17] Bücheler, D.: Locally Continuous-fiber Reinforced Sheet Molding Compound. Doctoral Thesis, Karlsruhe, 2017.
- [But17] Butenko, V.: Internal communications. Documentation of the IRTG reference structure molding trials, Karlsruhe Institute of

- Technology (KIT) Institute of Product Engineering (IPEK), Karlsruhe, Germany, 2017, 2017.
- [Cas82] Castro, J. M.; Macosko, C. W.: Studies of mold filling and curing in the reaction injection molding process. In *AIChE Journal*, 1982, 28; pp. 250–260.
- [Cas89] Castro, J. M.; Griffith, R. M.: Sheet molding compound compression-molding flow. In *Polymer Engineering & Science*, 1989, 29; pp. 632–638.
- [Cas90] Castro, J. M.; Tomlinson, G.: Predicting molding forces in SMC compression molding. In *Polymer Engineering and Science*, 1990, 30; pp. 1568–1573.
- [Cha68] Chamberlain, N. J.: Derivation of expansion coefficients for a fibre reinforced composite. In *BAC Report SON(P)*, 1968; p. 33.
- [Che16] Cherif, C.: *Textile Materials for Lightweight Constructions*. Springer Berlin Heidelberg, Berlin, Heidelberg, 2016.
- [Chr97] Christensen, S. K. et al.: Fiber-matrix separation in ribbed SMC and BMC parts. In *Annual Technical Conference - ANTEC, Conference Proceedings*, 1997, 1.
- [Chu01] Chung, D. H.; Kwon, T. H.: Improved model of orthotropic closure approximation for flow induced fiber orientation. In *Polymer Composites*, 2001, 22; pp. 636–649.
- [Chu02] Chung, D. H.; Kwon, T. H.: Invariant-based optimal fitting closure approximation for the numerical prediction of flow-induced fiber orientation. In *Journal of Rheology*, 2002, 46; pp. 169–194.
- [Cin95] Cintra, J. S.; Tucker, C. L.: Orthotropic closure approximations for flow-induced fiber orientation. In *Journal of Rheology*, 1995, 39; pp. 1095–1122.

- [Com06] Comte, E. et al.: Void formation and transport during SMC manufacturing: Effect of the glass fiber sizing. In *Polymer Composites*, 2006, 27; pp. 289–298.
- [Doi81] Doi, M.: Molecular dynamics and rheological properties of concentrated solutions of rodlike polymers in isotropic and liquid crystalline phases. In *Journal of Polymer Science: Polymer Physics Edition*, 1981, 19; pp. 229–243.
- [Don04] Donea, J. et al.: *Arbitrary Lagrangian–Eulerian Methods: Encyclopedia of Computational Mechanics*. John Wiley & Sons, Ltd, 2004.
- [Dum03] Dumont, P. et al.: Anisotropic viscous behavior of sheet molding compounds (SMC) during compression molding. In *International Journal of Plasticity*, 2003, 19; pp. 625–646.
- [Dum07] Dumont, P. et al.: Compression moulding of SMC: In situ experiments, modelling and simulation. In *Composites Part A: Applied Science and Manufacturing*, 2007, 38; pp. 353–368.
- [Dum12] Dumont, P. et al.: Finite element implementation of a two-phase model for compression molding of composites. In *Revue Européenne des Éléments Finis*, 2012, 14; pp. 885–902.
- [Ein1906] Einstein, A.: Eine neue Bestimmung der Moleküldimensionen. In *Annalen der Physik*, 1906, 324; pp. 289–306.
- [Fer17] Ferré Sentis, D. et al.: 3D in situ observations of the compressibility and pore transport in Sheet Moulding Compounds during the early stages of compression moulding. In *Composites Part A: Applied Science and Manufacturing*, 2017, 92; pp. 51–61.
- [Fol84] Folgar, F.; Tucker, C. L.: Orientation Behavior of Fibers in Concentrated Suspensions. In *Journal of Reinforced Plastics and Composites*, 1984, 3; pp. 98–119.

- [Gib99] Gibson, A. G.; Toll, S.: Mechanics of the squeeze flow of planar fibre suspensions. In *Journal of Non-Newtonian Fluid Mechanics*, 1999, 82; pp. 1–24.
- [Gui10] Guiraud, O. et al.: Towards the simulation of mould filling with polymer composites reinforced with mineral fillers and short fibres. In *International Journal of Material Forming*, 2010, 3; pp. 1313–1326.
- [Gui12] Guiraud, O. et al.: Rheometry of compression moulded fibre-reinforced polymer composites: Rheology, compressibility, and friction forces with mould surfaces. In *Composites Part A: Applied Science and Manufacturing*, 2012, 43; pp. 2107–2119.
- [Han62] Hand, G. L.: A theory of anisotropic fluids. In *Journal of Fluid Mechanics*, 1962, 13; p. 33.
- [Hen17] Henning, F. et al.: Expanding Applications Areas for Sheet Molding Compound (SMC) Through New Material Compositions and New Hybrid Processes, Cancún, Mexico, 10th-14th 2017.
- [Hie80] Hieber, C. A.; Shen, S. F.: A finite-element/finite-difference simulation of the injection-molding filling process. In *Journal of Non-Newtonian Fluid Mechanics*, 1980, 7; pp. 1–32.
- [Hir74] Hirt, C.W.; Amsden, A.A.; Cook, J.L.: An arbitrary Lagrangian-Eulerian computing method for all flow speeds. In *Journal of Computational Physics*, 1974, 14; pp. 227–253.
- [Hoh15] Hohberg, M.: Process simulation of hybrid SMC structures with local continuous fiber reinforcements, Frankfurt, 2015.
- [Hoh16a] Hohberg, M.; Baumgärtner, S.: Parameter Study on the Rib Filling Pattern of LFT in Combination with UD-Tapes, Frankfurt, Germany, 2016.

- [Hoh16b] Hohberg, M. et al.: Process Simulation of Sheet Molding Compound (SMC) as key for the integrated Simulation Chain. In (NAFEMS Ed.): Simulation of Composites - Ready for Industry 4.0?, 2016; pp. 61–67.
- [Hoh17a] Hohberg, M. et al.: Rheological measurements and rheological shell model considering the compressible behavior of long fiber reinforced sheet molding compound (SMC). In Composites Part A: Applied Science and Manufacturing, 2017, 95; pp. 110–117.
- [Hoh17b] Hohberg, M. et al.: Rheological in-mold measurements and characterizations of Sheet-Molding-Compound (SMC) formulations with different constitution properties by using a compressible shell model. In Intern. Polymer Processing, 2017, XXXII; pp. 659–668.
- [Hoh17c] Hohberg, M. et al.: Comparison of the Flow and Rheological Behavior of Two Semi-Structural Sheet-Molding-Compound (SMC) Based on a Hybrid Resin and Glass or Carbon Fibers, Cancún, Mexico, 10th-14th 2017.
- [Hue88] Huerta, A.; Liu, W. K.: Viscous flow with large free surface motion. In Computer Methods in Applied Mechanics and Engineering, 1988, 69; pp. 277–324.
- [Hug81] Hughes, T. J.R.; Liu, W. K.; Zimmermann, T. K.: Lagrangian-Eulerian finite element formulation for incompressible viscous flows. In Computer Methods in Applied Mechanics and Engineering, 1981, 29; pp. 329–349.
- [Jac86] Jackson, W. C.; Advani, S. G.; Tucker, C. L.: Predicting the Orientation of Short Fibers in Thin Compression Moldings. In Journal of Composite Materials, 1986, 20; pp. 539–557.

- [Jef22] Jeffery, G. B.: The Motion of Ellipsoidal Particles Immersed in a Viscous Fluid. In *Proceedings of the Royal Society A: Mathematical, Physical and Engineering Sciences*, 1922, 102; pp. 161–179.
- [Kär15] Kärger, L. et al.: Development and validation of a CAE chain for unidirectional fibre reinforced composite components. In *Composite Structures*, 2015, 132; pp. 350–358.
- [Kec16] Keckl, C.: Einfluss der Eindickung von dichterem Sheet Moulding Compound auf die Formteilwelligkeit. Dissertation, KIT, 2016.
- [Ken84] Ken-Ichi, K.: Distribution of directional data and fabric tensors. In *International Journal of Engineering Science*, 1984, 22; pp. 149–164.
- [Kim92] Kim, J. et al.: Compression molding simulation of chopped fiber reinforced polymeric composites in plate-rib type geometry. In *Polymer Composites*, 1992, 13; pp. 97–107.
- [Kim97] Kim, K.-T.; Jeong, J.-H.; Im, Y.-T.: Effect of molding parameters on compression molded sheet molding compounds parts. In *Journal of Materials Processing Technology*, 1997, 67; pp. 105–111.
- [Kon15] Koniges, A. et al.: Multi-Material ALE with AMR for Modeling Hot Plasmas and Cold Fragmenting Materials. In *Plasma Science and Technology*, 2015, 17; pp. 117–128.
- [Kot98] Kotsikos, G.; Gibson, A. G.: Investigation of the squeeze flow behaviour of Sheet Moulding Compounds (SMC). In *Composites Part A: Applied Science and Manufacturing*, 1998, 29; pp. 1569–1577.
- [Kuh18] Kuhn, C. et al.: Simulative Prediction of Fiber-Matrix Separation in Rib Filling During Compression Molding Using a Direct

- Fiber Simulation. In *Journal of Composites Science*, 2018, 2; p. 2.
- [Law73] Laws, N.: On the thermostatics of composite materials. In *Journal of the Mechanics and Physics of Solids*, 1973, 21; pp. 9–17.
- [Lax60] Lax, P.; Wendroff, B.: Systems of conservation laws. In *Communications on Pure and Applied Mathematics*, 1960, 13; pp. 217–237.
- [Le 02] Le Corre, S. et al.: Shear and compression behaviour of sheet moulding compounds. In *Composites Science and Technology*, 2002, 62; pp. 571–577.
- [Le08] Le, T.-H. et al.: X-ray phase contrast microtomography for the analysis of the fibrous microstructure of SMC composites. In *Composites Part A: Applied Science and Manufacturing*, 2008, 39; pp. 91–103.
- [Lee81] Lee, L. J.; Marker, L. F.; Griffith, R. M.: The Rheology and Mold Flow of Polyester Sheet Molding Compound. In *Annual Technical Conference - Society of Plastics Engineers*, 1981.
- [Lee84] Lee, C.-C.; Folgar, F.; Tucker, C. L.: Simulation of Compression Molding for Fiber-Reinforced Thermosetting Polymers. In *Journal of Engineering for Industry*, 1984, 106; p. 114.
- [Lee87] Lee, C.-C.; Tucker, C. L.: Flow and heat transfer in compression mold filling. In *Journal of Non-Newtonian Fluid Mechanics*, 1987, 24; pp. 245–264.
- [Let96] Leterrier, Y.; G'Sell, C.: Multilayer plug flow modeling of the fast stamping process for a polypropylene/glass fiber composite. In *Polymer Composites*, 1996, 17; pp. 231–241.

- [Lin97] Lin, C.-M.; Weng, C.-I.; Ho, C.-T.: Anisotropy in sheet molding compounds during compression molding. In *Polymer Composites*, 1997, 18; pp. 613–622.
- [Lin99] Lin, C.-M.; Weng, C.-I.: Simulation of compression molding for sheet molding compound considering the anisotropic effect. In *Polymer Composites*, 1999, 20; pp. 98–113.
- [Lip88] Lipscomb, G. G. et al.: The flow of fiber suspensions in complex geometries. In *Journal of Non-Newtonian Fluid Mechanics*, 1988, 26; pp. 297–325.
- [Liu86] Liu, W. K.; Belytschko, T.; Chang, H.: An arbitrary lagrangian-eulerian finite element method for path-dependent materials. In *Computer Methods in Applied Mechanics and Engineering*, 1986, 58; pp. 227–245.
- [Liu91] Liu, W. K. et al.: Adaptive ALE finite elements with particular reference to external work rate on frictional interface. In *Computer Methods in Applied Mechanics and Engineering*, 1991, 93; pp. 189–216.
- [Mag16] Magagnato, D.: Charakterisierung und Simulation der Formfüllung beim Resin Transfer Molding unter Berücksichtigung der lokalen Faserstruktur. Dissertation, Karlsruhe, Germany, 2016.
- [Mar09] Marjavaara, B. D.; Ebermark, S.; Lundström, T. S.: Compression moulding simulations of SMC using a multiobjective surrogate-based inverse modeling approach. In *Mechanics of Composite Materials*, 2009, 45; p. 503.
- [Mar77] Marker, L. F.; Ford, B.: FLOW AND CURING BEHAVIOR EXHIBITED BY SMC DURING MOLDING. In *Modern Plastics*, 1977, 54; 64-66, 68 & 70.
- [Mey16] Meyer, N.: Documentation Fibermap, 2016.

- [Mic90] Michaeli, W. et al.: Simulation of the flow in SMC. In *Kunststoffe, German plastics*, 1990, 80; pp. 31–33.
- [Mrk15] Mrkonjić, M. et al.: Phenomenological Characterization and Macromechanical Modeling of Anisotropic, Non-linear Behavior of Sheet Molding Compounds (SMC), Karlsruhe, Germany, 2015.
- [Nic11] Nicolais, L.: *Wiley Encyclopedia of Composites*. John Wiley & Sons, Inc, Hoboken, NJ, USA, 2011.
- [Nic12] Nicolais, L.; Barzacchiello, A. Eds.: *Wiley Encyclopedia of Composites*, 2012.
- [Noh63] Noh, W. F.: CEL. A TIME-DEPENDENT, TWO-SPACE-DIMENSIONAL, COUPLED EULERIAN-LAGRANGE CODE, 1963.
- [Ode04] Odenberger, P. T.; Andersson, H. M.; Lundström, T. S.: Experimental flow-front visualisation in compression moulding of SMC. In *Composites Part A: Applied Science and Manufacturing*, 2004, 35; pp. 1125–1134.
- [Old04] Oldenbo, M. et al.: Global Stiffness of a SMC Panel Considering Process Induced Fiber Orientation. In *Journal of Reinforced Plastics and Composites*, 2004, 23; pp. 37–49.
- [Org06] Orgéas, L. et al.: Modelling the flow of power-law fluids through anisotropic porous media at low-pore Reynolds number. In *Chemical Engineering Science*, 2006, 61; pp. 4490–4502.
- [Org07] Orgéas, L. et al.: Upscaling the flow of generalised Newtonian fluids through anisotropic porous media. In *Journal of Non-Newtonian Fluid Mechanics*, 2007, 145; pp. 15–29.
- [Org12] Orgéas, L.; Dumont, P. J.J.: Sheet Molding Compounds. In (Nicolais, L.; Barzacchiello, A. Eds.): *Wiley Encyclopedia of Composites*, 2012.

- [Oss87] Osswald, T. A.: Numerical Methods for Compression Mold Filling Simulation. Ph. D. Thesis, Urbana-Champaign, USA, 1987.
- [Oss90] Osswald, T. A.; Tucker, C. L.: Compression Mold Filling Simulation for Non-Planar Parts. In *International Polymer Processing*, 1990, 5; pp. 79–87.
- [Oss94] Osswald, T. A.; Tseng, S.-C.: Compression Molding. In (Advani, S. G. Ed.): *Flow and rheology in polymer composites manufacturing*. Elsevier, Amsterdam, 1994; pp. 361–413.
- [Pér15] Pérez, C.; Ramírez, D.; Osswald, T. A.: Mechanistic model simulation of a compression molding process. Fiber orientation and fiber-matrix separation: Annual Technical Conference - ANTEC, Conference Proceedings, 2015; pp. 561–566.
- [Phe09a] Phelps, J. H.; Tucker, C. L.: An anisotropic rotary diffusion model for fiber orientation in short- and long-fiber thermoplastics. In *Journal of Non-Newtonian Fluid Mechanics*, 2009, 156; pp. 165–176.
- [Phe09b] Phelps, J. H.: Processing-microstructure models for short- and long-fiber thermoplastic composites, 2009.
- [Rab08] Rabinovich, M. et al.: Sheet molding compound characterization using spiral flow. In *Journal of Applied Polymer Science*, 2008, 109; pp. 2465–2471.
- [Ros70] Rosen, B.W.; Hashin, Z.: Effective thermal expansion coefficients and specific heats of composite materials. In *International Journal of Engineering Science*, 1970, 8; pp. 157–173.
- [Sai96] Saito, R.; Kan, W.-M. J.; James Lee, L.: Thickening behaviour and shrinkage control of low profile unsaturated polyester resins. In *Polymer*, 1996, 37; pp. 3567–3576.
- [Sch07] Schürmann, H.: *Konstruieren mit Faser-Kunststoff-Verbunden*. Springer-Verlag Berlin Heidelberg, Berlin Heidelberg, 2007.

- [Sch68] Schapery, R. A.: Thermal Expansion Coefficients of Composite Materials Based on Energy Principles. In *Journal of Composite Materials*, 1968, 2; pp. 380–404.
- [Sho14] Shokrieh, M. M.; Mosalmani, R.: Modeling of sheet molding compound compression molding under non-isothermal conditions. In *Journal of Reinforced Plastics and Composites*, 2014, 33; pp. 1183–1198.
- [Sil80] Silva-Nieto, R. J.; Fisher, B. C.; Birley, A. W.: Predicting mold flow for unsaturated polyester resin sheet molding compounds. In *Polymer Composites*, 1980, 1; pp. 14–23.
- [Sil81] Silva-Nieto, R.J.; Fisher, B.C.; Birley, A.W.: Rheological characterization of unsaturated polyester resin sheet molding compound. In *POLYMER ENGINEERING AND SCIENCE*, 1981, 21; pp. 499–506.
- [Spi12] Spiess, H.; Oeckerath, A.; Landvogt, B.: Mapping library manual version 2010.1, Fraunhofer SCAI, Sankt Augustin, 2012.
- [Tan84] Tandon, G. P.; Weng, G. J.: The effect of aspect ratio of inclusions on the elastic properties of unidirectionally aligned composites. In *Polymer Composites*, 1984, 5; pp. 327–333.
- [Tro1906] Trouton, F. T.: On the Coefficient of Viscous Traction and Its Relation to that of Viscosity. In *Proceedings of the Royal Society A: Mathematical, Physical and Engineering Sciences*, 1906, 77; pp. 426–440.
- [Tsi09] Tsigkopoulos, T. et al.: Consideration of elongation effects for both fiber reinforced and unfilled fluids by means of an invariant constitutive model. The Society of Rheology 81st Annual Meeting, Madison, Wisconsin, USA, 2009.

- [Twu93] Twu, J.-T. et al.: Numerical simulation of non-isothermal SMC (sheet molding compound) molding. In *Polymer Composites*, 1993, 14; pp. 503–514.
- [Van70] Vancso-Szmercsanyi, I.: Interaction between unsaturated polyester resins and metal oxides, [Zur Wechselwirkung zwischen ungesaetigten Polyesterharzen und Metalloxiden]. In *Kunststoffe*, 1970, 60; pp. 1066–1071.
- [Ver94] Verleye, V.; Couniot, A.; Dupret, F.: Numerical prediction of fiber orientation in complex composite injection-molded parts. In *American Society of Mechanical Engineers, Materials Division (Publication) MD*, 1994, 49.
- [Vit08] Vitali, E.; Benson, D. J.: Contact with friction in multi-material arbitrary Lagrangian-Eulerian formulations using X-FEM. In *International Journal for Numerical Methods in Engineering*, 2008, 76; pp. 893–921.
- [Wan08] Wang, J.; O’Gara, J. F.; Tucker, C. L.: An objective model for slow orientation kinetics in concentrated fiber suspensions: Theory and rheological evidence. In *Journal of Rheology*, 2008, 52; pp. 1179–1200.
- [Xu93] Xu, J. et al.: Compression molding of sheet molding compound in plate-rib type geometry. In *Polymer Composites*, 1993, 14; pp. 51–58.
- [Yad11] Yadali Jamaloei, B.; Kharrat, R.; Torabi, F.: A mechanistic analysis of viscous fingering in low-tension polymer flooding in heavy-oil reservoirs. In *Journal of Petroleum Science and Engineering*, 2011, 78; pp. 228–232.

Karlsruher Schriftenreihe Fahrzeugsystemtechnik (ISSN 1869-6058)

Herausgeber: FAST Institut für Fahrzeugsystemtechnik

- Band 1** Urs Wiesel
Hybrides Lenksystem zur Kraftstoffeinsparung im schweren Nutzfahrzeug. 2010
ISBN 978-3-86644-456-0
- Band 2** Andreas Huber
Ermittlung von prozessabhängigen Lastkollektiven eines hydrostatischen Fahrtriebsstrangs am Beispiel eines Teleskopladers. 2010
ISBN 978-3-86644-564-2
- Band 3** Maurice Bliesener
Optimierung der Betriebsführung mobiler Arbeitsmaschinen. Ansatz für ein Gesamtmaschinenmanagement. 2010
ISBN 978-3-86644-536-9
- Band 4** Manuel Boog
Steigerung der Verfügbarkeit mobiler Arbeitsmaschinen durch Betriebslastfassung und Fehleridentifikation an hydrostatischen Verdrängereinheiten. 2011
ISBN 978-3-86644-600-7
- Band 5** Christian Kraft
Gezielte Variation und Analyse des Fahrverhaltens von Kraftfahrzeugen mittels elektrischer Linearaktuatoren im Fahrwerksbereich. 2011
ISBN 978-3-86644-607-6
- Band 6** Lars Völker
Untersuchung des Kommunikationsintervalls bei der gekoppelten Simulation. 2011
ISBN 978-3-86644-611-3
- Band 7** 3. Fachtagung
Hybridantriebe für mobile Arbeitsmaschinen. 17. Februar 2011, Karlsruhe. 2011
ISBN 978-3-86644-599-4

- Band 8** Vladimir Iliev
Systemansatz zur anregungsunabhängigen Charakterisierung des Schwingungskomforts eines Fahrzeugs. 2011
ISBN 978-3-86644-681-6
- Band 9** Lars Lewandowitz
Markenspezifische Auswahl, Parametrierung und Gestaltung der Produktgruppe Fahrerassistenzsysteme. Ein methodisches Rahmenwerk. 2011
ISBN 978-3-86644-701-1
- Band 10** Phillip Thiebes
Hybridantriebe für mobile Arbeitsmaschinen. Grundlegende Erkenntnisse und Zusammenhänge, Vorstellung einer Methodik zur Unterstützung des Entwicklungsprozesses und deren Validierung am Beispiel einer Forstmaschine. 2012
ISBN 978-3-86644-808-7
- Band 11** Martin Gießler
Mechanismen der Kraftübertragung des Reifens auf Schnee und Eis. 2012
ISBN 978-3-86644-806-3
- Band 12** Daniel Pies
Reifenungleichförmigkeitserregter Schwingungskomfort – Quantifizierung und Bewertung komfortrelevanter Fahrzeugschwingungen. 2012
ISBN 978-3-86644-825-4
- Band 13** Daniel Weber
Untersuchung des Potenzials einer Brems-Ausweich-Assistenz. 2012
ISBN 978-3-86644-864-3
- Band 14** **7. Kolloquium Mobilhydraulik. 27./28. September 2012 in Karlsruhe.** 2012
ISBN 978-3-86644-881-0
- Band 15** 4. Fachtagung
Hybridantriebe für mobile Arbeitsmaschinen 20. Februar 2013, Karlsruhe. 2013
ISBN 978-3-86644-970-1
- Band 16** Hans-Joachim Unrau
Der Einfluss der Fahrbahnoberflächenkrümmung auf den Rollwiderstand, die Cornering Stiffness und die Aligning Stiffness von Pkw-Reifen. 2013
ISBN 978-3-86644-983-1

- Band 17** Xi Zhang
Untersuchung und Entwicklung verschiedener Spurführungsansätze für Offroad-Fahrzeuge mit Deichselverbindung. Nicht erschienen
ISBN 978-3-7315-0005-6
- Band 18** Stefanie Grollius
Analyse des gekoppelten Systems Reifen-Hohlraum-Rad-Radführung im Rollzustand und Entwicklung eines Rollgeräuschmodells. 2013
ISBN 978-3-7315-0029-2
- Band 19** Tobias Radke
Energieoptimale Längsführung von Kraftfahrzeugen durch Einsatz vorausschauender Fahrstrategien. 2013
ISBN 978-3-7315-0069-8
- Band 20** David Gutjahr
Objektive Bewertung querdynamischer Reifeneigenschaften im Gesamtfahrzeugversuch. 2014
ISBN 978-3-7315-0153-4
- Band 21** Neli Ovcharova
Methodik zur Nutzenanalyse und Optimierung sicherheitsrelevanter Fahrerassistenzsysteme. 2014
ISBN 978-3-7315-0176-3
- Band 22** Marcus Geimer, Christian Pohlandt
Grundlagen mobiler Arbeitsmaschinen. 2014
ISBN 978-3-7315-0188-6
- Band 23** Timo Kautzmann
Die mobile Arbeitsmaschine als komplexes System. 2014
ISBN 978-3-7315-0187-9
- Band 24** Roman Weidemann
Analyse der mechanischen Randbedingungen zur Adaption der oszillierenden Hinterschneidtechnik an einen Mobilbagger. 2014
ISBN 978-3-7315-0193-0
- Band 25** Yunfan Wei
Spurführungsregelung eines aktiv gelenkten Radpaars für Straßenbahnen. 2014
ISBN 978-3-7315-0232-6

- Band 26** David Schmitz
Entwurf eines fehlertoleranten Lenkventils für Steer-by-Wire Anwendungen bei Traktoren. 2014
ISBN 978-3-7315-0264-7
- Band 27** Christian Schwab
Beitrag zu einer universellen Baggerschnittstelle zur Übertragung elektrischer und hydraulischer Leistung sowie elektronischer Signale für komplexe Anbaugeräte. 2014
ISBN 978-3-7315-0281-4
- Band 28** Peter Dengler
Untersuchung zum effizienten Betrieb von Hydraulikzylindern in Konstantdrucksystemen unter Verwendung einer Zwischendruckleitung. 2015
ISBN 978-3-7315-0295-1
- Band 29** Manuel Bös
Untersuchung und Optimierung der Fahrkomfort- und Fahrdynamikeigenschaften von Radladern unter Berücksichtigung der prozessspezifischen Randbedingungen. 2015
ISBN 978-3-7315-0310-1
- Band 30** 5. Fachtagung
Hybride und energieeffiziente Antriebe für mobile Arbeitsmaschinen. 25. Februar 2015, Karlsruhe. 2015
ISBN 978-3-7315-0323-1
- Band 31** Michael Eckert
Energieoptimale Fahrdynamikregelung mehrmotoriger Elektrofahrzeuge. 2015
ISBN 978-3-7315-0332-3
- Band 32** Martin Scherer
Beitrag zur Effizienzsteigerung mobiler Arbeitsmaschinen. Entwicklung einer elektrohydraulischen Bedarfsstromsteuerung mit aufgeprägtem Volumenstrom. 2015
ISBN 978-3-7315-0339-2
- Band 33** Rinaldo Arnold
Automatische Abstimmung der Sekundärseite eines dreiphasigen Systems zur berührungslosen induktiven Energieübertragung. 2015
ISBN 978-3-7315-0355-2
- Band 34** Johannes Gültlinger
Kraftübertragung und Fahrbahnverschleiß durch Spikereifen. 2015
ISBN 978-3-7315-0358-3

- Band 35** Thorsten Dreher
Energieeffizienz von Konstantdrucksystemen mit sekundäreregelten Antrieben beim Einsatz in mobilen Arbeitsmaschinen. 2015
ISBN 978-3-7315-0377-4
- Band 36** Steffen Kölling
Konzeptionelle Untersuchung zur Neigekompensation von Stromabnehmern. 2015
ISBN 978-3-7315-0387-3
- Band 37** Michael Fritz
Entwicklungswerkzeuge für die Fahrzeugklimatisierung von Nutzfahrzeugen. 2015
ISBN 978-3-7315-0384-2
- Band 38** Ralf Oberfell
Stochastische Simulation von Energieflüssen im Nutzfahrzeug. Ein einsatzorientiertes Bewertungs- und Optimierungsverfahren. 2015
ISBN 978-3-7315-0403-0
- Band 39** Christoph Sturm
Bewertung der Energieeffizienz von Antriebssystemen mobiler Arbeitsmaschinen am Beispiel Bagger. 2015
ISBN 978-3-7315-0404-7
- Band 40** Florian Netter
Komplexitätsadaption integrierter Gesamtfahrzeugsimulationen. 2016
ISBN 978-3-7315-0414-6
- Band 41** Markus Springmann
Auslegung eines asynchronen Langstatorlinearmotors mit großem Luftspalt als Straßenbahnantrieb. 2015
ISBN 978-3-7315-0418-4
- Band 42** Alexander Basler
Eine modulare Funktionsarchitektur zur Umsetzung einer gesamtheitlichen Betriebsstrategie für Elektrofahrzeuge. 2015
ISBN 978-3-7315-0421-4
- Band 43** Hans-Georg Wahl
Optimale Regelung eines prädiktiven Energiemanagements von Hybridfahrzeugen. 2015
ISBN 978-3-7315-0422-1

- Band 44** Jennifer Heck
Zur Simulation des Rad-Schiene-Verschleißes bei Straßenbahnen. 2016
ISBN 978-3-7315-0443-6
- Band 45** Moritz Vaillant
Design Space Exploration zur multikriteriellen Optimierung elektrischer Sportwagenantriebsstränge: Variation von Topologie und Komponenteneigenschaften zur Steigerung von Fahrleistungen und Tank-to-Wheel Wirkungsgrad. 2016
ISBN 978-3-7315-0452-8
- Band 46** Philip Nagel
Entwicklung einer Betriebsstrategie zur Energierückgewinnung in hybriden Mehrverbrauchersystemen. 2016
ISBN 978-3-7315-0479-5
- Band 47** Matthias Pfriem
Analyse der Realnutzung von Elektrofahrzeugen in kommerziellen Flotten zur Definition einer bedarfsgerechten Fahrzeugauslegung. 2016
ISBN 978-3-7315-0489-4
- Band 48** Mohanad El-Haji
Ontologie-basierte Definition von Anforderungen an Validierungswerkzeuge in der Fahrzeugtechnik. 2016
ISBN 978-3-7315-0496-2
- Band 49** **9. Kolloquium Mobilhydraulik 22./23. September 2016 in Karlsruhe.** 2016
ISBN 978-3-7315-0573-0
- Band 50** 6. Fachtagung
Hybride und energieeffiziente Antriebe für mobile Arbeitsmaschinen. 15. Februar 2017, Karlsruhe. 2017
ISBN 978-3-7315-0601-0
- Band 51** Fabian Schirmaier
Experimentelle Untersuchung und Simulation des Umformverhaltens nähgewirkter unidirektionaler Kohlenstofffasergelege. 2017
ISBN 978-3-7315-0620-1
- Band 52** Mathias Cabrera Cano
Neuronale Netze mit externen Laguerre-Filtern zur automatischen numerischen Vereinfachung von Getriebemodellen. 2017
ISBN 978-3-7315-0621-8

- Band 53** Arwed Schmidt
Flottenbetrieb von elektrischen und autonomen Serviceagenten im städtischen Personennahverkehr. 2017
ISBN 978-3-7315-0633-1
- Band 54** Katharina Knaisch
Untersuchung von Spulensystemen zur induktiven Energieübertragung von Elektrofahrzeugen. Vergleich von Topologien und Entwicklung einer Auslegungsmethodik. 2017
ISBN 978-3-7315-0630-0
- Band 55** Frank Christof Stalter
Ansätze zur akustischen Optimierung von Reifen und Fahrbahnen für Elektrofahrzeuge unter Antriebsmoment. 2017
ISBN 978-3-7315-0645-4
- Band 56** Steffen Rose
Modellbildung und Simulation von mobilen Arbeitsmaschinen. Untersuchungen zu systematischen Modellvereinfachungen in der Simulation von Antriebssystemen am Beispiel Bagger. 2017
ISBN 978-3-7315-0684-3
- Band 57** Ulrico Peckelsen
Objective Tyre Development. Definition and Analysis of Tyre Characteristics and Quantification of their Conflicts. 2017
ISBN 978-3-7315-0713-0
- Band 58** Stefan Haag
Sequentieller Versuch zur HiL-unterstützten Validierung hybrider Antriebssysteme mit gekoppelten Antriebseinheiten. 2018
ISBN 978-3-7315-0752-9
- Band 59** Dirk Hülsebusch
Fahrerassistenzsysteme zur energieeffizienten Längsregelung - Analyse und Optimierung der Fahrsicherheit. 2018
ISBN 978-3-7315-0755-0
- Band 60** Christian Pohlandt
Intelligentes Gesamtmaschinenmanagement für elektrische Antriebssysteme. 2018
ISBN 978-3-7315-0774-1
- Band 61** Oliver Maier
Modellbasierte Entwicklung eines aktiven Sicherheitssystems für elektrifizierte Fahrräder. 2018
ISBN 978-3-7315-0778-9

- Band 62** Stephan Rhode
Robust and Regularized Algorithms for Vehicle Tractive Force Prediction and Mass Estimation. 2018
ISBN 978-3-7315-0807-6
- Band 63** Péter Megyesi
Methode zur Einbindung realer Nutzerprofile in die ökologische und ökonomische Bewertung von Fahrzeugkonzepten. 2018
ISBN 978-3-7315-0808-3
- Band 64** Benedikt Reick
Methode zur Analyse und Bewertung von stufenlosen Traktorgetrieben mit mehreren Schnittstellen. 2018
ISBN 978-3-7315-0815-1
- Band 65** Matthias Graf
Entwicklung und Validierung einer neuen Methode zur Charakterisierung des Scherverhaltens von Carbonfasergewebe mit Binderauftrag unter Normalkraft und viskoser Reibung bei hohen Prozesstemperaturen. 2018
ISBN 978-3-7315-0838-0
- Band 66** Christoph Kühn
Simulation von Fahrspielen und Energieflüssen in Nahverkehrssystemen. 2018
ISBN 978-3-7315-0740-6
- Band 67** 7. Fachtagung
Hybride und energieeffiziente Antriebe für mobile Arbeitsmaschinen. 20. Februar 2019, Karlsruhe. 2019
ISBN 978-3-7315-0873-1
- Band 68** Oliver Krauss
Experimentelle Untersuchungen zum Innengeräusch von Fahrzeugluftreifen. 2019
ISBN 978-3-7315-0867-0
- Band 69** Tristan Reich
Beurteilung der Prüfprozesseignung bei Fahrzeugversuchen mit mobilen Arbeitsmaschinen. 2019
ISBN 978-3-7315-0848-9
- Band 70** Matthias Bürckert
Realitätsnahe Bewertung des Einflusses der Oberflächenspannung flüssiger Zwischenmedien auf den maximalen Reibschluss zwischen Reifen und Fahrbahn. 2019
ISBN 978-3-7315-0891-5

- Band 71** Matthias Greiner
Verfahren zur Prädiktion des Rollwiderstands bei variablen Betriebsparametern auf Basis standardisierter Rollwiderstandsmessungen. 2019
ISBN 978-3-7315-0898-4
- Band 72** David Hummelberger
Hybride Werkstoffsysteme: Systematische Betrachtung und Bewertung der physikalischen Wirkmechanismen. 2019
ISBN 978-3-7315-0901-1
- Band 73** Michael Kerber
Analyse dynamischer Reifeneigenschaften und deren Auswirkung auf den Schwingungskomfort. 2019
ISBN 978-3-7315-0944-8
- Band 74** Kilian Berthold
Techno-ökonomische Auslegungsmethodik für die Elektrifizierung urbaner Busnetze. 2019
ISBN 978-3-7315-0953-0
- Band 75** Bernd Wassertheurer
Reifenmodellierung für die Fahrdynamiksimulation auf Schnee, Eis und nasser Fahrbahn. 2019
ISBN 978-3-7315-0957-8
- Band 76** Kai-Lukas Bauer
Echtzeit-Strategieplanung für vorausschauendes automatisiertes Fahren. 2020
ISBN 978-3-7315-0949-3
- Band 77** Thomas Schirle
Systementwurf eines elektromechanischen Fahrwerks für Megacitymobilität. 2020
ISBN 978-3-7315-0995-0
- Band 78** Dominik Dörr
Simulation of the thermoforming process of UD fiber-reinforced thermoplastic tape laminates. 2021
ISBN 978-3-7315-0998-1
- Band 79** Dominik Robert Naake
Simulation of damage mechanisms in weave reinforced materials based on multiscale modeling. 2020
ISBN 978-3-7315-1005-5

Band 80

Martin Hohberg

**Experimental investigation and process simulation of the
compression molding process of Sheet Molding Compound
(SMC) with local reinforcements. 2021**

ISBN 978-3-7315-1007-9

Hybridization of Sheet Molding Compound (SMC) with local reinforcements leads to new cost-efficient lightweight solutions. Nevertheless this increases the process and design complexity, so that enhanced simulation methods in the context of the virtual process chain becomes more important.

For this reason, a new three-dimensional approach for the process simulation of SMC is developed in this work. This approach takes into account both, the core layer as well as the thin lubrication layer. By implementing it into Coupled-Eulerian-Lagrangian (CEL), hybrid process simulations can be performed. In order to transfer the information from the process simulation to the structure simulation, a CAE chain is further developed. This CAE chain enables the transfer of the information from the process to the structure mesh.

To analyze the flow behavior experimentally and to provide the required valid material parameters for process simulation, a new rheological tool is developed. With this rheological tool, the compressible behavior of semi-structural SMC formulations is proven for the first time and described by using a phenomenological approach.

